

Material and Device Investigations On A Carbon Nanotube-Based Torsional Nanoelectromechanical System

Adam Roger Hall

A dissertation submitted to the faculty of the University of North Carolina at Chapel Hill
in partial fulfillment of the requirements for the degree of Doctor of Philosophy in the
Curriculum of Applied and Materials Sciences

Chapel Hill
2007

Approved By:

Dr. Sean Washburn

Dr. Richard Superfine

Dr. Jianping Lu

Dr. Yue Wu

Dr. Jie Liu

© 2007
Adam Roger Hall
ALL RIGHTS RESERVED

ABSTRACT

Adam Hall: Material and Device Investigations On A Carbon Nanotube-Based Torsional
Nanoelectromechanical System

(Under the direction of Dr. Sean Washburn)

The experiments in this thesis present a foundational study of a nanoelectromechanical system that demonstrates high potential for use in a wide range of applications. This system incorporates an individual carbon nanotube as a torsional spring for a lithographically defined, nanometer-scale metal mass suspended above a substrate.

Fabrication and operation of such a device is discussed. Investigations are then performed to elucidate a variety of material and device characteristics. First, the shear (twisting) modulus of an individual singlewall carbon nanotube is measured. This is done through a combination of direct electrostatic actuation and computer modeling. Next, the theoretical dependence of singlewall carbon nanotube transport properties on torsional strain is confirmed experimentally. Finally, the device is used as a self-sensing resonant oscillator. The characteristics of such a device and the implications of all results are discussed, as are future directions.

ACKNOWLEDGEMENTS

As with all work, the contents of this thesis do not represent the effort of the author alone. I am indebted to a great many people for their contributions, both direct and indirect.

First, I express my appreciation to my principal advisor, Sean Washburn. Thank you for allowing me the freedom to explore and to learn from my own mistakes- for better or worse. Your method of mentorship was one that I hadn't been exposed to previously: sink or swim. I hope I swam.

Next, I owe a debt of gratitude to many colleagues. Chief among them are Richard Superfine and Michael Falvo, the two additional principal investigators who oversaw this work. The atmosphere in our research group has been consistently fun and stimulating during the entire time I have been a part of it, and this fact is in no small part due to the leadership of these two gentlemen. I hope that current and future group members appreciate that this is not the case everywhere. Thanks also to Lei An for taking the time to show me how to perform chemical vapor deposition and to Leandra Vicci for the assistance on all manner of things (especially for her help on the analysis of the data presented in Ch. 3). I also wish to sincerely thank the many fellow students and postdoctoral fellows with whom I have been fortunate to work, specifically Sreeja Asokan, Louise Jawerth, Lloyd Carroll, Michael Stadermann, Lamar Maire, Adam Shields, Ben Evans, Jerome Carpenter and Kwan Skinner. Without you all, either my

appreciation for science or my sanity would be severely diminished (and probably both). I would especially like to thank Garrett Matthews and Tim Meehan for every discussion, science and otherwise. I'm not entirely sure I would have made it without them.

I owe special recognition to Phillip Williams and Stergios Papadakis, who worked on nanotube torsional devices previous to me and directly with me, respectively. Their stellar work has been the rock upon which this thesis was built. Even after each had officially left the research group, they offered support and advice. For this, I am especially thankful.

The friends who stuck with me through this endeavor are true friends indeed. To Kendra Stockman, thanks for putting things into perspective. To Melanie Fehrenbacher and Caroline Oldham, thank you for being two of the best people I know.

To the Parkers, who treated me like a son (and brother) before I actually was, I am eternally grateful. I might still be stranded at a gas station on Jones Sausage Road if not for you.

To Mom, Dad and Nicole, I owe you everything. Your unerring support and confidence was more than I deserved sometimes. I wish I could have explored the world while staying closer to where my heart is, but thank you for putting up with the distance. I love you all.

Finally, to my wife Amanda, I can't express how thankful I am to have you always stand by me. You are my light in the darkness. No matter what else happens, if I've got you, everything is going to be fine, fine, fine.

TABLE OF CONTENTS

List of Tables.....	ix
List of Figures.....	x
List of Abbreviations.....	xiii
1. Introduction	
1.1 Motivation.....	1
1.2 An Introduction to Carbon Nanotubes.....	3
1.3 Carbon Nanotube Mechanical Properties.....	6
1.4 Electrical Transport in Carbon Nanotubes.....	7
1.5 Concerns in Real Nanotube Devices.....	10
1.6 Thesis Overview and Outline.....	16
2. Experimental techniques	
2.1 Introduction.....	18
2.2 Carbon Nanotube Deposition.....	18
2.3 The Carbon Nanotube Torsional Device	21
2.4 Electrically Contacting Carbon Nanotubes.....	26

3. Experimental Measurement of Single-wall Carbon Nanotube Shear Moduli	
3.1 Introduction.....	29
3.2 Experimental Methods.....	36
3.3 Device Modeling and Analysis.....	38
3.4 Results and Discussion.....	41
4. Electromechanical Response of Single-wall Carbon Nanotubes to Applied Torsional Strain	
4.1 Introduction.....	45
4.2 Experimental Methods.....	50
4.3 Results and Discussion.....	57
5. Single-wall Carbon Nanotube Torsional Oscillators in Resonance	
5.1 Introduction.....	63
5.2 Resonator Detection Schemes.....	68
5.3 Experimental Methods.....	75
5.4 Oscillator Behavior of a SWNT Torsional Device.....	81
5.5 Results and Discussion.....	86
6. Summary and Future Directions	
6.1 Research Summary and Implications.....	88
6.2 Future Directions and Aims.....	89

Appendices

A1. Chemical Vapor Deposition Instructions.....	91
A2. Torsional Device Fabrication Details.....	92
Citations List.....	115

LIST OF TABLES

Table 3.1 Collected data on MWNT torsional oscillators.....	34
Table 5.1 Calculated dissipation mechanisms for SWNT torsional oscillators.....	86

LIST OF FIGURES

Fig. 1.1 Early transistor technology.....	2
Fig. 1.2 Nanotube chirality mapped to the graphitic Bravais lattice.....	4
Fig. 1.3 SWNT representations in k -space.....	8
Fig. 1.4 Relation of SWNT Fermi point location to band gap.....	9
Fig. 1.5 Schottky barrier formation in SWNT contacts.....	12
Fig. 1.6 SWNT field effect in schematic and data.....	13
Fig. 1.7 Device modeling for the effect of gate oxide and separation on field effect.....	15
Fig. 2.1 Diameter distribution for CVD-grown SWNT.....	21
Fig. 2.2 Schematic of CNT torsional device.....	22
Fig. 2.3 Photolithography pattern for macroscopic contacts.....	23
Fig. 2.4 Device fabrication process using CVD SWNT.....	24
Fig. 2.5 Fully suspended devices.....	26
Fig. 2.6 Bilayer PMMA method.....	27
Fig. 3.1 MWNT mechanical characterization techniques.....	30
Fig. 3.2 MWNT torsional response.....	32
Fig. 3.3 Interferometric measurements on MWNT torsional devices.....	33
Fig. 3.4 Measurable geometric values from a device image.....	36
Fig. 3.5 Characterization of torsional deflection angle from images.....	37
Fig. 3.6 Finite-element modeling of a SWNT device.....	39
Fig. 3.7 Calculating the torque on a modeled paddle.....	40
Fig. 3.8 Experimental torsional properties of individual SWNT devices.....	42
Fig. 3.9 Calculated buckling of a SWNT.....	43

Fig. 4.1	Theoretical dependence of SWNT band gap on applied strains.....	47
Fig. 4.2	Electromechanical response of SWNT transport to axial stretching.....	49
Fig. 4.3	Torsion-induced oscillations in MWNT transport.....	50
Fig. 4.4	Increasing maximum deflection angle by device geometry.....	52
Fig. 4.5	Transport vs. torsional strain experimental setup.....	53
Fig. 4.6	Deflection measurement of a thick paddle.....	54
Fig. 4.7	Gate dependence of transport before and after etching for two SWNT devices..	55
Fig. 4.8	Typical measured variation in SWNT gate response.....	56
Fig. 4.9	Source-drain resistance vs. applied torsional strain for six SWNT devices.....	58
Fig. 4.10	I-V linearity vs. resistance-strain dependence for measured SWNT devices...	59
Fig. 4.11	Source-drain resistance vs. applied torsional strain with calculated fit.....	60
Fig. 4.12	Effect of etching on SWNT device I-V character.....	61
Fig. 5.1	Calculated amplitude and phase curves at resonance.....	65
Fig. 5.2	Dependence of Q on gas pressure.....	67
Fig. 5.3	Schematic of MEMS capacitive displacement sensing.....	71
Fig. 5.4	NEMS resonator measurement with EMF.....	71
Fig. 5.5	MWNT resonance measurement via field emission.....	72
Fig. 5.6	Circuit diagram for piezoresistive oscillator down-mixing technique.....	73
Fig. 5.7	Tunable SWNT bridge oscillator behavior.....	74
Fig. 5.8	Effect of DC offset on electrostatically driven oscillator behavior.....	76
Fig. 5.9	Measured resonance and first harmonic for a SWNT torsional device.....	77
Fig. 5.10	Agreement between SWNT quasistatics and observed resonance peaks.....	78
Fig. 5.11	SWNT device resonance measurement through direct SEM imaging.....	79

Fig. 5.12 Resonance observed with transport measurement and with direct imaging.....	80
Fig. 5.13 Drive amplitude-dependence of SWNT torsional device resonance peaks.....	82
Fig. 5.14 Square of the drive amplitude vs. peak height for a SWNT oscillator.....	83
Fig. 5.15 Theoretical oscillations in SWNT band gap for high applied strains.....	84
Fig. 5.16 Relation of SWNT torsional device Q to that of other oscillators.....	85

LIST OF ABBREVIATIONS

<i>AFM</i>	atomic force microscope
<i>CNT</i>	carbon nanotube
<i>CVD</i>	chemical vapor deposition
<i>EBL</i>	electron beam lithography
<i>EMF</i>	electromotive force
<i>FE</i>	finite element
<i>FET</i>	field-effect transistor
<i>MEMS</i>	microelectromechanical systems
<i>MWNT</i>	multi-wall nanotube
<i>NEMS</i>	nanoelectromechanical systems
<i>PMMA</i>	polymethyl methacrylate
<i>SEM</i>	scanning electron microscope
<i>SWNT</i>	single-wall nanotube
<i>TEM</i>	transmission electron microscope

*It's a magical world, Hobbes, ol' buddy...
Let's go exploring!*

-Calvin
from *Calvin & Hobbes*

Introduction

*I don't know how to [miniaturize a computer] in a practical way, but I do know that computing machines are very large... Why can't we make them very small, make them of little wires, little elements---and by little, I mean **little**. For instance, the wires should be 10 or 100 atoms in diameter, and the circuits should be a few thousand angstroms across.*

-Richard P. Feynman, 1959

1.1 Motivation

In 1959, Dr. Richard Feynman of the California Institute of Technology recognized that technology didn't have to take up the space that it did. At the time, though, just getting a computer to work was a feat unto itself. The first field effect transistor (or at least the first FET-like device) had been developed by J. E. Lilianfeld in as early as 1925 (Fig. 1.1a), but 34 years later, silicon technology had only begun to allow realization of a working device. Integration into systems was still years away. Electrical computing technology still depended on the vacuum tube, which made it bulky (Fig. 1.1b). The "compact" technology of the day was the black and white home television. Clearly, science had a number of things to work on before worrying about getting smaller, especially to the degree that Dr. Feynman was suggesting.

But, it wouldn't be long before the idea was no longer relegated to the realm of science fiction. The advent of integrated circuit (IC) technology in the 1960's, which combined the burgeoning field of silicon processing with much improved transistor

performance to great success, made it possible to realize large numbers of electrical circuit devices over a small area. The question was no longer whether miniaturization was possible, but in what ways the technology would benefit from it. Aside from merely taking up less space, what would there be to gain from targeting length scales like those postulated by Feynman?

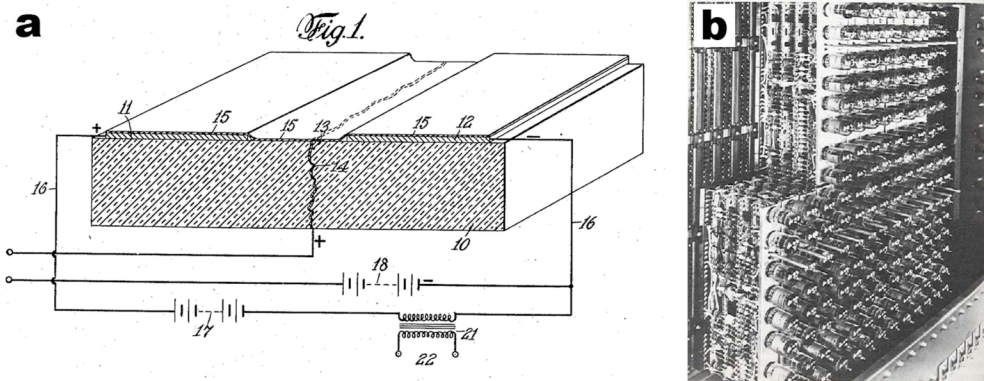


Figure 1.1 (a) Figure 1 from J. E Lilianfeld’s first patented FET-like device (US Patent #1745175). (b) An example of a vacuum tube computing system (image from www.columbia.edu/acis/history)

The answer quickly made itself apparent in computational technology. Hundreds of memory-storing devices on one small chip was impressive for the first IC, but storing larger amounts of information would require larger numbers of devices, and each one requires a certain amount of power to operate. Although the power consumption for a single device may be small, the total amount added up quickly when multiplied over extremely large numbers, resulting in unreasonably high power requirements per chip. Further, the low efficiency of transistor devices resulted in a high heat loss, making rising temperatures another factor. In high ambient temperature ranges, the devices cease to function properly. Each of these hurdles could be positively affected by miniaturizing the

technology; smaller individual devices would require lower power to run and have less surface area from which to generate heat.

But, the benefits of technology miniaturization in general would be greater and more wide-ranging than such mere practicality. For example, device physics acts very similarly and predictably over a large range of macroscopic length scales, but at scales approaching the molecular level, quantum effects begin to be less masked by bulk properties. This reveals a whole array of new material characteristics to exploit in new devices. In biologically relevant technology, decreased size can result in much higher sensitivity, meaning that the technology can interact with entities involved in basic biological functions or with entities that are detrimental to those functions.

This is the length scale that is being explored by the present state of the art nanotechnology and is the subject of the current thesis, which will investigate one specific nanometer-scale device. It is built on a single carbon nanotube; “a wire... 10 or 100 atoms in diameter”. This brings us closer than ever to realizing the fantastic idea postulated by Dr. Feynman nearly half a century ago.

1.2 An Introduction to Carbon Nanotubes

Since their 1991 discovery[1], carbon nanotubes (CNT) have been the darling of nanotechnology. Their use has been suggested in everything from electrical circuitry to the “space elevator”- an Earth-bound tether for a geosynchronous satellite. While their infinite utility may be somewhat overblown, the motive for such widespread interest is sound. This is indeed a unique material.

Essentially, CNT are a single, atomically thin graphitic layer rolled up on itself such that the hexagonal lattice structure is maintained circumferentially. Being only one atomic layer, this formation is energetically favorable only for small tube diameters, on the order of a single nanometer, but the length in the axial dimension is limitless, making the material molecular scale in one dimension and potentially macroscopic in another. Furthermore, an ideal CNT with few defect sites will be both mechanically strong and chemically inert.

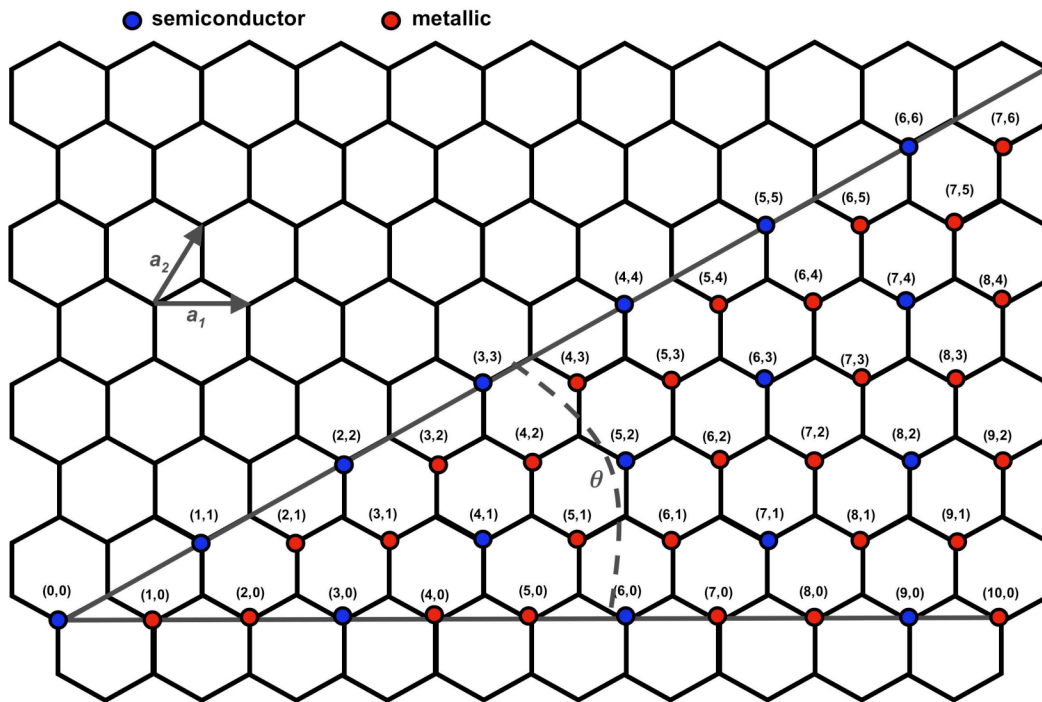


Figure 1.2 The carbon nanotube chiral structure, as related to the crystal lattice of graphite. Any nanotube can be mapped to a lattice point rolled over to meet $(0,0)$. Also noted are the metallic or semiconducting behavior of a given lattice point (discussed in section 1.4)

CNT are often characterized by their chiral vector, C , which is defined by the sum of an integer number of lattice vectors a_1 and a_2 on the Bravais lattice (Fig. 1.2):

$$C = m \cdot a_1 + n \cdot a_2 \quad (\text{Eq. 1.1})$$

In effect, this relation means that the point (m,n) can be rolled to meet the origin $(0,0)$ and form the cylinder of the CNT. More commonly used than C to define a nanotube is the wrapping angle θ , or the angle at which C wraps about the tube axis (compared to the uniaxial vector). The relation between θ and the lattice point (m,n) is

$$\theta = \tan^{-1} \left[\frac{\sqrt{3}m}{m+2n} \right] \quad (\text{Eq. 1.2})$$

It is notable that all CNT can be mapped to a chiral angle in this range of 0° - 30° due to symmetry in the lattice structure. In other words, a $(4,3)$ nanotube is just a $(3,4)$ nanotube turned on its head.

As a consequence of mapping to the hexagonal graphitic lattice, the lattice point (m,n) is also correlated with the diameter d_t of the nanotube. This relation is given by

$$d_t = \frac{\sqrt{3}a_{c-c} (m^2 + n^2 + mn)^{1/2}}{\pi} \quad (\text{Eq. 1.3})$$

where a_{c-c} is the carbon-carbon bond length (1.42 \AA). Hence, CNT come in a variety of clearly defined types, each interrelated yet possessing distinct geometrical values.

CNT can also exist as either an individual tubule or as a series of concentric tubules, each having its own distinct properties. Tubes made of only one layer are thus referred to as single-wall nanotubes (SWNT) and those made of any number of coaxial layers are collectively referred to as multi-wall nanotubes (MWNT). Practically, MWNT are somewhat easier to incorporate into experiments, due to their larger diameter (on the order of tens of nm). However, as will be shown in coming sections, they also exhibit decidedly less interesting properties when compared to their single layer counterparts.

1.3 Carbon Nanotube Mechanical Properties

Carbon atoms in a CNT share sp^2 bonds, like those found in planar graphite and fullerenes. As each atom is covalently bonded to three nearest neighbors, the resulting structure is incredibly robust. Theoretical work[2] expected that a SWNT would have a Young's modulus of ~ 1 TPa and a shear modulus of ~ 0.5 TPa. MWNT values would vary depending on the number of shells that comprise it, but values were expected to reach a Young's modulus above 1.1 TPa and a shear modulus of more than 0.55 TPa. Experimental measurements on diamond[3] (along the cube axis) has yielded values of 1.06 and 0.58 TPa, respectively.

A variety of experimental work[4-9] has been done to confirm these values. Results for the Young's modulus range from 0.4 to 4 TPa, in rough agreement with theory (owing for possible defect sites, mechanical losses and measurement error). These experimental results will be discussed in greater detail in Ch. 3. Furthermore, manipulations of individual CNT[10] have demonstrated that they exhibit little to no signs of wear or fatigue despite repeated application of large amounts of strain. This robust behavior makes the material ideal for a host of applications including scanning probe tips[11], composites[12, 13] and nanomechanical systems.

Scanning probe force measurement techniques have also been used to directly measure the shear modulus of MWNT[14] using a fabricated metal pad as a lever arm[15]. The values garnered here were around 0.4 TPa, in agreement with theoretical expectations[2]. Previous experimental work has been unable to measure shear modulus in SWNT. This is the subject of work presented later in this thesis (Chapter 4).

1.4 Electrical Transport in Carbon Nanotubes

As discussed previously, lattice continuity in the CNT tubule formation can be achieved with the carbon atoms spiraling about the axis at any number of angles with respect to the diameter. While these different varieties possess slightly different dimensions, the greatest distinction amongst them is found in their transport properties.

Amazingly, SWNT of slightly different chirality can have radically different band structure- ranging from conductivity as high as copper to as wide a band gap as bulk silicon[16]. This has made the material especially attractive to nanotechnology as electrical or electromechanical components and much experimental work has been performed to this end, notably toward utility as field-effect transistors[17].

For obvious reasons, CNT band structure is related closely with that of an individual sheet of planar graphite, known as graphene. Graphene is known as a semi-metal, not being uniquely classifiable as an insulator, semiconductor or pure metal due to the two-dimensional confinement of carrier mobility in the graphitic plane combined with the specific rotational symmetry of the lattice structure. The k -space representation of the lattice is a hexagon containing two lattice points (Fig. 1.3a) and the energy structure of the conduction (π) and valence (π^*) bands with respect to this k -space representation result in points of energy minima and maxima, respectively (Fig. 1.3b). These points (called K points) occur at the six vertices of the hexagonal k -space lattice representation and meet between bands at the Fermi energy, E_F . Importantly, the energies recede from E_F in a conical shape (known as a dispersion relation, $E(k)$) and electronic states that approaching the Fermi level follow this shape.

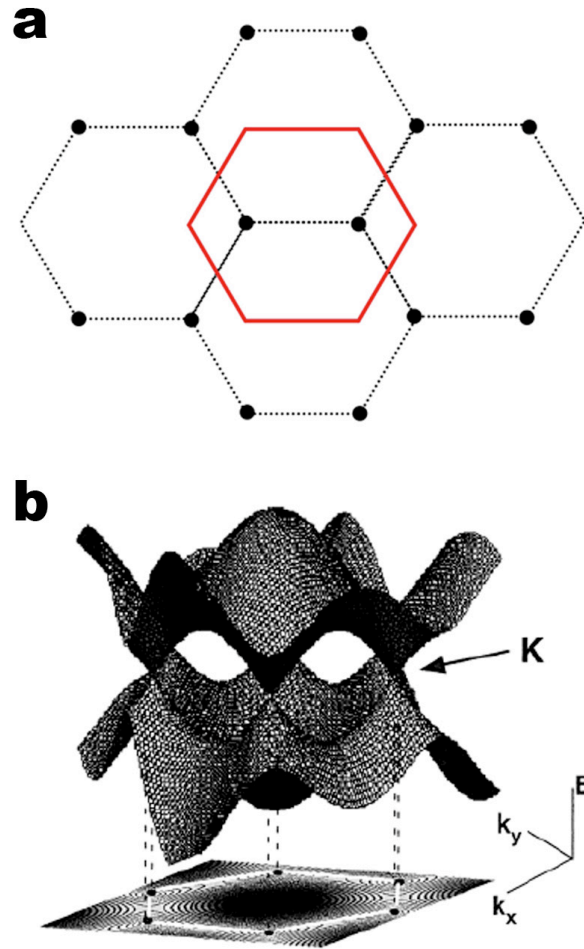


Figure 1.3 (a) The k -space representation of the graphene lattice (red outline) atop the Bravais lattice. (b) The shapes of the graphene π and π^* energy bands in k -space. Also shown is the energy projection onto a 2D plane and the K points. (b) from [18].

The cylindrical shape of the CNT imposes an additional circumferential boundary condition on the electron wave function and further limits the allowed propagation of carriers traveling down the tube axis. This gives rise to one-dimensional conduction bands that can be applied to the energetic profile of planar graphene to reveal the electronic structure of the tube itself.

Figure 1.4 shows the k -space representation of the graphite lattice with respect to these 1D conduction bands. When these bands intercept the k points (located at the six

vertices of the hexagon), free carriers are available for axial transport. Part a shows a metallic SWNT, where all Fermi points are intersected (red dots). Part b shows a lattice in which the conduction bands miss all Fermi points, resulting in a semiconducting tube. Below each representation is the shape of the energy band when overlaid on the conical dispersion relationship mentioned previously. When the conduction band approaches the Fermi point but does not meet it, the separation is representative of the band gap. Note the conical band shape.

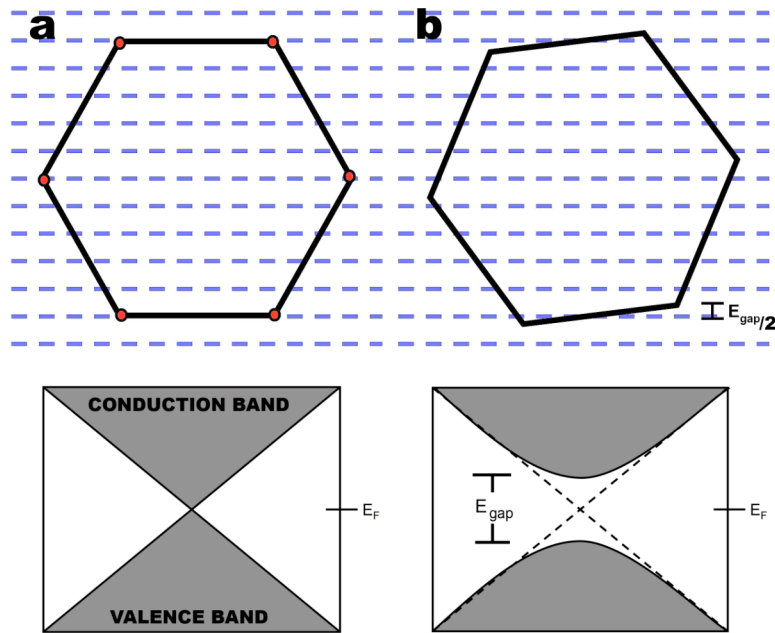


Figure 1.4 One-dimensional conduction bands with an overlaid k -space representation of (a) a metallic, or "armchair", nanotube and (b) a chiral nanotube. Red points represent Fermi points intersecting with conduction bands. Below each is the valence-conduction band character as the allowed bands are projected on the k -space energies.

In general, SWNT exhibit metallic behavior when

$$2m + n = 3x \quad (\text{Eq. 1.4})$$

where x is an integer. All other tubes will have some band gap, roughly of magnitude $(0.7/d_t)$ eV, where d_t is the CNT diameter in nm[16]. It is notable that due to the four degenerate states in a SWNT (two spin states and two for directionality, or “handedness”), the maximum conductance of an individual metallic nanotube is expected to be $4 e^2/h$, or a resistance of ~ 6.5 k Ω . While this level of conductance has not yet been observed, measurements continue to approach it.

MWNT exhibit the character of a small- or zero gap semiconductor regardless of the chirality of the outer layer. This is in part due to the inverse proportionality of the band gap to the tube diameter, $E_{gap}=(t_o a_{c-c})/d$, where t_o is the tight binding overlap integral (2.7 eV), a_{c-c} is the nearest carbon atom distance and d is the diameter[16]. At diameters of ~ 15 nm, the energy required to exceed the band gap is comparable to thermal energy at room temperature. It is also poorly understood how much neighboring shells interact with each other. Such interaction could make a larger number of states available to carriers, thus making a MWNT into a higher-order conductor than the 1D SWNT system, or the interaction could create a pseudogap in the density of states[19].

1.5 Concerns in Real Nanotube Devices

Possibly the primary concern when making electrical contact to nanotubes has been the formation of Schottky barriers. When a metal makes contact with a semiconductor, the Fermi energy levels must equilibrate through charge transfer. Because of the reduced mobility in the semiconductor, this causes a build up of charge at the interface, resulting in local bending of the electron energy bands and a potential barrier for carriers to overcome before transport can occur across the junction.

For n -type semiconductors, there is a buildup of positive charges at the junction (or, alternatively, an absence of negative carriers, hence the terminology depletion zone) as its higher Fermi level decreases to meet that of the metal (Fig. 1.5a). In this case, the height of the barrier ϕ_B is the difference between work function of the metal, ϕ_m , and the electron affinity of the semiconductor, χ [20]:

$$q\phi_{Bn} = q(\phi_m - \chi) \quad (\text{Eq. 1.5})$$

where q is charge. The value ϕ_m is the energy difference between vacuum and the metal Fermi level while χ is the difference between vacuum and the bottom of the conduction band in the semiconductor. The resulting arrangement is rectifying to n carriers traveling from the semiconductor to the metal.

For p -type semiconductors, the Fermi level must be raised to meet that of the metal (Fig. 1.5b), causing a buildup of negative charge at the junction (a p -type depletion zone). Here, the effect is reversed, rectifying p carriers from the semiconductor to the metal with a barrier of[20]

$$q\phi_{Bn} = E_g - q(\phi_m - \chi) \quad (\text{Eq. 1.6})$$

where E_g is the energy across the band gap. The effect appears the same in both cases, due to the difference of carriers.

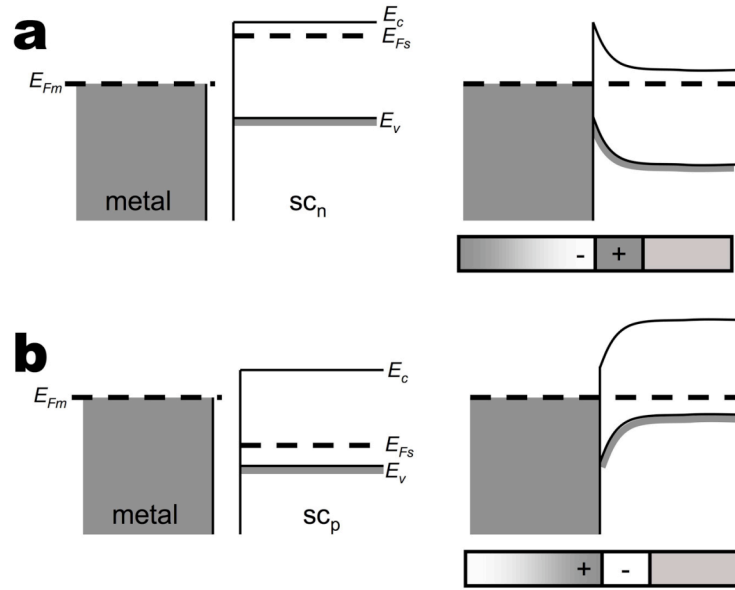


Figure 1.5 Schottky barrier formation for (a) a *n*-type and (b) a *p*-type semiconductor. In each is a representation of the energy structure before (left) and after (right) being brought into contact and in the lower right is a representation of the regions of charge buildup.

In CNT devices, Schottky barriers are difficult to avoid. Even with metallic tubes, the existence of small amounts of contamination between the contacting metal and the tube can cause similar energy barriers because charge transfer is not unimpeded. Here, the barrier potential is the difference between the two work functions. Experimentally, the most success at attaining ohmic contacts has been through work function matching and thermal treatment. As shown in eqs. 1.5 and 1.6, the more closely matched the metal work function is to the electron affinity of semiconducting CNT (and indeed the work function of metallic CNT), the lower the energy barrier will be. Therefore, it has been demonstrated that Pd contacts yield the most ohmic behavior, followed by Au, Ti, etc[21, 22]. Furthermore, thermal treatments have been shown to aid the contact[23], mostly through decomposition of contamination layers between CNT and the adjoining metal.

Once a CNT device is fabricated, the bands can also be manipulated through external fields, such as with a gate electrode. Transistor behavior has been demonstrated using SWNT[17, 24] showing a large gate dependence, wherein the conduction band of the tube is essentially bent by an applied field until a barrier is created or removed for transverse carriers (Fig. 1.6). As MWNT tend to be metallic (see section 1.X), field effect observed in those devices tend not to be related to intrinsic properties of the tube itself. So, further discussions will deal specifically with SWNT devices only.

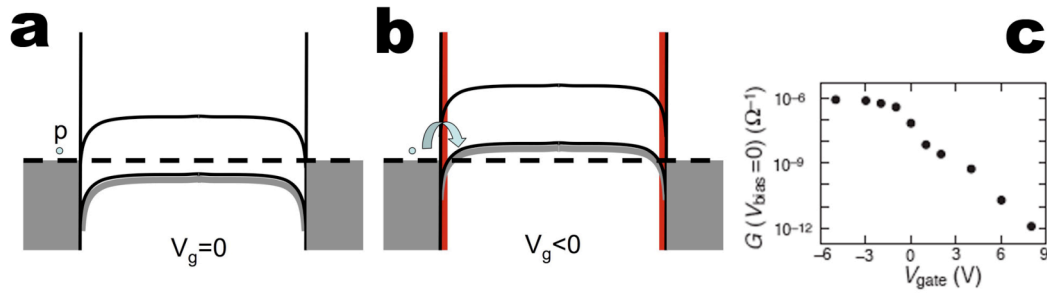


Figure 1.6 Ideal field effect on a p-type SWNT with Schottky barriers for (a) zero and (b) negative values of gate bias. Red areas in (b) indicate the small tunneling barrier that remains after band deflection. (c) Experimental data from a SWNT transistor[17].

The electric field effect (or transconductance) of a SWNT device is also strongly correlated to aspects of the device outside the material properties of the tube. Real devices are generally separated from the gate electrode by a dielectric layer (typically silicon oxide) of thickness z and permittivity ϵ . These values can be varied from one device to the next and doing so will be of importance later in this thesis (see Ch. 4). Therefore, it is useful to discuss how large the dependence of gate response on z and ϵ is. This examination begins by looking at the transport across the SWNT (source-drain), which follows Ohm's law:

$$V_{SD} = RI_{SD} = \left(\frac{L}{\sigma A} \right) I_{SD} \quad (\text{Eq. 1.7})$$

where σ is conductivity, A is cross sectional area and L is tube length. Conductivity can further be written as[20]

$$\sigma = Q\mu_n \quad (\text{Eq. 1.8})$$

where Q is the total charge on the tube ($Q=nq$, where n is number of carriers and q is elementary charge) and μ_n is electron mobility. Now, because Q is related to capacitance C via $Q=CV$, it is clear that C has a direct relation with the measured conductivity of the SWNT.

The capacitance C between the SWNT and the gate electrode is[25]

$$C = \frac{4\pi\epsilon_0 L}{2\ln(2z/r)} \quad (\text{Eq. 1.9})$$

where ϵ is the permittivity of the material between, L is the tube length, z is the separation distance between the tube and the gate and r is tube radius. Therefore, comparisons can be made between three separate cases: (1) thin oxide devices, (2) thick oxide devices and (3) suspended devices (Fig. 1.7). Thin oxide is generally used in the aforementioned SWNT FET studies[17, 24], where a large field effect is desirable. The first model approximates this. The thick oxide model looks at the results of changing z and the suspended model examines a change in ϵ .

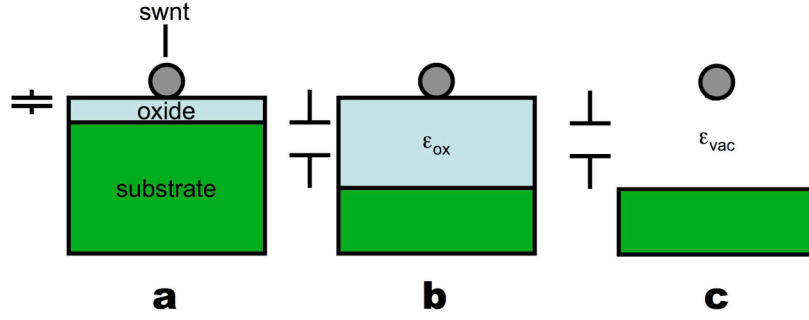


Figure 1.7 Three SWNT transistor models used to study the effect of device geometry on the field effect: (a) thin oxide, (b) thick oxide and (c) suspended.

The only factor changing between cases 1 and 2 (for the same device geometry) is the oxide thickness z . So the ratio of the capacitances (and therefore the conductivities) for the two cases is

$$\frac{C_2}{C_1} = \frac{\ln(2z_1/r)}{\ln(2z_2/r)} \quad (\text{Eq. 1.10})$$

As a test case, typical values are used for z_1 (100 nm), z_2 (1 μm) and r (1 nm), showing that a tenfold increase in distance z decreases the capacitance (i.e. measured conductivity) by only $\sim 30\%$.

In analyzing the effect of changing the permittivity ϵ (case 2 to case 3), the relation is simply

$$\frac{C_3}{C_2} = \frac{\epsilon_3}{\epsilon_2} \quad (\text{Eq. 1.11})$$

Assuming ϵ_3 is vacuum permittivity (ϵ_0) and ϵ_2 is silicon oxide permittivity ($3.8\epsilon_0$), removing the oxide decreases capacitance to nearly a quarter of its initial value. Therefore, the intervening material has a strong effect on the transconductance.

A final aspect of real devices that bears mention is the effect of surface charges on a contacted CNT device. Various ions can become deposited in the thermal oxide of a wafer as it is being formed[26]. These can cause a net positive charge in the material that can in turn induce a negative charge in the tube itself. Furthermore, at the boundary of the oxide and the bulk silicon, interface charges exist- a result of the Si^+ ions left after oxidation. These can also contribute to induced charge.

The first of these charge sources (ionic contamination) is nearly impossible to quantify without specific knowledge of the wafer fabrication. The second (interfacial charge), however, can be estimated to have a density of 10^{10} q/cm^2 for {100} silicon[26]. The expected potential V caused by these interfacial charges is[27]

$$V = \frac{z\rho}{2\epsilon} \quad (\text{Eq. 1.12})$$

where z is separation distance, ρ is surface charge density and ϵ is the permittivity of the intervening space. Therefore, an uncertainty is added to the gate bias that varies directly with the density of charges caused by the dangling bonds. This relationship will be referred to in later chapters.

1.6 Thesis Overview and Outline

In Chapter 2 of this thesis, experimental methods and CNT torsional device geometry are discussed. Chapter 3 discusses resonant actuation of a MWNT torsional device. Chapter 4 concentrates on measurements of SWNT material properties using a torsional device. In Chapter 5, the use of the same type of device to study transport phenomena in a SWNT under applied shear strain is demonstrated. Chapter 6 discusses

the operation of SWNT torsional devices as oscillators in resonance. Finally, Chapter 7 summarizes the thesis and discusses future directions and uses of the experiments.

Experimental Technique and Design

Though this be madness, yet there be method in 't.

-William Shakespeare, *Hamlet*,
Act 2, scene 2

2.1 Introduction

The experiments detailed in this thesis have required a number of specialized fabrication and measurement techniques. Some of the methods are performed in a common manner, such as photolithography. These will be reviewed only briefly. However, other methods have been modified so as to allow for the highest quality device as a final product. These are the details that will be the focus of this chapter

2.2 Carbon Nanotube Deposition

While the specifics of the CNT deposition techniques used are somewhat well established, they bare mentioning in order to disclose the specific methods chosen for the present devices.

For devices incorporating MWNT (not discussed in this thesis), raw material made with the laser ablation method[28] are used. Here, a target material composed largely of graphite and some catalyst particles (Co or Ni) is placed into a controlled furnace heat zone (900-1200 C) and a laser is used to evaporate the material. What results

is found to be up to 90% pure CNT. The material is then suspended in dichloromethane as nanotubes tend to suspend freely in nonpolar solvents such as this. In general, neither mass nor volume ratios are measured, but roughly 1 cm³ of raw material is added to ~30 mL of solvent. Suspension density dictates the final density of nanotubes on a substrate and is adjusted to achieve the desired surface coverage. The MWNT suspension is then subjected to an ultrasonic treatment for an hour to break up densely packed bundles and result in a homogeneous mixture.

For deposition onto a substrate, a drop of MWNT suspension is placed onto a substrate, followed by several drops of isopropanol. This addition changes the overall polarity of the solvent, causing the nanotubes to fall out of suspension and onto the underlying surface. After drying under nitrogen flow, the substrate is ready for further fabrication.

SWNT can be produced in the same manner as MWNT in a laser ablation system through choice of catalyst particle, especially by using particles of smaller average diameter[29]. They are, however, more difficult to deposit from liquid. This is because their mass-to-surface area ratio is much lower than that of a MWNT, predominantly resulting in the formation of ropes rather than individual nanotubes due to Van der Waals interactions. This is avoided through the use of a surfactant method[30], wherein raw SWNT material is added to a 1% wt. solution of Sodium Dodecylsulfate (SDS) in water and exposed to a vigorous ultrasonic treatment (60-80 W) for an hour. This has the effect of breaking apart many of the ropes of material, which are then prevented from re-agglomerating by the surfactant layer surrounding them. The suspension is then centrifuged for 60 minutes at 12,000 rpm, pulling most of the remaining ropes out of

suspension. The supernatant is then decanted and deposited onto a substrate spinning at 2000 rpm. The surfactant layer is removed from the deposited material by deluging the surface with water.

This liquid deposition technique does not deposit individual material with absolute certainty, however. In order to avoid these issues, this work preferentially uses SWNT grown directly on silicon substrates using a chemical vapor deposition (CVD) method. The central concern of CVD is the thermal decomposition of organic gas in a controlled environment and the catalysis of the decomposed material in order to produce SWNT. This requires catalyst particles (usually Fe- or Ni-containing) of very small diameter (<10 nm) or with asperities of a similar scale.

The growth method used is discussed in detail in Appendix 1. In general, Fe/Mo catalyst particles[31] with diameters ~ 1 nm (or other similar sized, Fe-containing particles) were deposited directly onto a substrate by evaporation of a liquid suspension. Ideal catalyst density was determined in order to result in low nanotube coverage for device fabrication. The substrates were calcinated at 700 C in air for 10 minutes and then placed in a hydrogen flow (400 sccm). The temperature was raised to 900 C and the substrates were exposed to methane (800 sccm) and ethylene (5 sccm) for five minutes of growth, after which they were removed and processed. CVD using disperse catalyst particles is known to result in almost entirely individual nanotubes[29]. SWNT grown for this work have an average diameter of 0.97 nm (Fig. 2.1), further supporting this theorem.

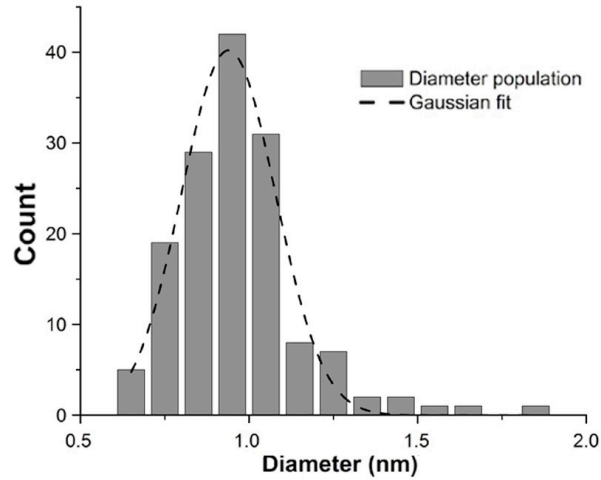


Figure 2.1 Diameter distribution of SWNT grown by CVD directly onto a substrate, measured by AFM[32].

2.3 The Carbon Nanotube Torsional Device

This thesis concentrates on a specific nanoelectromechanical device that utilizes an individual CNT as a torsional spring. The nanotube is suspended between two anchoring electrodes and supports a small metal block above the underlying substrate (Fig 2.2). This section will discuss the details of the fabrication process for this device architecture. Detailed methodologies pertaining to the particular equipment used in performing the experiments in this work is included in Appendix 2.

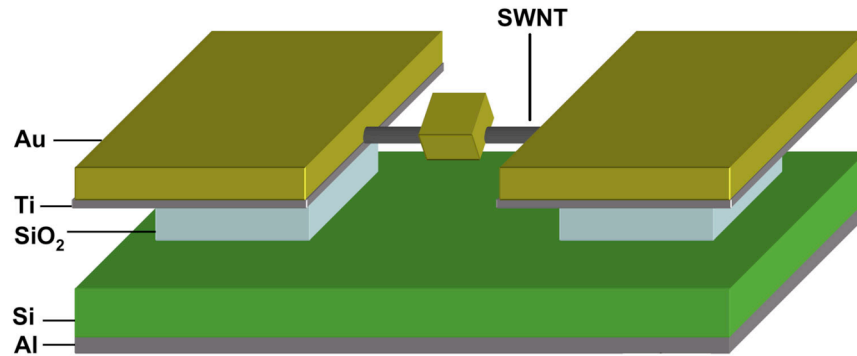


Figure 2.2 Schematic of the CNT torsional device, wherein a torsional platform is suspended on an individual CNT between two metal anchors over a gap

First, positive photolithography is performed on degenerately doped silicon wafers with thermally grown oxide layers of 0.6 to 1 μm . The procedure is commonly performed by spin coating a substrate (4000 rpm for 40 s.) with commercial photoresist (Shipley S1813). After baking the sample for 1 min. at 115 C to remove remnant solvent, it is allowed to cool before further processing. A mask aligner (Kasper) is then used to expose the resist to ultraviolet light (wavelength 365 nm) through a patterned glass mask. This has the effect of de-crosslinking the polymer network in the exposed regions and leaving them more susceptible to chemical treatment than unexposed areas. Exploiting this, a developer solution is then used to remove the de-crosslinked regions, resulting in a gutter to the underlying substrate in the otherwise unaffected resist. Following directional evaporation of metal (typically 10 nm Ti and 30 nm Au) onto the patterned wafer, all resist is removed with an acetone soak. Metal deposited atop the resist is removed with it, leaving substrate-bound areas only where exposure occurred. Negative photolithography, wherein exposed areas are crosslinked and metal remains in unexposed regions, can also

be performed to the same end using applicable resist and a negative mask, it was not used in this work

In this way, the surface is patterned with eight individually addressable macroscopic electrodes that decrease in size to a small $\sim 40 \mu\text{m} \times 40 \mu\text{m}$ area where devices are to be fabricated (Fig. 2.3). Following this, the backside of the substrate is cleared of its oxide layer using a Hydrofluoric acid (HF) etch and coated with Al, to form a backgate electrode. Samples are then subjected to a thermal anneal of 350° in order to aid Al migration into the Si, thereby improving contact. Following this, CNT are deposited on the substrate using one of the methods described in section 2.2. In the cases where CVD is used to grow SWNT, the photolithography step is performed after growth to avoid the adverse effects of exposing the metal patterns to high temperature. The thermal treatment of the backgate is also performed in an Ar environment to avoid oxidation of the nanotubes.

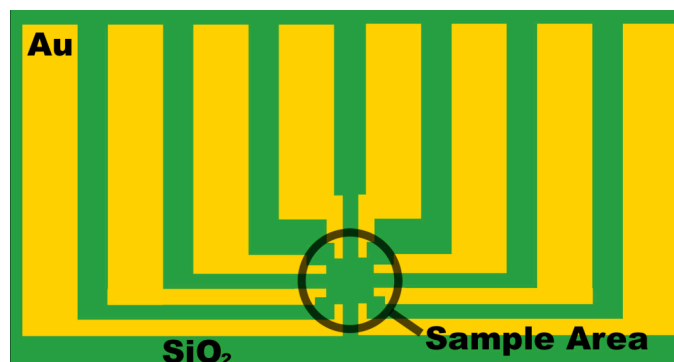


Figure 2.3 Schematic of the photolithography pattern with eight isolated leads

In these cases, there are also frequently CNT bridging multiple leads (Fig. 2.4a). These are removed before subsequent steps by applying large bias between neighboring

electrodes under ambient conditions until conductance paths became immeasurable. This is found to correspond to oxidation of the bridging tubes (Fig 2.4b). The deposited CNT are then located with respect to the patterned metal and imaged using a scanning electron microscope (SEM) (Hitachi S-4700 FE). These images are used to perform electron beam lithography (EBL) on the substrates (see section 2.4), fabricating large anchor contacts on either end of a CNT and individually addressable electrical contacts to the eight isolated metal leads (Fig 2.4c). This step of EBL is also used to pattern small fiduciary marks on the substrate, to be used in subsequent steps.

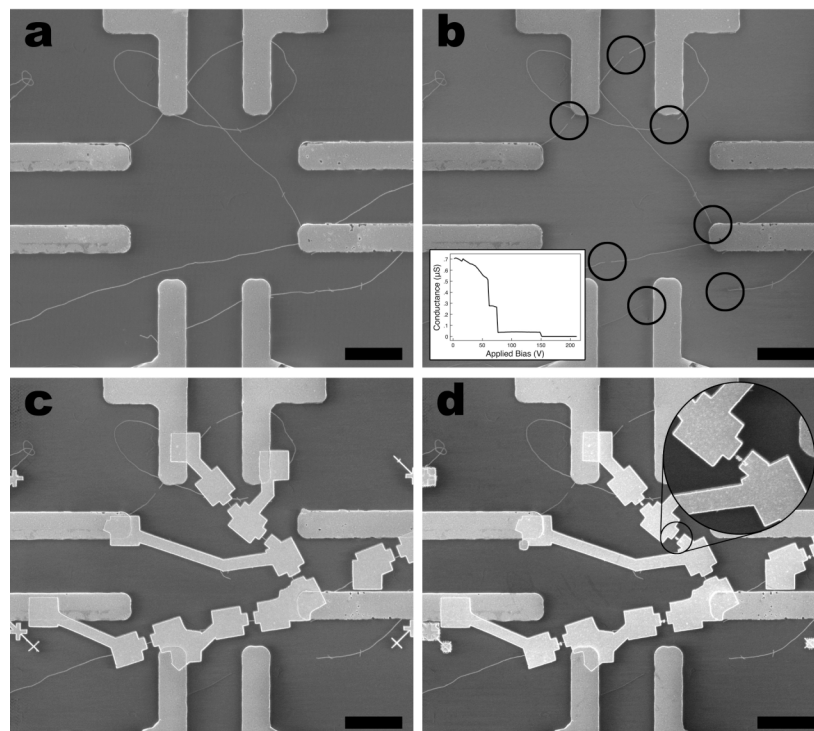


Figure 2.4 The fabrication process. (a) CVD-grown SWNT, connecting several overlying photolithographed leads. (b) Oxidative removal of connecting SWNT (circles indicate break points). Inset: representative conductance vs. applied bias between two leads. Each drop in conductance corresponds to removal of one or more tubes (more CNT connect leads outside of imaging field). (c) EBL-patterned anchors, contacts and fiduciary marks (cross-hairs). (d) EBL-patterned torsional platforms. Scale bars correspond to 10 μm .

Following metal deposition of the primary patterns, the device area is imaged once again to determine precise locations for all contacted CNT. A second step of EBL was performed to fabricate the small paddle structures onto the length of the CNT (Fig. 2.4d). This step is aligned to the electron-beam defined fiduciary marks for high precision and is used to pattern only the smallest features of the devices, in order to avoid detrimental effects of drift during pattern exposure. After metal deposition on the second patterning step, the substrate is exposed to a thermal anneal of 350-400 C under Ar flow, again, to prevent possible SWNT oxidation. This has the effect of thermally decomposing any remnant EBL resist polymer (and/or SDS, in pertinent devices) from the area between the nanotube and the contacting metal, resulting in improved contact. Following this, the sample is ready to be etched.

The substrate is coated with a single layer of polymethyl methacrylate (PMMA) ($M_w = 996k$), and standard EBL is used to define small squares over each device. Here, the patterned resist layer is used as an etch mask rather than a stencil for deposited metal. Buffered HF is then deposited onto the surface in order to chemically etch 0.5 to 1 μm of silicon oxide from it, depending on the original oxide thickness and, in some cases, the specific geometry of the devices. The PMMA protects the surface from the etchant everywhere except directly over the paddles, where the etch windows are defined. Devices can be fabricated successfully without using this extra step of EBL, but it is found that the procedure decreases possible leakage current between devices and the backgate electrode and makes the final devices more robust.

Following etching, the substrate is submerged in acetone to remove the PMMA layer and then immediately dried using supercritical CO_2 . This prevents the devices from

being exposed to surface tension effects during evaporative drying, which generally cause them to fail. The final device is then complete (Fig 2.5) and ready for experimentation.

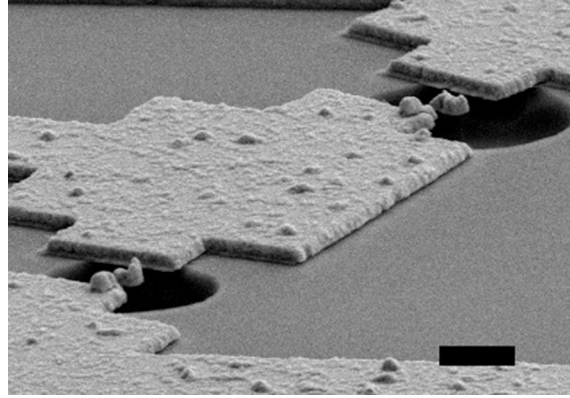


Figure 2.5 Two fully suspended devices, viewed at approximately 30° to the substrate. Scale bar represents 1 μm .

2.4 Electrically Contacting Nanotubes

Obtaining low resistance electrical contact to SWNT is a difficult problem and has been the subject of much research. Many methods have been examined, such as choice of contacting metal[21] and using top- and bottom-contacts[33]. The work presented in this thesis uses a bilayer resist method and an annealing process to achieve low resistance electrical contact. The methods will be reviewed here; Appendix 2 gives step-by-step instructions of how they were performed.

EBL is used to define contacting leads to individual nanotubes. EBL is very similar to photolithography, discussed in the previous section, except that PMMA is used as a resist. This polymer is sensitive to incident electrons in much the same way positive photoresist is sensitive to ultraviolet light, as exposure results in the de-crosslinking of the polymer. Development is then performed by using a 1:3 mixture of methyl isobutyl

ketone in isopropanol. Through the use of a SEM electron beam as an exposure source, however, the attainable resolution of patterns is drastically improved over photolithography, which is limited by the wavelength of the light. EBL can reliably produce sub-100 nm features, spatially positioned within 100 nm of a target area.

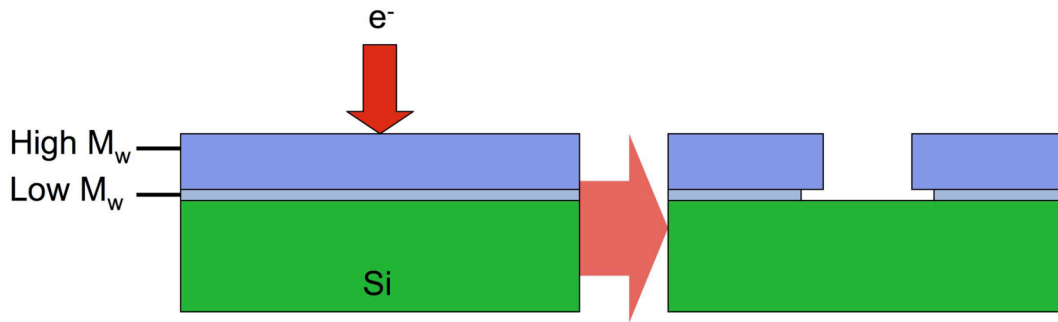


Figure 2.6 Use of bilayer PMMA for electron beam lithography, resulting in desirable T-structure (right) and low remnant material on the surface

Common EBL resist is made using PMMA of $M_w = 996k$, but lower molecular weight polymer is more sensitive to electron beam exposure. Therefore, EBL can be performed on a bilayer resist composed of a layer of low M_w (350k) PMMA beneath a layer of standard M_w material (Fig. 2.6). Each type of PMMA are prepared by making a 4% (wt.) solution of dry polymer in chlorobenzene. After being allowed to dissolve completely, a clear, only slightly viscous liquid results. The resist is deposited on a substrate via spin coating. Low M_w is deposited first, at a spin speed of 5000 rpm, and then subjected to a soft bake (180°C) for 2 minutes on a hot plate. This drives off remnant solvent and allows for a solid surface on which to deposit the second resist layer. High M_w PMMA is then spun at 4000 rpm, after which the sample is baked for ~ 1 hr. at 180°C , this time using a tube furnace or enclosed oven. Application of ambient heat

results in more consistency within the layers and extended baking time is used to ensure total removal of solvent.

The resulting devices incorporate the high-resolution device patterning of conventional EBL with decreased remnant resist left on the underlying surface (and nanotubes). Thermal evaporation is used to deposit first an adhesion layer (typically 5-10 nm of Cr or Ti) and then a thicker contact layer (typically 80 nm Au) onto the patterned substrate. This is followed by a thermal anneal under Ar flow (see Section 2.3). Following this thermal treatment, SWNT contact resistances are generally found to be on the order of 100 k Ω , although values slightly lower than this have been measured.

Experimental Measurement of Single-wall Carbon Nanotube

Shear Moduli

You can observe a lot just by watching

-Yogi Berra

3.1 Introduction

One aspect of carbon nanotubes that make them attractive candidates for use in devices and composite materials is their amazing mechanical properties. As discussed in Ch. 1, they have larger mechanical moduli than diamond, making nanotubes the strongest material known. But, whether being used individually or *en mass*, the ultimate strength of any system incorporating CNT is linked to the strength of the individual tubes.

A number of investigations have measured the axial and bending strength of CNT. These investigations have primarily utilized techniques of oscillatory behavior and direct scanning probe manipulation and measurement. The former initially concentrated on monitoring thermal vibrations of cantilevered CNT with transmission electron microscopy (TEM) (Fig. 3.1a) and utilized MWNT or short SWNT, due to persistence length issues. By fitting the thermal amplitude over a range of temperatures, values for the Young's modulus, Y , were extracted. For MWNT of various diameters, Y ranged from 0.4-4.15 TPa with an average value of 1.8 TPa[8]. Similar measurements on short SWNT

yielded a similar range, though averaging to a lower ($1.3 -0.4/+0.6$) TPa[6] while doubly clamped CVD SWNT (Fig. 3.1b) showed Y ranging from 0.02-2.6 TPa[4]. While these experiments overlapped with theoretical expectations, they contained obviously large error ranges.

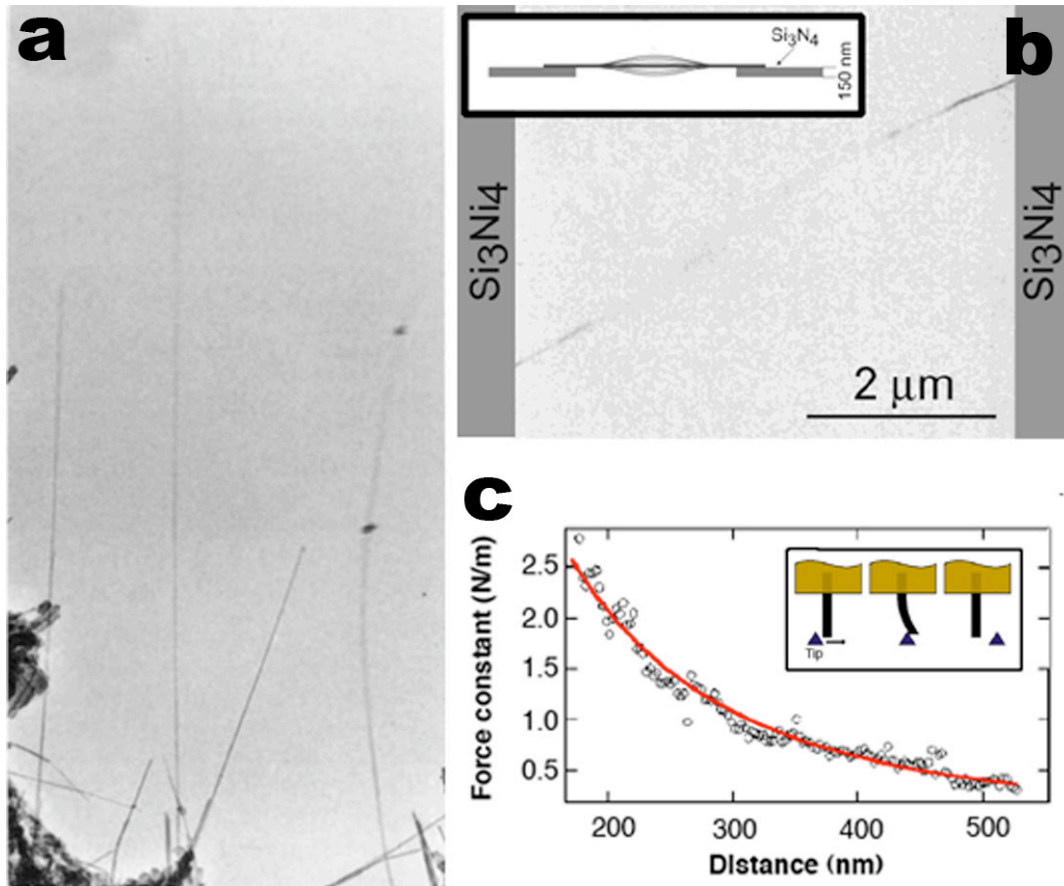


Figure 3.1 Thermal excitation of (a) a cantilevered MWNT[8] and (b) a doubly-clamped CVD SWNT[4] (inset: side view schematic). (c) Direct lateral scanning probe measurement on a cantilevered MWNT[9] (inset: manipulation schematic).

Driven oscillations further elucidated the experimental measurement of Y . The methods used for this will be discussed in greater detail in Ch. 5, but the resonance frequency of individual oscillating CNT were measured and could be related to the Young's modulus of the material through geometric values. MWNT of various

diameter[7, 34] and apparent quality[5] demonstrated a range of Y that was generally around 1 TPa with an inverse relation to diameter.

The most direct measurements, however, are the use of an atomic force microscope (AFM) to directly contact individual CNT. Lateral Force microscopy of cantilevered MWNT (Fig. 3.1c) revealed $Y=1.28 \pm 0.59$ TPa[9]. Force measurements on SWNT ropes[35, 36] indicated values around 1 TPa with a bundle diameter dependence that decreased Y at larger diameters. Similar measurements on individual SWNT[37] yield values in high agreement with both the low diameter limit of the bundle values and theoretical expectations.

While reasonably consistent across many material growth methods and measurement techniques, all previous studies have concentrated on axial strength as it is the most accessible dimension in which to actuate or apply strain. The nanoelectromechanical torsional device offered the first real ability to examine the third straining mode- that of twisting.

The first measurements of this kind were performed on MWNT[14, 38], due to higher device stability and higher measurement threshold. Torsional devices were fabricated on individual MWNT and torsional properties were investigated through scanning probe measurements with a hybrid AFM/SEM system (Fig. 3.2a). Scanning probe-based force measurements require a probe spring constant matched closely to that of the object being measured, so the MWNT devices were studied with cantilevers of spring constant ~ 1 N/m. Values for measured shear moduli (Fig. 3.2b) agreed qualitatively with expected theoretical values of ~ 0.5 TPa[2]. More interestingly, however, a systematic increase in this measured value was found as the devices were

subjected to continued deflections (Fig 3.2c). This increase eventually saturated after hundreds of deflections. While several possible reasons for this effect were considered, including the result of imaging-beam induced contamination and changing mechanical contact at the points of CNT pinning, it was ultimately attributed to increasing interactions between the multiple graphitic shells that make up the MWNT. While some theoretical work supported this hypothesis[39], it was difficult to experimentally verify.

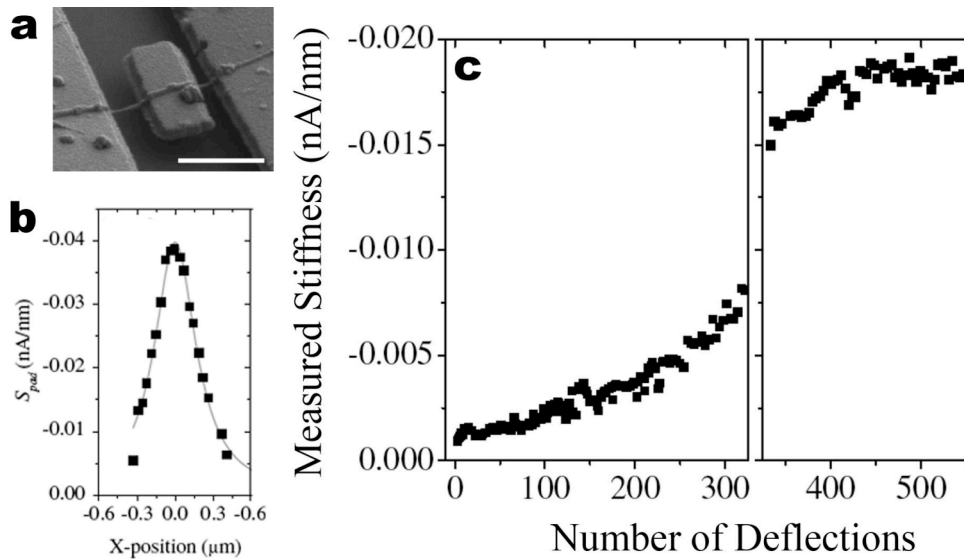


Figure 3.2 Dependence of MWNT stiffness (measured by AFM; units of photodiode signal intensity per piezo distance) on number of deflections (from [14])

Further work on the MWNT-based torsional system utilized the paddle as an oscillator[40]. This work was performed by Papadakis, *et al* with contributions by the author of the current thesis. Here, devices were excited electrostatically (discussed later in this chapter) and deflection was measured with an optical interferometer at a pressure of $\sim 10^{-5}$ Torr (Fig. 3.3a). While DC deflection (see next section) was observed (Fig. 3.3b), the work concentrated on the frequency-dependent behavior of the system. In order

to drive the oscillations, a small, variable-frequency alternating signal was added to a DC offset and applied to the underlying substrate. In this way, it was shown that MWNT devices exhibit amplitude-dependent resonant torsional oscillations on the order of 1 MHz (Fig. 3.3c and d). This behavior will be discussed further in the next chapter.

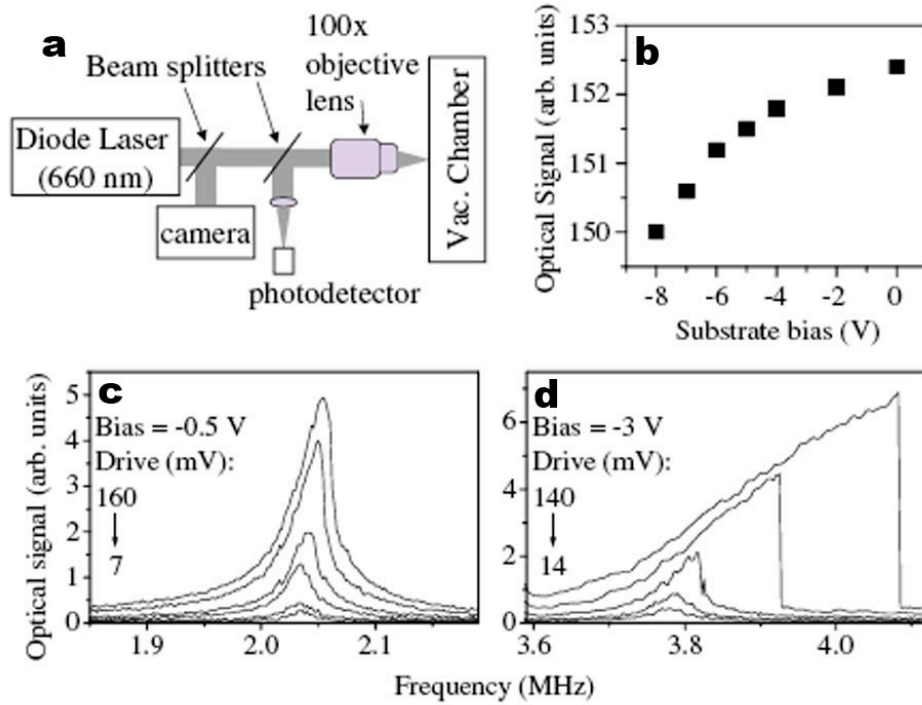


Figure 3.3 (a) Schematic of the optical interferometer setup. (b) Measured DC deflection of a MWNT device and the resonant behavior of two devices showing both symmetric (c) and overdriven peaks. Bias is the applied DC component while the drive voltage is the amplitude of the oscillating signal. From [40], by Papadakis, Hall, *et al.*

Because the resonance frequency F_o is related to the torsional spring constant K_θ by $K_\theta = (2\pi F_o)^2 I$, where the moment of inertia I of the paddle is estimated from direct geometric measurements of SEM images. From this, information inherent to the MWNT itself can be gained via the relation

$$K_{\theta} = \frac{\pi(r_{out}^4 - r_{in}^4)G}{2l} \quad (\text{Eq. 3.1})$$

where G is the CNT shear modulus, l is its exposed length and r_{out} and r_{in} are its outer and inner radius, respectively. While l and r_{out} could be directly measured, r_{in} could not, and in any event, the previous scanning probe-based measurements made it unclear how much interaction would occur between shells. Therefore, two limiting values for shear modulus were calculated: G_e , the solid rod model, and G_s , the thin shell model.

Device	Diameter (nm)	ω_o (MHz)	G_e (GPa)	G_s (GPa)
1	12	1.68	90	570
2	27	2.37	35	460
3	28	2.50	54	740
4	35	3.27	33	560
5	16	2.92	435	3420
6	20	3.79	290	2880
7	18	4.12	565	5000
8	22	2.98	200	2190
9	21	2.04	120	1200

Table 3.1 Measured values of diameter and resonant frequency (ω_o) for nine MWNT devices and shear moduli for each, calculated with the solid rod model (G_e) and the thin shell model (G_s). Details in text. From [40], by Papadakis, Hall, *et al.*

In the first model, total interaction among shells is assumed all the way to the center of the tube, while in the second, it is assumed that only the outermost shell is being torqued. From this, values for nine devices were gathered (Table 3.1). Interestingly, for

about half of the MWNT, G_e agreed best with experimental values while for the other half, G_s was in agreement. For one device, neither value was particularly close. This was taken to indicate that there could exist varying amounts of interaction amongst interior MWNT shells regardless of the number of deflections, as even the devices that indicated no interaction were actuated many millions of times. Therefore, the increasing interaction between shells (starting from the outermost and working inward) may continue through all layers or may stop at some particular layer. The reasons for this are unclear but may be related to specific registry between given shells or defect sites.

One way to examine this phenomenon would be to study devices built on CNT of fewer shells, the lower limit being SWNT, thus removing inter-shell interactions from the system. This also would allow for experimental verification of the theoretical torsional mechanical properties of these simpler systems. However, some aspects of the experimental method make its application to SWNT difficult. Chief among them is the expected torsional spring constant, K_θ . Because of the large dependence of this value on nanotube radius, the spring constant of a SWNT device ($r_{SWNT} \sim 0.5$ nm) is expected to be much lower (up to six orders of magnitude) than that of a similar device based on a MWNT ($r_{MWNT} \sim 15$ nm). As mentioned above, spring constant matching is required for reliable scanning probe-based force measurements. The weakest commercially available cantilevers are only as low as $\sim .001$ N/m, making such measurements on SWNT devices difficult if not impossible. Further, interferometry was made difficult by a feature of the fabrication method of SWNT devices, as follows. Due to the lower rigidity of SWNT, turbulence during the drying procedure or indeed even thermal energy[41] can cause relatively large deflections of the device. For this reason, the paddle itself must be made

much smaller than those built on MWNT in order to prevent it from touching the underlying substrate, after which Van der Waals forces make detachment impossible. This decrease in paddle surface area made optical measurements with the interferometer (spot size $\sim 0.7 \mu\text{m}$) difficult. Therefore, a new method must be used to advance these experiments. This chapter details this new method and the results obtained through its use.

3.2 Experimental Methods

An alternate to scanning probe actuation of the torsional device is electrostatic force actuation[42], which uses the underlying doped silicon wafer as a counter electrode to the torsional platform itself. In order to make the imaging of such actuation quantitative, the following methodology is used.

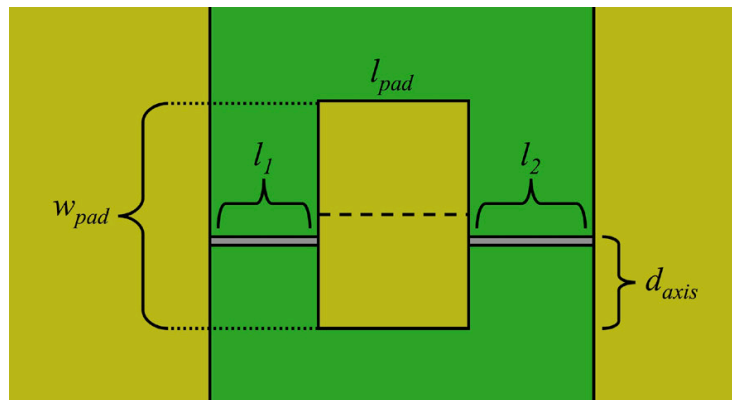


Figure 3.4 Schematic of a torsional device (viewed from above) detailing the geometric values attainable from a SEM image.

For a given device, a series of SEM images are taken perpendicular to the substrate. First, an image is taken of the device prior to actuation, from which device dimensions including SWNT lengths (l_1 and l_2), paddle length (l_{pad}), paddle width (w_{pad})

and distance to axis of rotation (d_{axis}) are obtained (Fig. 3.4). After this, successive images of a device are taken at various static positions (that is, at various constant applied backgate voltages, and thus constant electrostatic forces). For each of these images (Fig. 3.5a), the degree of deflection can be calculated from the projected image length of the paddle. For a given applied bias n , the apparent paddle width w_n is measured. Using w_n , the deflection angle can be deduced geometrically through the relation

$$\theta_n = \cos^{-1}\left(\frac{w_n}{w_0}\right) \quad (\text{Eq. 3.2})$$

as shown in Fig. 3.5b. Here, w_0 is the width of the non-actuated paddle and θ_n is the deflection angle at n applied volts.

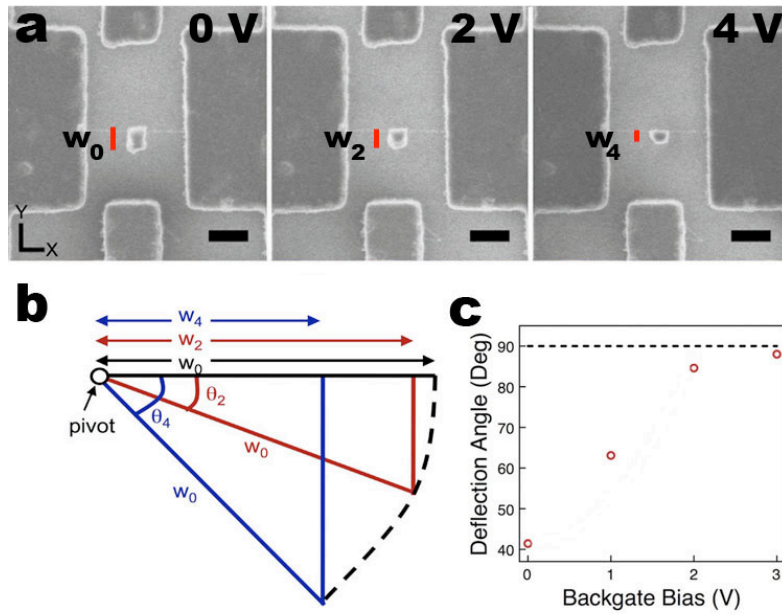


Figure 3.5 (a) SEM images of a device viewed from above and labeled with apparent paddle width (red lines) at three actuation biases (scale bar= 500 nm). (b) Geometric relation between apparent paddle widths and deflection angle. (c) Applied backgate voltage vs. measured paddle deflection for a typical device. Dashed lines represent quadratic fit to data and maximum angle attainable with this device (90°)

This results in a quantitative relation between applied bias and deflection for each device (Fig. 3.5c). It is notable that these devices have a maximum deflection angle of nearly $\pi/2$ radians, or perpendicular to the substrate. This is because the paddle is thin and asymmetric to the SWNT axis, placing the centroid of charge on nearly the same z plane as the tube prior to deflection. When the centroid is between the nanotube and the gate electrode, increased electrostatic attraction force can only contribute to lateral force rather than torque. In later devices, the maximum deflection was increased to nearly π radians through simple geometric means that will be discussed in Ch. 4.

3.3 Device Modeling and Analysis

With the quantitative information from analysis of the static images (Fig. 3.5a) and AFM measurements of actual etch depth, an accurate computer model of each actuated device was built (Fig. 3.6). These models included both precise location of device components in relation to one another as well as inherent properties of the materials used (for instance, the permittivity ϵ of SiO_2 compared to that of vacuum). The SWNT itself, however, is not included in the model as it was assumed from its size that it did not perturb the field significantly. Also not included in the model were slight irregularities, such as in metal edge smoothness, (as these were assumed to average out) and oxide surface states, which will be discussed in the next section. The computer model was then used to perform Finite Element (FE) analysis of the device in question. Examples of the calculated electric potential of a typical device are shown in Fig. 3.6.

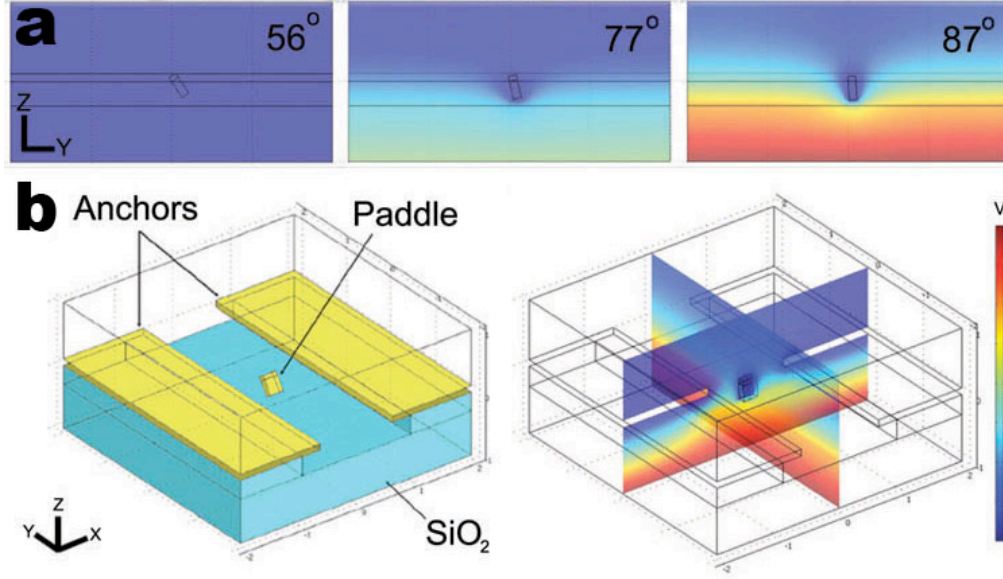


Figure 3.6 (a) FE calculated electric field potential at three deflection angles (viewed along the nanotube axis). These correspond to the SEM images in Fig. 3.5a. (b) Labeled FE model and overlaid color map of FE calculated electric field potential. Full color scale is 4 V. From [32], by Hall, *et al.*

From this simulation, surface charge density (ρ) at each point on the surface of a paddle is calculated through

$$\rho = \epsilon_0 \vec{E} \cdot \hat{n} \quad (\text{Eq. 3.3})$$

where ϵ_0 is the vacuum permittivity, \hat{n} is the local unit vector perpendicular to the paddle surface and \vec{E} is the electric field calculated with the FE program. The force on an infinitesimal area dA of the paddle surface is

$$d\vec{F} = \rho \vec{E} dA \quad (\text{Eq. 3.4})$$

The paddle is a conductor, so the incident electrostatic field $\vec{E}_{surf} = E\hat{n}$ must be normal to its surface. Therefore

$$d\vec{F} = \frac{1}{\epsilon_0} \rho^2 \hat{n} dA \quad (\text{Eq. 3.5})$$

The portion of the total torque on the paddle contributed by dA is $d\vec{T} = \vec{R} \times d\vec{F}$ where R is the distance of dA from the SWNT axis. Therefore, the total electrostatic torque on the paddle is given by the surface integral

$$T = \frac{1}{\epsilon_o} \int_{\text{surface}} \rho^2 \vec{R} \times \hat{n} dA \quad (\text{Eq. 3.6})$$

The model of the paddle has six distinct surfaces (Fig. 3.7a) on which individual calculations can be performed to obtain the contribution of each to the net torque. Four faces of the paddle (top, bottom and two ends) experience forces that contribute to this net value. Forces on the sides of the paddle (facing the anchors) have no component perpendicular to the axis of rotation and thus do not contribute. It was found that the contribution of one surface for this paddle shape (surface 4) dominates the total torque acting on the system (Fig. 3.7b). Nonetheless, the electrostatic torque calculation was the sum of the surface integrals of all six surfaces.

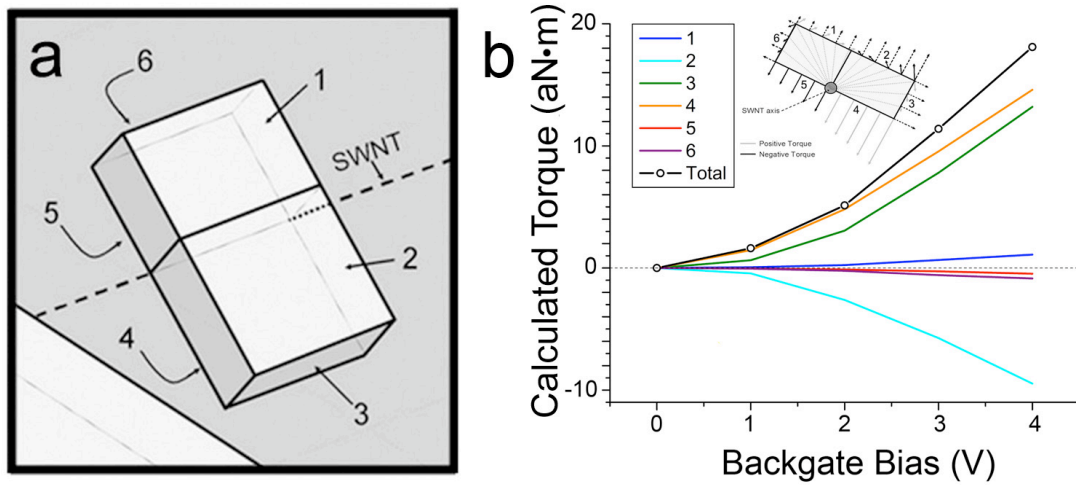


Figure 3.7 (a) Diagram[32] showing the six relevant faces in the FE model. (b) Calculated total torque and incremental torque acting on each face of a typical device for multiple applied biases. Inset: Electrostatic forces (dashed lines) and the components of those forces acting as a torque on each face. Light gray lines indicate moment arm relative to axis of rotation.

The net torque, T , varied with the applied bias, but was typically on the order of 10^{-18} N m for the devices studied. This value is related to the shear modulus, G , of the SWNT spring through the equation[43]

$$G = \frac{T(l_1 + l_2)}{r^3 t \pi \theta} \quad (\text{Eq. 3.7})$$

where l_1 and l_2 are the nanotube length to the left and right of the paddle, respectively, r is the nanotube radius, θ is the deflection angle and t is the wall thickness. The value used for t was 3.4 Å- an estimate of the graphene thickness based on the distance between layers in bulk graphite[2]. Other theoretical treatments[44] of SWNT use a thickness value as low as 0.66 Å. Error resulting from this would be negligible compared to error from other sources, such as the measurement of nanotube radius (see next section).

3.4 Results and Discussion

The resulting data showed the torsional spring behavior of individual SWNT (Fig. 3.8a). By averaging all measured values for a particular device, we arrive at a value G for the SWNT that it was built upon. For larger applied torque, T , the measured deflection angle increased linearly, indicating Hookean behavior (following $T=K_\theta\theta$). A plot of shear modulus G - related directly to K_θ , via eq. 3.1- at each deflection is shown in the inset of Fig. 3.8a, confirming this behavior. As the deflection limit of 90° is approached, the measurements deviate slightly from linearity, but are still within the error bars.

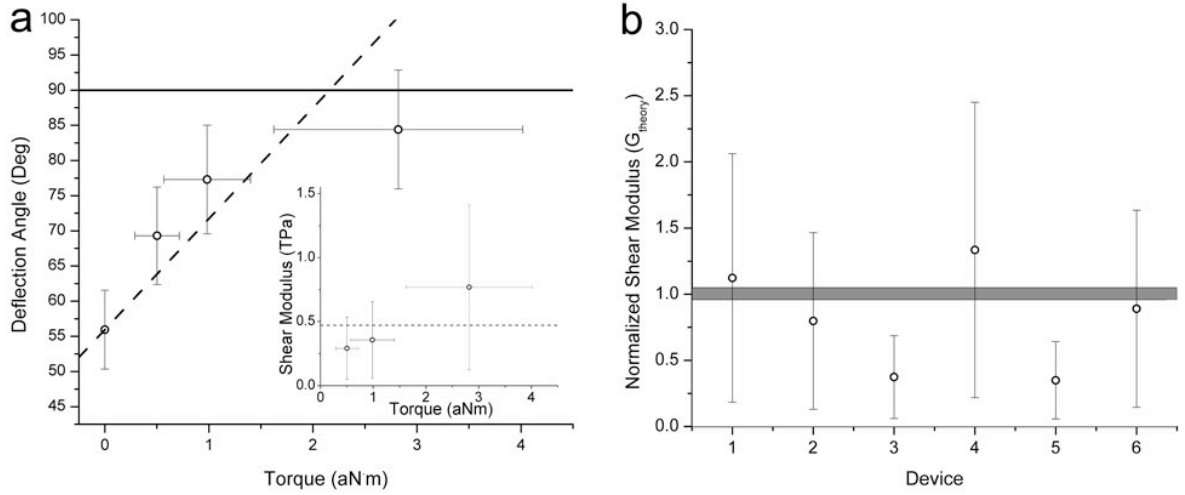


Figure 3.8 (a) Deflection angle vs. FE calculated torque for device 6 where 90 is the maximum deflection. Inset: Measured shear modulus vs. FE calculated torque for the same device. (b) Average SWNT shear modulus for six devices. Values are normalized to the average theoretical value (0.455 TPa) and the shaded region represents the range of values over all chiralities from Ref. [2]. Figure from [32], by Hall, *et al.*

As shown in Fig. 3.8b, the inferred values are in agreement with theoretical predictions[2]. The average value for the shear moduli of all devices is $G = 0.41 \pm 0.36$ TPa. The inset in Fig. 3.8a, shows that there is no detectable nonlinearity in the response, and from theoretical analysis[44], none is expected for the levels of strain applied here ($< 0.1\%$). This merely indicates that the SWNT is not twisted enough to cause kinks in its cylindrical structure. Such an occurrence would be manifested as a large and sudden drop in the measured shear modulus due to a drop in the strain energy (Fig. 3.9a). In fact, the critical twisting angle before basic tube buckling should be[44]

$$\theta_c = 2(1 + \nu)\pi \quad (\text{Eq. 3.8})$$

where ν is Poisson's ratio (~ 0.2). Such deflections are unattainable by any SWNT torsional system fabricated for this work.

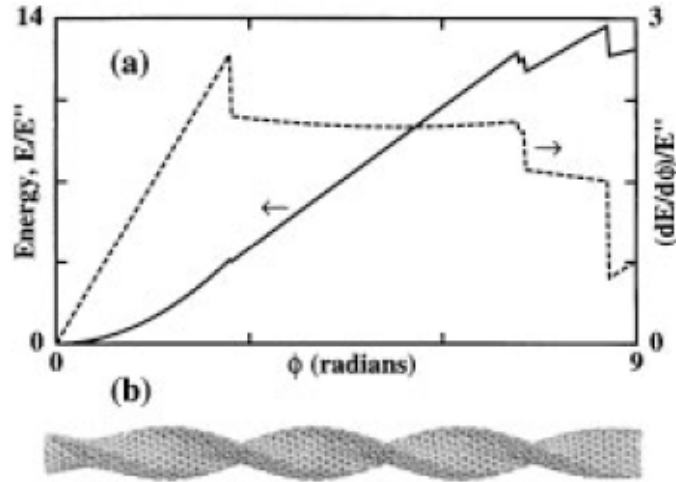


Figure 3.9 (a) Calculated strain energy for increasing deflection angle of a 23nm long, 1nm diameter SWNT. (b) Helical buckling pattern expected above 2.7 rad. Longer SWNT sections (like those found in the torsional device) would require even larger deflections before buckling occurs. From [44].

The largest error in the shear modulus measurements stems from the inability to measure the diameter of each SWNT accurately once the devices are suspended. Calculations are performed using a diameter equal to the measured mean diameter of the starting material ($0.97 \pm 0.2\text{nm}$). From measured distribution (see Chapter 2), we expect 20% error, accounting for about 95% of all nanotubes on the surface. Differences in radii alone may be able to explain the statistical variation of shear modulus from one SWNT to the next. Other sources of error can be found in the dimensional measurements taken directly from SEM images and shape variation of the paddle, each about 10%. The significantly lower moduli (of samples 3 and 5, for example) could be due to increased defect density in those specific SWNT, or to the diameters' being slightly more than one standard deviation above the mean.

A final source of error lies in the possible surface states of the etched silicon oxide that underlies the device, as discussed in section 1.4. Eq 1.12 can be used to

quantify the effect of surface charge on the etched device, setting z equal to the 1 μm oxide thickness. The permittivity ϵ is set as $(0.6\epsilon_{\text{oxide}}+0.4\epsilon_o)$ to account for the remaining oxide as well as the etched gap. The resulting potential difference (assuming a surface charge density ρ of 10^{10} q/cm^2) is $\sim 0.34 \text{ V}$, corresponding to an error in the bias of only about 5%. The actual surface charge density may be significantly lower due to charge passivation from being exposed to ambient conditions.

Following DC actuation measurements, further investigation to deduce the cause of MWNT shear strengthening (section 3.1) was performed. An oscillating signal was applied to one device with a low frequency ($<1 \text{ Hz}$) and of large enough amplitude to deflect the device to nearly 90° . The imaging beam was turned off for this procedure in order to remove any perturbation it may have caused. After several hundred cycles, the procedure to measure shear modulus was performed again. Despite the repeated deflections, the device showed no measurable change in reaction to applied field, giving the indication that the history-dependence of G is not present in similar systems built on SWNT. This supports the theory that the hysteretic behavior may be a product of interaction between interior graphene layers since none are present in the simplest single-shell case. This will be the subject of future work with these devices (see Chapter 6).

Electromechanical Response of Single-wall Carbon Nanotubes to Applied Torsional Strain

Any sufficiently advanced technology is indistinguishable from magic.

-Arthur C. Clarke

4.1 Introduction

It is well established that individual SWNT can exhibit a wide range of transport properties based upon their specific crystal structure (see section 1.4). But perhaps even more interesting than this is the anticipated dependence of the transport properties of a particular SWNT on external stimuli, such as strain. This phenomenon offers a means by which to monitor pertinent stimuli on the nanometer scale and opens the door for integrated nanoelectromechanical devices.

The effect of strains on the properties of nanotubes has been widely studied in theory[45-50]. The effect of inducing strain on the carbon bonds is a distortion of the lattice from the graphene ideal that causes a shift of the Fermi points in relation to the allowable energy bands. It is the localization of the Fermi points with these 2D energy bands (k states) that is the prime factor deciding the band structure of the tube in question. Because the periodicity of the allowable energy bands is strongly correlated to the diameter of the tube (in so much as it depends on electron wavelengths that can fit around the circumference of the tube) and because this diameter is not strongly affected

by applied strains- especially small strains[49]- it is not a shift of these bands that is responsible for the expected change.

In 2000, Yang and Han[50] used a Hückel tight-binding (TB) Hamiltonian to elucidate the effects of strain on the SWNT graphitic lattice. Similar calculations had previously been used to successfully predict the band structure of unstrained tubes[51, 52] and here was used with the addition of a 2D strain tensor $\varepsilon=(\varepsilon_{ij})_{2 \times 2}$.

The Hückel TB model for Fermi point k_F takes the form of $H(k_F) = \sum t_j \exp(ik_F \cdot a_{j0})$, where a_0 is the carbon-carbon bond length and the sum is over $j=1,2,3$ for the three bonds to a given carbon atom. The variable t_j is a Harrison hopping parameter of the form $t_j=t_0(r_j/r_0)^2$ that accounts for the change in electron transport due to the deformed bonds (t_0 is the tight-binding overlap integral, 2.7 eV). $H(k_F)$ is an energy term and is also equivalent to density of states energy $E(k_F)$, which will be important in the relation to the band structure. The expansion of $|H(k_F)|=0$ to first order yields expressions for the circumferential shift in Fermi energy, Δk_F^c :

$$\Delta k_F^c a_0 = (1 + \nu)\sigma \cos 3\theta + \gamma \sin 3\theta \quad (\text{Eq. 4.1})$$

where ν is Poisson's ratio, σ is axial strain, γ is torsional strain, and θ is the chiral angle. Through the use of energy equivalence (mentioned above) to find band energy for the initial k_F location[51] and the strained location, a relation of applied strains to the gap energy (between the first van Hove singularities, quantum number =1) is arrived at, of the form:

$$\Delta E_{gap} = \text{sgn}(2p + 1)3t_0[(1 + \nu)\sigma \cos 3\theta + \gamma \sin 3\theta] \quad (\text{Eq. 4.2})$$

Here, the variable p has a value of -1,0 or 1 such that $n-m=3q+p$ is fulfilled, where q is an integer and m and n are the SWNT lattice indices. For semiconducting tubes, $p=\pm 1$,

which means that the expected change in band gap can be either positive *or* negative. Metallic tubes ($p=0$) can only exhibit positive change, as required by their initial zero energy gap. The effect of both axial and torsional strain on the gaps of several types of SWNT is shown in Fig. 4.1.

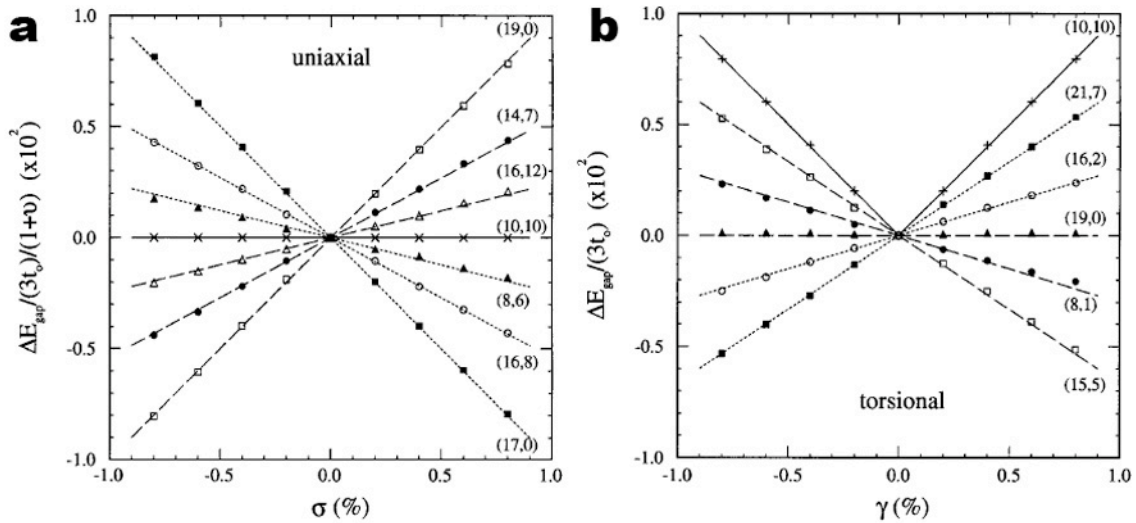


Figure 4.1 Theoretical dependence of SWNT band gap on (a) uniaxial and (b) torsional strain[50].

Prior to this, experiments were being performed to probe the effects of applied strain on nanotubes conductivity. Early atomic resolution scanning tunneling microscopy[53] observed a localized twist in a SWNT confined to a rope and speculated that such deformations could cause a semiconducting behavior observed in bundled material. In the earliest direct measurements[54], surface-bound MWNT were contacted on either end and a scanning probe was used to manipulate the tube laterally across the surface. While a repeatable and measurable change in resistance was observed, rigorous investigations on the levels of strain were not completed. While the results were somewhat frustrated by several aspects (including contact stability, surface interactions

and the use of the more complex MWNT system), they remain the first observable consequences of strain on nanotube transport.

In later experiments, scanning probes were used elegantly to apply strains vertically to suspended SWNT. First, simple displacement dependence of an individual tube's resistance was demonstrated with high reproducibility[55]. Soon after, the use of the scanning probe as a means by which to apply strain was extended to use as a gate electrode in order to characterize the transport characteristics of a given SWNT[56]. The latter work contains a quantitative treatment that will be reviewed here.

To relate the measured resistance of a tube to its band structure, thermal excitations across the gap were considered and contributions of tunneling were neglected. For carriers of energy E such that $(E-E_F) > E_{gap}$, excitation across the gap will occur with a transmission probability $|t|^2$, while those with energy $(E-E_F) < E_{gap}$ cannot cross. The resulting relation was of the form

$$R = R_c + \frac{1}{|t|^2} \frac{\hbar}{8e^2} \left[1 + \exp\left(\frac{E_{gap}}{KT}\right) \right] \quad (\text{Eq. 4.3})$$

where R_c is the contact resistance in series with the SWNT. This is intended to hold for low bias source-drain measurements, where optical phonons, etc. are not a factor.

The work in question found a distinct correlation between applied axial strain and transport properties and, importantly, observed different responses from different SWNT (Fig. 4.2). This result is in line with the previously mentioned theoretical works, which expect a dependence of the reaction on initial lattice arrangement. Agreement with the above exponential behavior was also observed (Fig. 4.2 insets), confirming its validity.

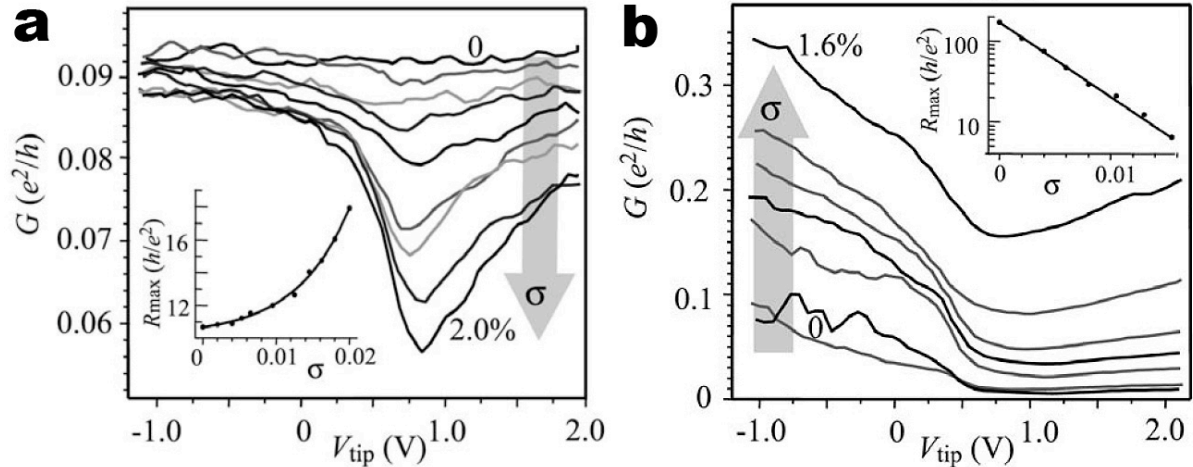


Figure 4.2 Experimental response of SWNT transport to axial strain for two different samples, demonstrating both (a) increasing and (b) decreasing resistance with added strain[56].

Several other experiments followed these works, exploring aspects of metallic/quasi-metallic/semiconducting tube response[57] and application to strain sensing technology[58]. However, these continued to concentrate on axial strain.

The first study of torsional strain effects on transport were performed in 2006[59] on a system similar to the one presented in this thesis. In this work, suspended paddle elements were fabricated on MWNT and actuated directly with a scanning probe in a similar fashion to previously published methods[14]. Here, however, low-bias (10 mV) source-drain resistance was monitored during the actuation. In the resulting measurements, an oscillatory behavior was observed in the transport properties as the probe tip exerted a torque on the MWNT (Fig. 4.3). This was attributed to movement of the Fermi points through a number of allowable k states, the spacing of which were assumed narrow due to the large diameter of the tube. Total loss of conductance was also recorded at large deflection and attributed to breakage of the tube.

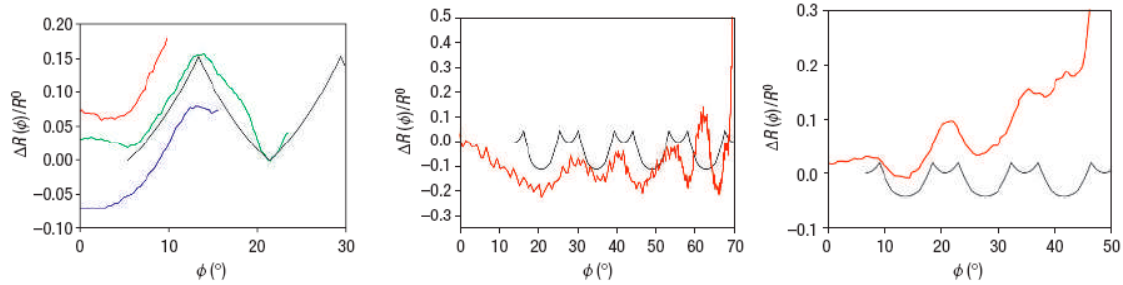


Figure 4.3 Oscillations in MWNT transport measured experimentally with a torsional device geometry[59].

Issues, however, abounded with this experimental setup, the most notable of which was the use of MWNT. During the course of the experiment, it was assumed that *all* transport occurred through the outermost graphene shell and that at no point did interior shells interact, even at large deflections. This was not supported by some previous work[14], although, as mentioned in section 3.1, varying degrees of interaction probably exist for different MWNT. The use of the scanning probe as a means by which to apply the strain may have also been problematic, allowing for possible perturbations due to additional charges, tip contact stability, etc. The work presented in this chapter seeks to remedy- or at least to lessen- these concerns and build upon the work covered briefly in this section.

4.2 Experimental Methods

Torsional devices were fabricated in the method detailed earlier in this thesis (section 2.3), ensuring the best electrical contact possible was achieved (section 2.4). CVD-grown SWNT were used in the process, immediately simplifying the experiment from its MWNT-based forerunner. Geometrically, the exposed length of SWNT on either side of the paddle was purposefully kept small by using high-resolution EBL techniques.

Lengths as low as 100-150 nm could be reliably attained in this way. The reason for this was to maximize the amount of torsional strain applied to the tube for a given rotation of the paddle as torsional strain in the SWNT sections goes as $\gamma=r\theta/l$, where r is radius, θ is paddle deflection and l is the tube section length.

The paddles were actuated using electrostatic attraction forces (Ch. 3), replacing the scanning probe method of strain application and its perturbative effects mentioned in the previous section. The paddle itself was fabricated in such a way that its thickness was large compared to its width (in the direction perpendicular to the tube axis). In previous thinner devices (see section 3.2), the maximum deflection attainable was about $\pi/2$ radians because the centroid of charge was at nearly the same initial height as the SWNT axis (Fig. 4.4a); the fact that it was off-axis was the main cause of the torque. Thicker paddles shift the centroid above the axis of the nanotube, thereby allowing for deflections of nearly π radians (Fig. 4.4b).

As discussed in section 1.4, surface charges on the underlying substrate can add uncertainty to the gate bias values, and since a larger amount of oxide is removed in the etching of these devices than was for the devices presented in the previous chapter, the uncertainty could be somewhat larger. Assuming total removal of the oxide, the potential resulting from surface states could be as much as 0.9 V. Again, though, passivation is not accounted for, making this a maxima.

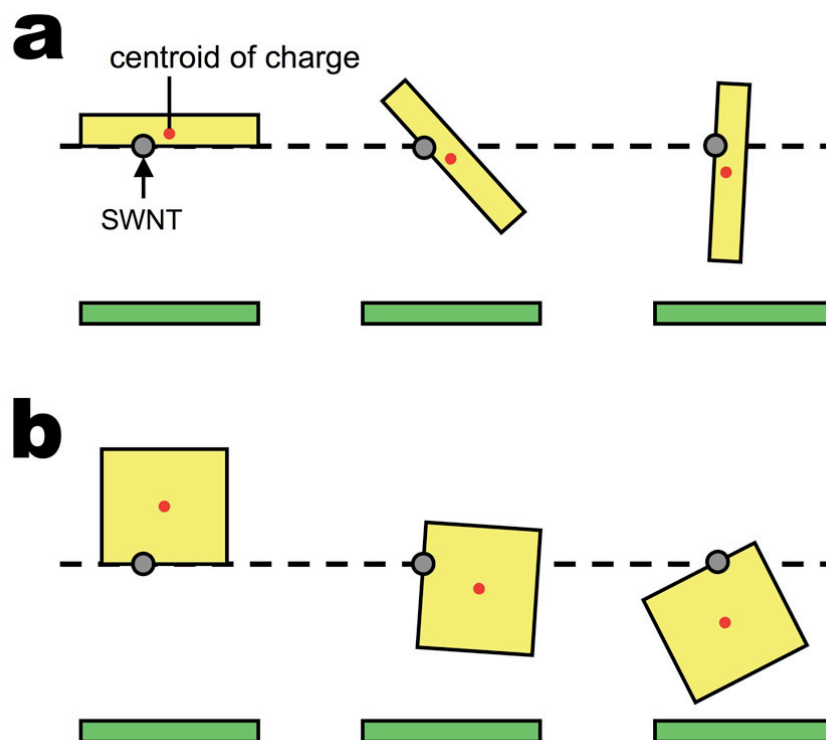


Figure 4.4 Schematics of paddle actuation, where there is an increasing electrostatic force between the substrate (green) and the paddle (yellow) from left to right. Red dots represent the centroid of charge. Thin paddles (a) can only deflect around $\pi/2$ radians while thicker paddles (b) can attain nearly π radians.

The total torsional measurement technique is shown in Fig. 4.5. Generally, SWNT transport was monitored as a DC bias was applied to the backgate electrode beneath. Importantly, these measurements were performed prior to high magnification SEM imaging of the devices. Incident electron beams have been shown to have an adverse (and, in some cases, controllable[60]) effect on CNT structure and transport properties[61]. This was found to diminish or to remove the measurable torsional response. After transport measurements, a series of SEM images were taken of a given device from above over a range of backgate biases, both positive and negative. Analysis of the projected width of the paddle allowed for a measure of its deflection angle at the

given gate value (see eq. 3.2). Because these thicker paddles can achieve large deflection angles, care must be taken to assure the correct widths are being measured from the static images (Fig. 4.6).

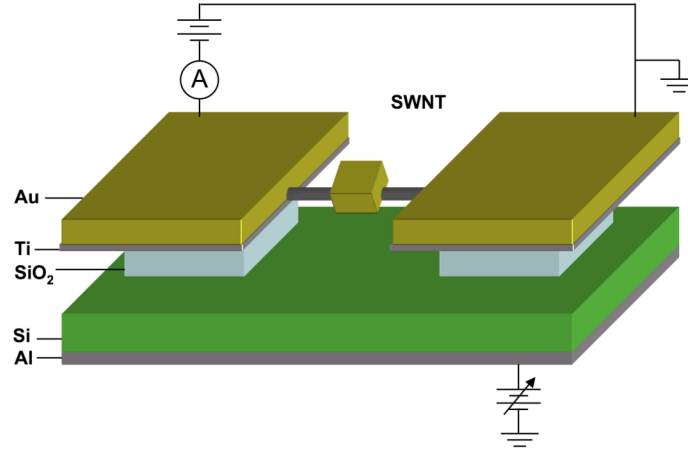


Figure 4.5 Schematic of the self-contained system for the simultaneous measuring of SWNT transport and electrostatic application of torque.

Assuming that the source-drain voltage drops linearly along the length of the tube, we expect that the actual voltage V_{tot} between the paddle and the gate is $V_{BG} - (V_{S-D} \cdot l_1 / (l_1 + l_2))$ and the electrostatic force between the entire paddle and the substrate is then

$$F_{ES} = \frac{\epsilon W_{pad} l_{pad}}{t_{sub}^2} V_{tot}^2 \quad (\text{Eq. 4.4})$$

where t_{sub} is the distance from the paddle to the substrate below (in this case, the original oxide thickness). Because F_{ES} is proportional to torque and thus to paddle deflection, this indicates that $\theta \propto V_{tot}^2$. This will be used in the analysis of the results.

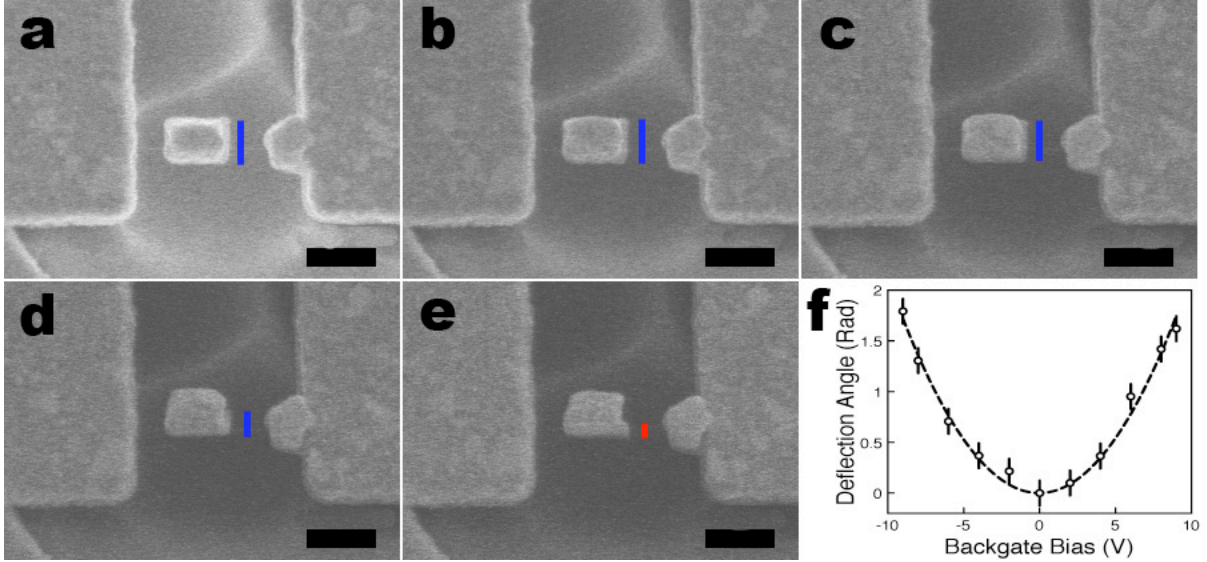


Figure 4.6 (a-e) A thick paddle from 0 to 8 V applied gate bias (each image increases by 2 V). Past π radians, the positive width of the paddle (blue) is measured in negative values (red) along the same surface. Scale bars represent 500 nm. (c) Backgate bias vs. deflection angle for a typical device with a quadratic fit.

Measurement of the resistance response before etching (when the paddle is not free to rotate) allows separation of the torsional response of the SWNT from any field effect (transconductance) in the much longer static sections. This field effect on the etched device would be expected to be even smaller than the dependence prior to etching, as the dielectric constant of the vacuum gap was much lower than the silicon oxide layer (see section 1.4).

The resistance response and measured deflection for two different SWNT devices are displayed in Fig. 4.7. The responses prior to etching are plotted on the same axes. Over many devices, the latter response ranged from slightly *n*-type to slightly *p*-type (Fig. 4.8). This is probably due to a competition between band bending at the metal-nanotube junctions (*n*-type) and the inherent[62] behavior of semiconducting SWNT (*p*-type). In all cases, measured transconductance was small, on the order of $\Delta R \leq 10\%$ (Fig. 4.8).

This can be partially explained by the large oxide thickness (1 μm) and modest applied backgate biases, as discussed in section 1.4. The relatively high contact resistance is another likely cause. Furthermore, no SWNT demonstrated transconductance that was ambisymmetric about 0 V before release.

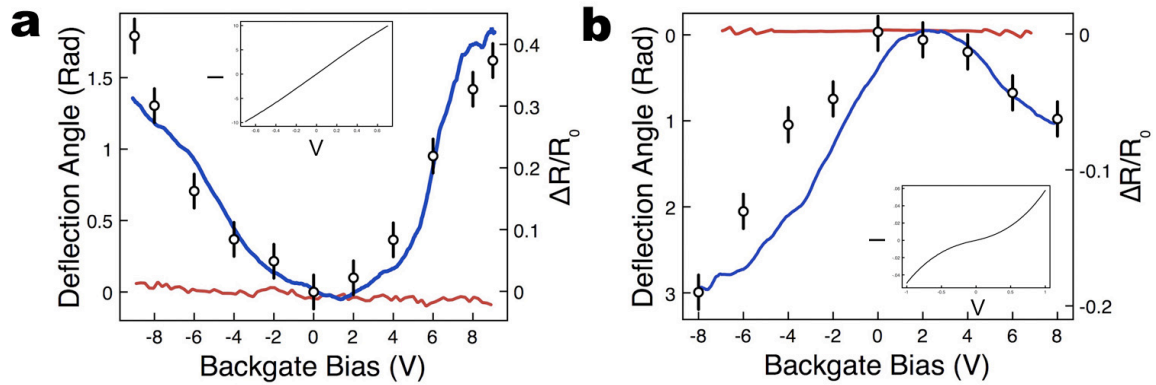


Figure 4.7 Deflection (open circles) and measured differential resistance before (red) and after (blue) etching vs. applied backgate bias for two different SWNT. Both increasing (a) and decreasing (b) resistance was observed for added deflection. Insets: I-V characteristics of each device.

After etching, however, the measured resistance changed with the paddle deflection. The rough symmetry about 0V is consistent with torsional strain as the stimulus for the effect, as the application of either positive or negative bias to the backgate results in a net torque in the same direction and thus the same strain in the SWNT. Importantly, some devices demonstrated an *increase* in source-drain resistance when deflected (Fig. 4.7a) while others demonstrated a *decrease* in the same value (Fig. 4.7b). Measurements were performed in both high- and low-bias source-drain regimes and no qualitative difference was observed. This indicates that optical phonons do not play a significant role in transport for these devices. High bias measurements were

generally performed on the order of $1V_{S-D}$ (Keithley 2400), while the low bias measurements were on the order of 10 mV_{S-D} (EG&G lock-in amplifier).

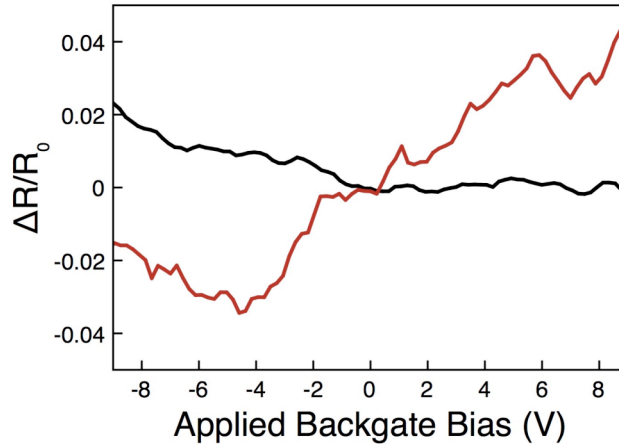


Figure 4.8 Typical gate response of two SWNT demonstrating slight *n*-type (black) and slight *p*-type (red) behavior.

One alternative origin suggested for the measured transport change could be physical alteration of the metal-SWNT contact at either anchor electrode. This could be induced by electrostatic deflection of the tube changing its contact to the metal electrodes. This, however, is an unlikely explanation. Because the nanotube is buried under the deposited metal leads, electrostatic attraction should only be capable of deflecting the tube down toward the substrate and away from the lead. While this could explain an increase in resistance, the observed decrease in resistance for some devices cannot be accounted for. Furthermore, in devices fabricated with longer exposed SWNT on either side of the paddle, no effect was observed. While such devices would still be affected by possible changes to the nanotube contact, the torsional strain applied to the tube for the same paddle deflection would be dramatically reduced.

4.3 Results and Discussion

A second order polynomial is fit to the raw backgate bias vs. deflection data (Fig. 4.6f) in order to get an expression relating the two. This expression is applied to the source-drain transport vs. backgate bias data (Fig. 4.7, blue lines) in order to attain source-drain differential resistance vs. deflection angle. The exposed SWNT lengths in a device- l_1 and l_2 , to the right and left of the paddle, respectively- are then obtained through measuring directly from SEM images. Source-drain differential resistance vs. strain γ in either SWNT section can then be gained through the relation $\gamma=d\ell/2\theta$, where θ is the deflection angle and d is the nanotube diameter. Because direct measurement of tube diameter was difficult and in many cases added contamination to the system, the radius used in this calculation was the mean SWNT radius (0.49 nm) from the AFM-measured distribution of the CVD method (Fig. 2.1). As in Ch. 3, 20% uncertainty accounts for ~95% of all tubes present on the substrate.

A plot of the SWNT torsional strain against measured source-drain resistance reveals that a variety of responses are observed for different tubes. Fig. 4.9 shows the measured response for six different SWNT, plotted against the strain in the shorter exposed length of tube only in order to fit on the same axes. Following past work on strain-induced transport changes, these trends are associated with changes in the nanotube band gap. The insets show the I-V characteristics of two devices. All nanotubes that demonstrated a decrease in measured resistance showed some nonlinearity in this sweep, while those that indicated an increase in resistance varied in their linearity (Fig. 4.10).

This also agrees with the torsional mechanism, as a tube with no initial band gap (ie linear I-V characteristics) cannot experience a decrease in the energetic width of this gap.

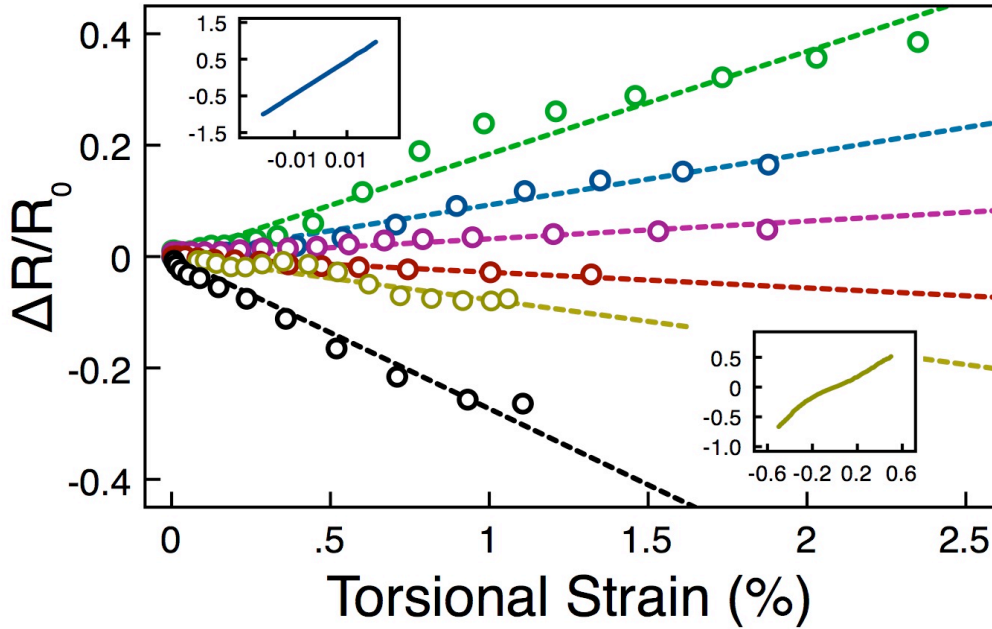


Figure 4.9 Torsional strain (in shorter SWNT section) vs. differential resistance for six different devices demonstrating the side variety of observed reactions. Insets: examples of I-V characteristics for two displayed devices (color indicated).

Further analysis can be performed on data of this kind by referring to the relation between measured SWNT resistance and expected gap energy[37, 56], as discussed in section 4.1. For this system, Eq. 4.1 can be rewritten as

$$\frac{dE_g}{d\gamma} = \text{sgn}(2p+1)3t_o \sin 3\phi(m,n) \quad (\text{Eq. 4.5})$$

It is assumed for this expression that axial strain in the system is negligible. Due to the fact that the Young's modulus (0.97 TPa) is much larger than the shear modulus (~0.45 TPa)[2], this estimation is warranted.

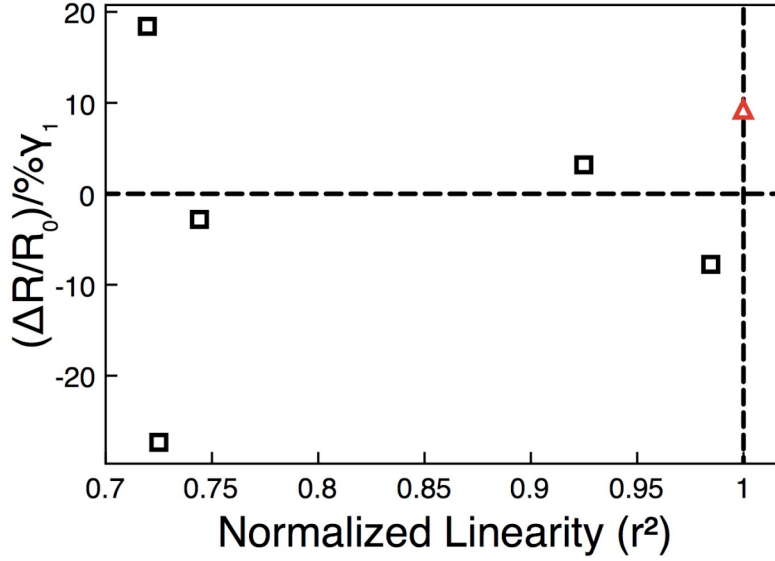


Figure 4.10 For all devices in Fig. 4.7, normalized linearity of the I-V response vs. measured change in differential resistance per unit applied strain. Linearity is measured through the r^2 value- in this case, a statistical measure of how well the I-V data points match to a linear fit, scaled between 0 and 1. A value of 1 is a perfect fit. Linear response (red) implies metallic behavior while nonlinearity (black) implies semiconductor behavior.

The total measured resistance of the system is

$$R_T = R_C + R_{NT1} + R_{NT2} \quad (\text{Eq. 4.6})$$

where R_C is the total contact resistance between the metal leads and the nanotube and R_{NT1} and R_{NT2} are the resistance contributions of each SWNT section. Using this relation along with Eq. 4.2 and 4.4, the measured differential resistance of the device can be correlated with the torsional strains in each section of nanotube through

$$\frac{\Delta R_T(\gamma)}{R_o} = \frac{R_c + R_{NT}(+\gamma_1) + R_{NT}(-\gamma_2)}{R_c + 2R_{NT}(0)} - 1 \quad (\text{Eq. 4.7})$$

Note that the strain on one side of the paddle will tend to compensate the response from the section on the other side. Because Eq. 4.2 does not account for tunneling across the band gap, this equation is most suitable for low source-drain bias measurements, so it is fit to a lock-in measurement (amplitude 50 mV) as shown in Fig. 4.11. In doing so,

further insight is gained into the nanotube structure. The change in resistance due to etching was 10 M Ω , which is attributed to a decrease in contact between the SWNT and the metal leads. The decrease could be caused by a number of factors including changes in mechanical pinning at the anchor lead or oxidation of the contacting metal. But, in general, because the measured resistances of the nanotubes prior to etching are much lower than after (Fig. 4.12), the change is considered to be an estimate of the total contact resistance R_c . The remaining parameters of $|t|^2$, E_o and $\phi(m,n)$ are then to fit the data.

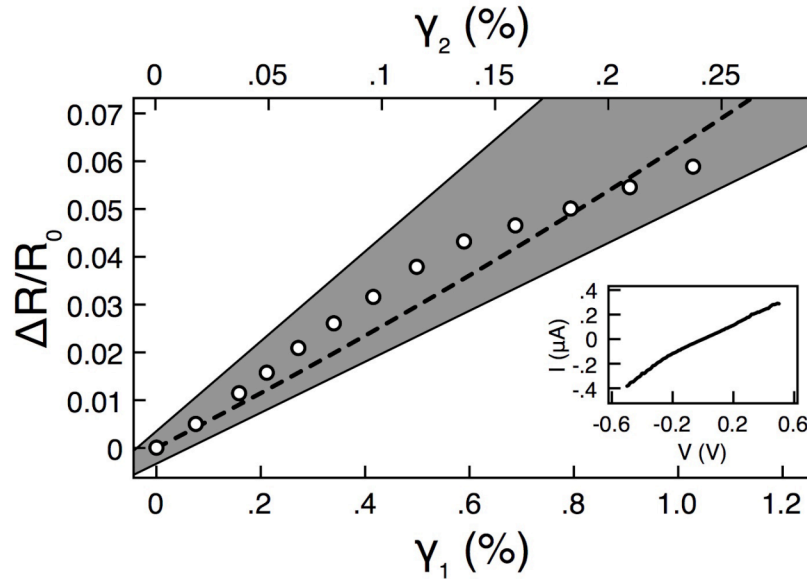


Figure 4.11 Applied torsional strain in each SWNT section (l_1 and l_2 , respectively) vs. measured differential resistance for a common device. Shaded region indicates error in the measured values and dashed line is a fit to Eq. 4.6. Inset: I-V characteristics of the SWNT.

Fitting indicated that the presented SWNT agrees with an initial band gap energy of 29 meV and an estimated chiral angle ϕ of $\sim 57^\circ$. Errors in our measurement- especially in nanotube radius- prevent high accuracy in this value and so these results are not meant to be quantitative. They do, however, demonstrate that the device acts as

expected if the change in measured transport was due to torsional strain. The fit also indicates a transmission probability $|t|^2$ of 0.2, in agreement with other SWNT devices[56, 58]. However, varying this parameter over a large range did not affect the other values significantly, demonstrating its high uncertainty.

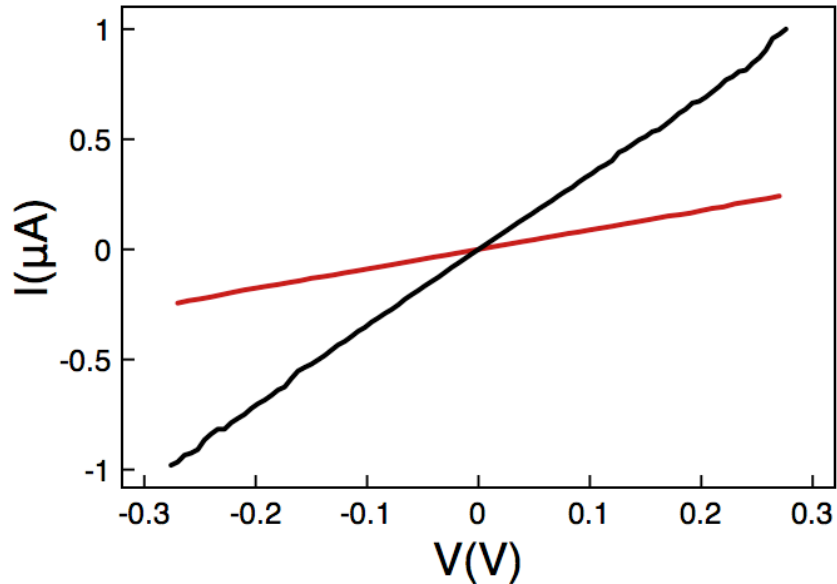


Figure 4.12 I-V characteristics for a typical SWNT taken before (black) and after (red) etching, demonstrating the decrease in measured conductivity due to the process.

This chapter has demonstrated that the torsional nanoelectromechanical device can be utilized as a means to apply a torsional strain to an individual SWNT and that this action can result in a measurable change in the transport properties of that tube. Several factors in the data indicate that the observed responses are in fact a product of the applied torsional strain. First, the gate dependence of the source-drain transport prior to etching was slight and non-ambisymmetric about $V_G=0V$ while after etching, the same measurement followed the torsional deflection of the paddle. Second, the degree of this reaction was found to vary widely between different SWNT, including both direct and

inverse relations. This was in agreement with theoretical expectations of torsional strain. Third, control experiments involving low applied torsional strain (*i.e.* long supporting SWNT lengths) showed no discernible gate dependence outside of field effect. Finally, the transport change was shown to act in a way that agrees with the expected reaction to torsional strain.

Single-wall Carbon Nanotube Torsional Oscillators in Resonance

Machines take me by surprise with great frequency

-Alan Turing

5.1 Introduction

In essence, the CNT-based torsional nanoelectromechanical device is a mass on a doubly-clamped torsional spring. In the previous chapters, this has been employed to study the linear torsional mechanics of individual SWNT (Ch. 3) and to measure the effect of applied torsional strain on the resistance of a SWNT (Ch. 4). In this chapter, these two findings will be combined in order to realize a self-contained method for measuring the resonance of these devices. First, however, it is necessary to discuss oscillatory behavior in general[63], beginning with the simplest harmonic motion of a mass m on a linear spring of spring constant k .

The force on the system when brought out of equilibrium is $m\ddot{x}(t)$ while the linear restoring force for this system is $-kx(t)$. The forces can be set equal, resulting in the equation of motion

$$m\ddot{x}(t) + kx(t) = 0 \quad (\text{Eq. 5.1})$$

The solutions to this relation take the form of

$$x(t) = x_o \cos(\omega_o t + \delta) \quad (\text{Eq. 5.2})$$

where x_o is the initial position of the mass, t is time and δ is the phase of the oscillation.

The variable ω_o is $\sqrt{k/m}$.

Closer to reality is an oscillator that is subject to damping forces. The damping force is assumed to be proportional to the velocity $\dot{x}(t)$, such as in the case of friction. This is not always the case, but it allows for a linear equation of the form

$$\ddot{x}(t) + 2\beta\dot{x}(t) + \omega^2 x(t) = A \cos \omega t \quad (\text{Eq. 5.3})$$

where β is $b/2m$ (b is a constant) and A is F_o/m (F_o is a driving force). This is for the case of sinusoidal driving. The particular solution to this variation of eq. 5.X takes the form of

$$x(t) = \frac{A}{\sqrt{(\omega_o^2 - \omega^2)^2 + 4\omega^2\beta^2}} \cos(\omega t - \delta) \quad (\text{Eq. 5.4})$$

where the factor preceding the $\cos(\omega t - \delta)$ function is the amplitude D of the oscillation and

$$\delta = \tan^{-1} \left(\frac{2\beta\omega}{\omega_o^2 - \omega^2} \right) \quad (\text{Eq. 5.5})$$

The maximum amplitude of the system can be found when $dD/d\omega=0$. The resulting angular frequency ω_R is the resonance frequency and can be expressed as

$$\omega_R = \sqrt{\omega_o^2 - 2\beta^2} \quad (\text{Eq. 5.6})$$

When $\beta^2 > \omega_o^2$, the value of ω_R is imaginary and thus does not exist. Fig. 5.1 shows calculated resonance behavior. The phase angle δ (or the phase between the application of driving signal and its reaction) varies from 0 when $\omega \ll \omega_R$ to π when $\omega \gg \omega_R$, passing through $\pi/2$ at ω_R . The amplitude increases until the resonance frequency and decreases after, producing the familiar peak associated with the phenomenon.

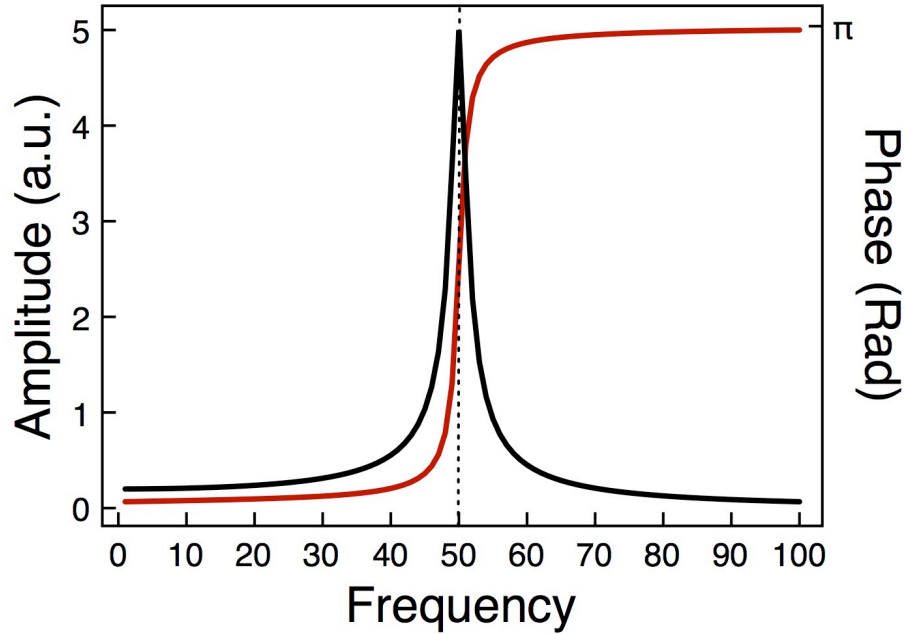


Figure 5.1 Calculated dependence of amplitude (black) and phase (red) on frequency. ω_R set arbitrarily at 50 Hz.

The quality factor, Q , of the oscillator is mathematically defined as

$$Q \equiv \frac{\omega_R}{2\beta} \quad (\text{Eq. 5.7})$$

for $\beta \ll \omega_0$. Because of this relation to the factor β , Q is essentially a measure of the amount of damping in the oscillator- the greater the damping, the lower the Q . Qualitatively, it can be thought of as the number of cycles a given system will keep oscillating after removal of a driving force.

In terms of the resonance peak, the quality factor is a measure of how much larger the amplitude response is at the resonance frequency compared to the off-resonance behavior. It can thus also be defined for measured peaks as

$$Q = \frac{f_R}{\Delta f_{FWHM}} \quad (\text{Eq. 5.8})$$

where f_R is the measured resonance frequency and Δf_{FWHM} is the peak width measured at half the total peak height. This measurement will be used later in this chapter to compare oscillators to one another.

There are, of course, many damping effects that severely diminish the Q of real oscillators. Some of these damping factors have an even larger effect when the dimensions decrease, such as with NEMS devices. Some sources of damping will now be discussed in order to show later how they affect the SWNT torsional system. This treatment will concentrate on external effects as opposed to internal interactions (phonon-phonon, electron-phonon, etc.), as they are dominant for a system on the scale of the SWNT torsional oscillator. One internal dissipation mechanism- the thermoelastic effect- however, is often a major source of loss in NEMS devices[64, 65] and so bears mention. As thermoelastic dissipation is a result of local volume changes in the oscillating structure, pure torsional deflection (such as is assumed for devices detailed later in this chapter) is considered a thermoelectrically lossless mode. A more thorough discussion of both internal and external phenomena can be found in Ref. [61].

The first dissipation mechanism at work is the friction that arises from air resistance on the oscillator as it moves. Despite having very low surface area, interactions of this kind can play a role in damping. At low pressures, the mean free path of gas molecules can be larger than the size of a NEMS oscillator, and so the level of interaction becomes statistical. This effect has been quantified[66] as an energy loss per cycle Q^{-1} through the relation

$$Q^{-1} = \frac{pA}{m_{eff}\omega_o v} \quad (\text{Eq. 5.9})$$

where p is pressure, A is the oscillator surface area, m_{eff} is its effective mass and ω_o is its resonance frequency. The variable v is the thermal velocity of the gas, calculated with

$\sqrt{\frac{k_B T}{m_{air}}}$. At much higher pressures, this dependency changes (Fig. 5.2), but the work in

this thesis deals only with low-pressure measurements.

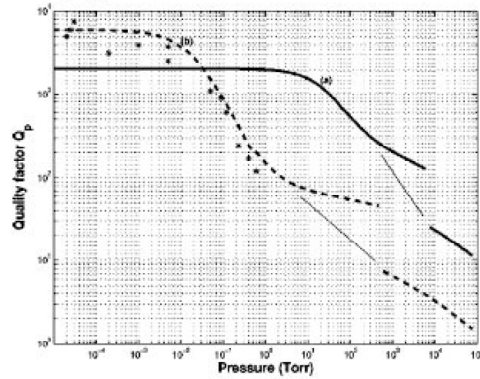


Figure 5.2 Dependence of Q on gas pressure, from reference [66].

A second dissipation mechanism is caused by the clamping of the oscillator at its interface with the mechanical supports. Here, acoustic energy can be lost in each cycle. Calculations involving this kind of dissipation have been limited to cantilever based systems. This is because multiple experimental data[67, 68] have concluded that clamping loss in torsional elements is negligible. While these findings were for micromechanical rather than nanomechanical resonators, it can be inferred that dissipation is similarly low in that regime.

For an estimate, however, the most relevant cantilever relation is the general case of a finite thickness, which can be expressed as[69]

$$Q^{-1} \approx \frac{w}{L} \left(\frac{t}{L} \right)^4 \quad (\text{Eq. 5.10})$$

where w , t and l are width, thickness and length of the cantilever, respectively. Other calculations for clamping loss[70] make assumptions about the oscillator geometry (infinite width and equivalent thickness of the cantilever and the support, respectively) that make them less applicable to the oscillators being studied here.

A final relevant loss source is ohmic dissipation resulting from capacitive coupling in a system being measured electrically. This source has been quantified for a similar system[61] as

$$Q^{-1} = \frac{(C'V)^2}{\pi k C} \left(\frac{\omega \tau}{1 + (\omega \tau)^2} \right) \quad (\text{Eq. 5.11})$$

where C is capacitance (C' being its spatial derivative), k is the resonator spring constant, ω is frequency and τ is the time constant RC .

Each of these mechanisms will be estimated for measurements on SWNT torsional devices later in this chapter.

5.2 Resonator Detection Schemes

High-quality oscillators have found wide use in a variety of technologies, ranging from timing elements to sensors. The miniaturization of such devices can have several advantages, such as lowering power requirements, increasing sensitivity and introducing additional quantum effects that may enhance utility. Towards this end, conventional silicon processing technology has been pushed to its limit in recent years, resulting in truly nanoscale devices with sharp oscillatory behavior[71].

As the critical dimension of these systems decrease, the means by which they can be monitored becomes an issue. Optical techniques have been a traditional approach to resonance measurement. Commonly in this method, laser light is reflected off both the resonator (measurement beam) and a stationary surface, such as the underlying substrate (reference beam). As the resonator moves, the measurement beam changes with respect to the reference, interfering constructively and destructively to varying degrees. By sensitively monitoring the sum of the two beams (hence the name ‘interferometry’), a measure of the instantaneous displacement of the device is made. When the resonance frequency is met, average displacement increases resulting in a peak in the measured beam intensity.

This is the method used in the detection of MWNT torsional device resonance[40] (see section 4.1). The measurement apparatus (Fig. 3.3a) utilizes only a single beam for both measurement and reference, as the spot size is large enough to be incident on both the resonator and the underlying substrate. This method is applicable because devices built on MWNT can be fabricated with relatively large paddle dimensions ($\sim 1 \mu\text{m}$). Those built on SWNT must be made somewhat smaller because the lower shear modulus results in larger amplitude thermal and mechanical vibrations. Paddles of larger dimensions can easily contact the underlying substrate, rendering them useless. As the size of the oscillator decreases to dimensions near that of the incident light wavelength, however, the method becomes less viable due to signal-to-noise limitations. As such, alternative measurement schemes must be used for devices at smallest, most interesting scales and many have been successfully demonstrated.

The most intuitive of these is the direct observation of the oscillator amplitude by an imaging technique, such as electron microscopy[67]. In this case, device actuation is performed *in situ* (for example, electrostatically with a counter-electrode) and when resonance is met, the amplitude of oscillation is observed directly, often as a blurring of the moving part. While powerful in its simplicity, this measurement has several drawbacks. First, it can be dependent on the frame rate of the observation; in some cases, excitation may simply happen too quickly to be detected. Secondly, it is poorly understood how much the imaging beam itself affects the operation of the device. This is especially true as the scale decreases and other effects such as charging play a larger role. Finally, environmental parameters such as pressure and adsorbed gas cannot be varied as most nanoscale imaging techniques (SEM, TEM) have strict operating requirements.

As such, many other more quantitative methods have also been used. Measuring the capacitance between a plate and a stationary component, for example, has been widely used in MEMS technology, especially with the aid of a multi-prong comb structure to increase the effect[72] (Fig. 5.3). Because the capacitance C is inversely related to plate separation d or overlapping area A through $C=\epsilon A/d$, the measurement is a sensitive determination of relative motion. Though challenging, the technique has been utilized for measuring nanometer-scale devices as well[73]. A variation on this theme in which an oscillator is coupled to a superconducting single electron transistor has also been demonstrated, reaching extremely high resolution in the measurement[74].

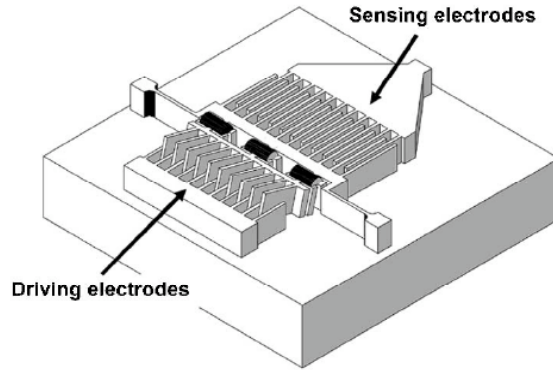


Figure 5.3 Schematic illustration of capacitive displacement sensing in MEMS technology[72]

Another quantitative measurement technique involves the use of electromotive force (EMF)[75]. Here, a doubly clamped beam (oscillator) is also used as a current carrying wire. A magnetic field is placed perpendicular to the beam orientation and a small AC current is introduced through the suspended beam structure. This causes a transverse Lorentzian force on the structure, which results in the oscillatory behavior of the device (Fig. 5.4). Beam actuation, in turn, induces an EMF that can be monitored electrically. This signal is maximized with maximum device amplitude.

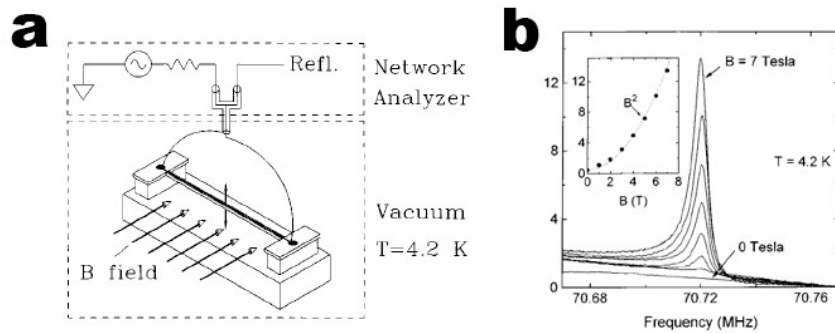


Figure 5.4 (a) Experimental method for measuring oscillation of amplitude with EMF and (b) and example of observed resonance peaks (EMF on y axis)[75].

Intrinsic properties of the oscillator material can also be exploited for detection. For instance, the field emission properties have been used in measuring resonance in an individual cantilevered nanotube[76]. Here, a nearby anode was used to apply electrostatic forces to a strongly biased MWNT while an electron-sensitive screen (at ground relative to the MWNT) was used to monitor field emission (Fig. 5.5a). The emitted current is very strongly correlated to the tube-screen distance d through the Fowler-Nordheim equation[77]:

$$I = V^2 a \exp\left(\frac{-b\varphi^{\frac{3}{2}}d}{\beta V}\right) \quad (\text{Eq. 5.12})$$

where V is the applied voltage, β is the field enhancement factor, φ is the tube work function and a and b are constants. Hence, the total emission current measured at the screen as the actuation frequency is swept reflects the oscillator amplitude (Fig. 5.5b).

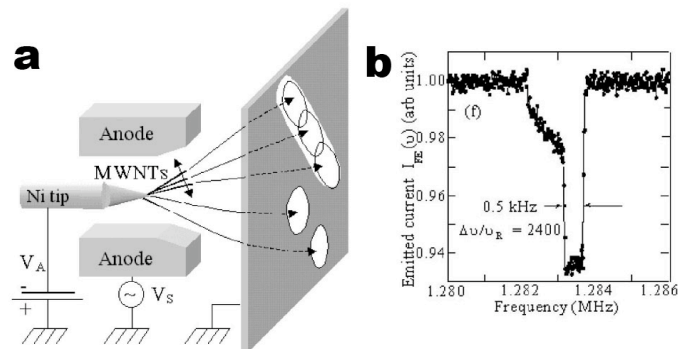


Figure 5.5 (a) Experimental setup for measuring MWNT resonance via field emission and (b) a resulting resonance peak measured through total emitted current at the electron sensitive screen[76].

A second example that uses material properties is the measurable response of a piezoelectric material. Here, material deformation during oscillation is transduced to an electrical response by intrinsic properties of the device material. This is strongly tied to the methods discussed for devices later in this chapter. Though incorporated widely in MEMS technology[78, 79], the generally high resistance of NEMS results in frequency dependent attenuation in the MHz range. This has been overcome successfully by using a down-mixing method to convert the high resistance pathway to $50\ \Omega$ through the use of electronics before the signal reaches the device[80] (Fig. 5.6). Piezoelectric response also offers the advantage of an entirely integrated detection mechanism that is not dependent environmental conditions or external fields.

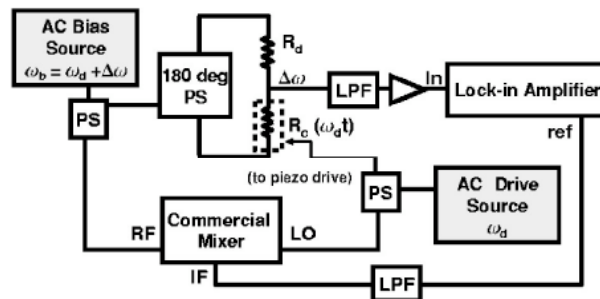


Figure 5.6 Circuit diagram for the down-mixing technique used to measure resonance piezoresistively[80].

A final example of an actuation/detection system is the pioneering work performed by Sazonova, *et al* on doubly-clamped SWNT[61]. Here, they utilized the property of semiconducting SWNT that the charge on the tube body is directly correlated with its conductance. A suspended SWNT was actuated through a small AC signal (offset

from zero) applied to the backgate electrode. The relation for change in charge, δq , is as follows:

$$\delta q = \delta(CV) = C\delta V + V\delta C \quad (\text{Eq. 5.13})$$

where C is capacitance and V is voltage (gate). The first term $C\delta V$ occurred throughout the measurement because the actuation signal is alternating. The second term $V\delta C$, however, only occurred in the system when there is a change in the distance between the tube and the gate; this is the case for the increase in oscillation amplitude then resonance is met. The SWNT was used as a mixer in order to monitor the small change in source-drain conductance that the capacitance effect caused, revealing resonance that could be tuned by changing the DC offset of the actuation signal (Fig. 5.7).

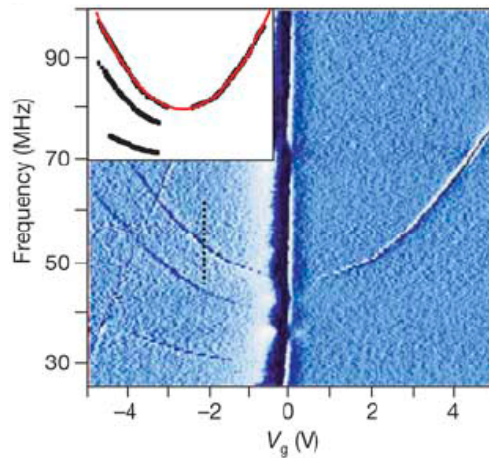


Figure 5.7 Experimentally measured SWNT resonances (vertical slices are frequency sweeps) and their dependence on gate offset V_g , demonstrating device tunability[25].

In the previous chapter, the torsional strain transduction properties of SWNT were demonstrated. These could also be used as a means to directly measure resonant behavior

(Ch. 4). This chapter will concentrate on detection of torsional device oscillation in this manner.

5.3 Experimental Methods

Devices are fabricated as described previously (section 2.3) with thick paddles to allow for large deflection angles. For each sample, the transport properties and their reactions to applied torsional strain are characterized in the manner discussed in detail in Ch. 4. This allows for the determination of consistency throughout all subsequent measurements.

Measurements of resonant behavior are performed in the vacuum of the SEM chamber ($\sim 10^{-5}$ Torr). Source-drain current is monitored with a low bias (50 mV) lock-in apparatus while a frequency-swept actuation signal is applied to the backgate electrode. This is accomplished through the use of a small (on the order of 100 mV) alternating signal, offset from zero (typically by 2-5V). The offset applies an initial deflection to the device, which has a twofold effect. First, it brings the centroid of the paddle close to the gate electrode, thereby increasing the electrostatic force resulting from the AC bias as the force has an inverse relation to the square of the separation distance (eq. 4.4). Second, it allows a symmetric reaction to the alternating signal; if it were to start from zero offset, the positive and negative portions of that signal would both cause attractive forces, doubling the effective frequency (Fig. 5.8). Offset voltages were used in other oscillator investigations[25, 40] for the same purpose.

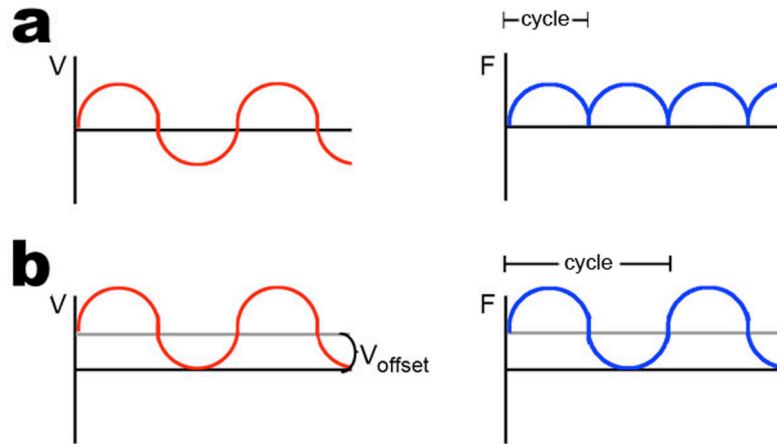


Figure 5.8 Effect of DC offset on alternating actuation. With zero offset (a), the applied frequency of the actuating signal V is doubled because both positive and negative biases result in attractive forces. With offset voltage V_{offset} equal to or greater than half the actuation amplitude, the applied frequency is maintained in the force spectrum.

As the actuation signal approaches the resonance frequency ω_o , the amplitude of device oscillation increases as well such that the paddle is at a higher average deflection angle during that portion of the sweep. This translates to a measurable peak in the source-drain resistance that is highly localized in the frequency spectrum. Fig. 5.9 shows an example of such a measurement that includes elucidation of the primary resonance peak as well as the first harmonic. Both peaks are high above the noise floor, have the same qualitative shape (Fig. 5.9 insets) and the harmonic occurs at $\sim 2.1\omega_o$. These three facts support the measurement as a mechanical resonance rather than an anomalous electrical peak, etc. There is $\sim 8\%$ error in the absolute frequency due to the measurement technique. Improving this measurement is of prime importance to future studies.

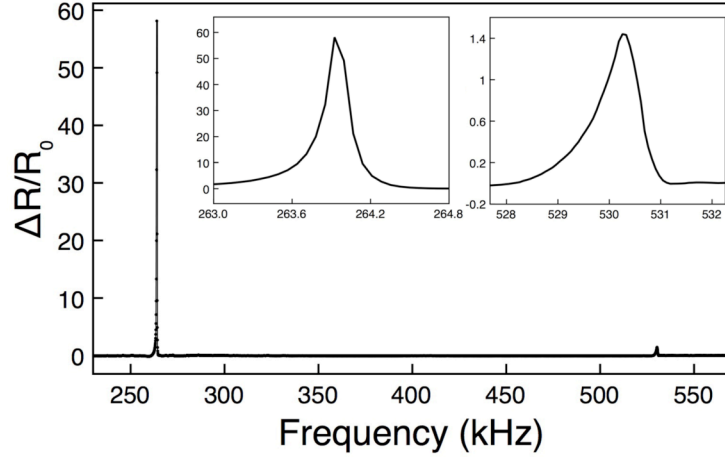


Figure 5.9 Measured change in SWNT differential resistance during a sweep of actuation frequency, showing both a resonance peak (~264 kHz) and the first harmonic (~530 kHz). Insets are magnified views of the primary peak (left) and the first harmonic (right), demonstrating their similar shapes.

The position of the main resonance peak offers a way to confirm the nature of the oscillation. A relation for the expected resonant frequency of the torsional mode has been shown[42]:

$$\omega_{\text{torsional}} = \frac{1}{2\pi} \sqrt{\frac{\kappa}{I}} \quad (\text{Eq. 5.14})$$

where κ is the torsional spring constant and I is the oscillator moment of inertia. Values for each of these can be inferred from measurements of the device images (see Fig. 3.4) and theoretical values for SWNT material properties. Upon doing so for the particular SWNT torsional oscillator measured for Fig. 5.9, the relation yields a value of $\omega_o = 358 \pm 125$ kHz. The large error stems from the value for κ , which is proportional to r_{swnt}^3 . Nonetheless, the measured resonance peak occurs well within this range.

Importantly, the resonance measurements also agree with the quasistatic electromechanical response in sign. As discussed in section 4.3, the same applied

torsional strain can affect the source-drain transport characteristics of different types of tubes in a range of ways- a twist can increase the resistance of some while decreasing the resistance of others, dependent on lattice orientation. Therefore, when utilizing the strain response to monitor device resonance, it is expected that the direction of the observed resonance peak could be either positive *or* negative in source-drain resistance, depending on the SWNT on which the particular device is built. Both reactions are observed and each agrees with the DC measurements taken before frequency-dependent actuation (Fig. 5.10). This is further confirmation that the measured transport response is a direct result of torsional strain and not some other response.

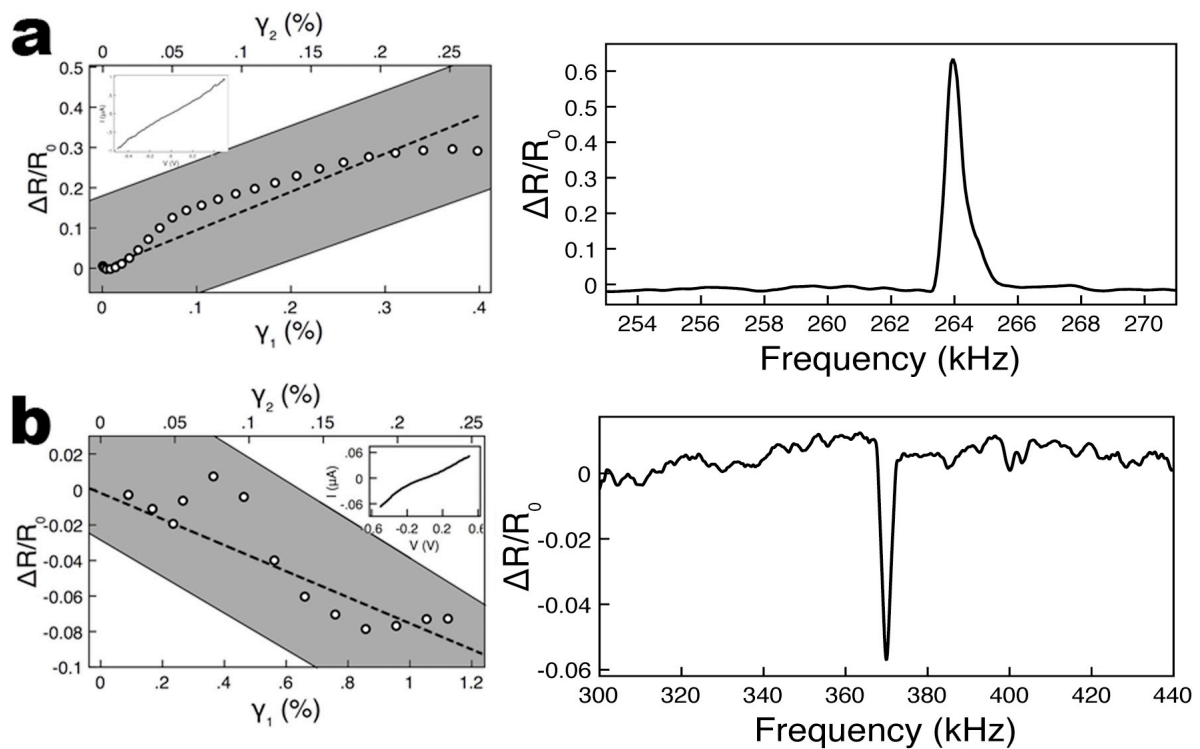


Figure 5.10 SWNT transport-strain dependence and measured resonance behavior for a two different nanotubes, one demonstrating (a) a direct relation and (b) an inverse relation between source-drain resistance and applied torsional strain (see section 4.3 for details). The direction of the peaks agrees with the respective DC deflection relation. Insets in differential resistance vs. strain plots are I-V behavior.

In order to verify the nature of the source-drain peak, however, an alternative method of measuring the mechanical resonance must be used. Optical interferometry is challenging for these devices because the surface area of the oscillating paddle is much smaller than that of previously measured MWNT devices- roughly 1/3 the size- critically decreasing the resolution of the technique (see previous section). Therefore, *in situ* imaging of the driven oscillator is used as a secondary measurement technique.

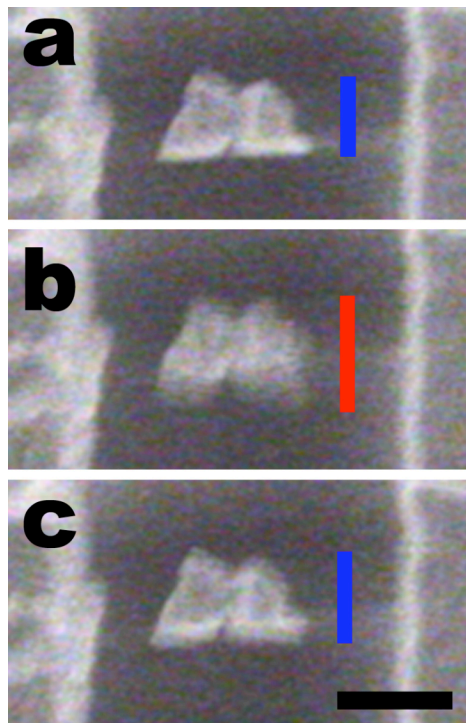


Figure 5.11 SEM images of a paddle (initial gate bias of 2 V_{DC}) with applied actuation frequency of (a) 245, (b) 257, (c) 276 kHz. The apparent width of the oscillator is larger on resonance (red bar in b) than off resonance (blue bars in a and b). Scale bar represents 500 nm.

For direct observation of resonance, the device is driven as stated above, but while simultaneously imaging it with the SEM. Importantly, this is performed after all

transport measurements on the device, as the incident electron beam was detrimental to the source-drain signal (see section 4.2). Similar to previously mentioned experiments[5, 7], when resonance is met, the increase in oscillation manifests itself as a blurring of the suspended platform (Fig. 5.11). The apparent width of the paddle over a range of actuation frequencies is then used as a direct measurement of the amplitude of oscillation. When plotted on the same axes as the source-drain electrical signal, it is found that the peaks are coincident in the frequency spectrum within uncertainty mentioned above (Fig. 5.12).

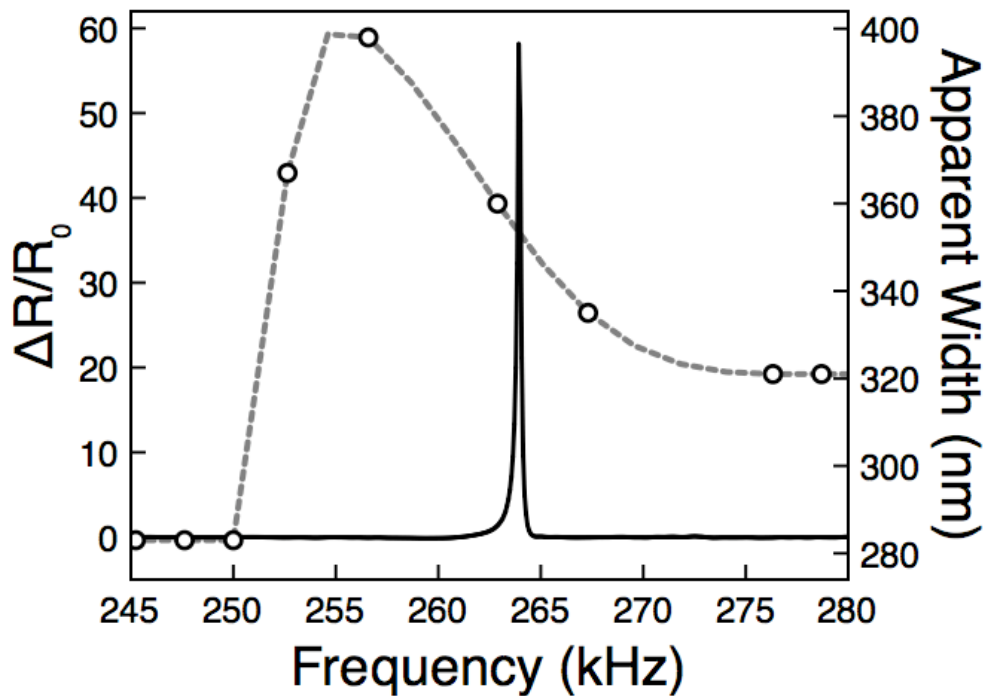


Figure 5.12 Comparison of resonance measured by the SWNT electromechanical effect (solid line) to that observed by direct imaging (open circles). The latter is measured as the apparent width of the paddle structure as it blurs due to oscillation amplitude (see Fig. 5.11).

The amplitude measurement from the SEM images is very wide compared to the electrical signal. This may be due to effects caused by the imaging beam, such as charging, amorphous carbon contamination or beam-induced damage to the carbon lattice, each of which could contribute to additional damping. These sources could also account for the somewhat lower resonance frequency observed with the imaging method, although uncertainty makes it difficult to know whether the difference is even real.

In the next section, the observed resonant response of the SWNT torsional device will be analyzed further.

5.4 Oscillator Behavior of a SWNT Torsional Device

The resonant behavior of a SWNT torsional device is further studied by varying the amplitude of the alternating signal being applied to the gate electrode. As expected for a driven oscillator, the amplitude of the resonant oscillation (as related by the height of the resonance peak) is strongly dependent upon the amplitude of the driving signal. Fig. 5.13 shows the resulting peaks for drive amplitudes of 0.1, 0.3, 0.5 and 0.6 V (gate offset is $2 V_{DC}$). An asymmetric peak can be observed at a slightly larger applied amplitude of 0.7 V (Fig. 5.13 inset). This section will characterize the measured amplitude-dependent response of a SWNT device.

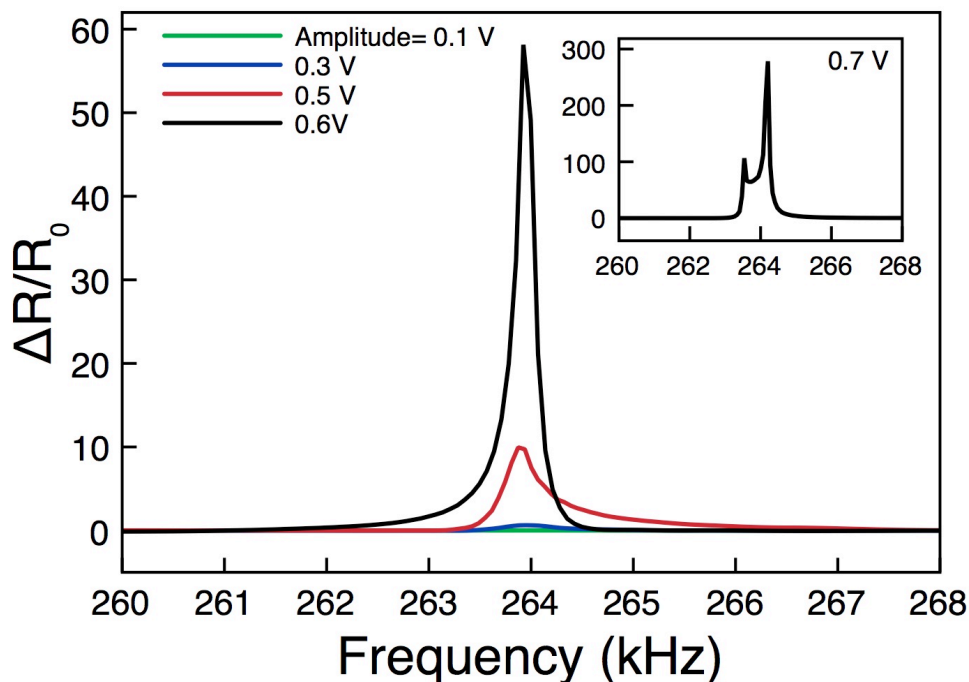


Figure 5.13 Measured resonant behavior of a SWNT device at actuation amplitudes of 0.1, 0.3, 0.5 and 0.6 V. Inset: response to a 0.7 V actuation amplitude, showing peak asymmetry (see text).

It is clear from the figure that one side of the peaks is steeper than the other. This detail is an artifact of the measurement technique, wherein the frequency change of the applied signal is varied slightly faster than the source-drain data acquisition rate. Therefore, as frequency is swept, the leading edge of the peak rises quickly while the trailing edge falls slowly. It is especially noticeable between the 0.6 V peak (frequency swept from high to low) and the 0.5 V peak (frequency swept from low to high) in Fig. 5.13.

The height of a resonance peak is directly correlated with the maximum amplitude of device oscillation (see section 5.1). Because the deflection amplitude is directly related to the strain in the SWNT, a plot of the square of the drive signal amplitude against the maximum differential resistance is also essentially a representation of strain vs. resistance

(due to $\gamma \propto V^2$, following eq. 4.4). Interestingly, as Fig. 5.14 indicates, there is an exponential relation between these two factors. This is in qualitative agreement with many previous uniaxial SWNT piezoresistant measurements[56-58] (see eq. 4.3) and can therefore be viewed as further evidence of the torsional strain effect discussed in Ch. 4. Moreover, though, the exponential relation indicates that the SWNT torsional devices can be operated with high sensitivity using this measurement technique.

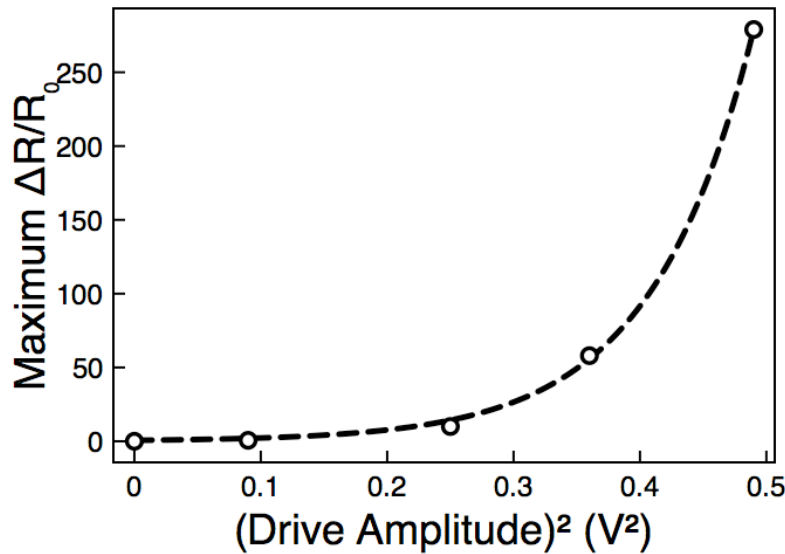


Figure 5.14 Square of the actuation amplitude vs. maximum height of measured resonance peaks, indicating an exponential dependence.

The specific reaction of the peak to the highest gate amplitude (0.7 V) is also of interest. It is possible that the observed response in this regime is a result of an inherent property of the SWNT. As the amplitude of oscillation approaches its largest value (at ω_0), it may begin to induce enough strain on the SWNT to cause the band gap to begin to close again, as predicted in theory[50] (Fig. 5.15). This would result in a measured decrease in the differential resistance after the initial increase of the peak. It is unlikely

that the feature is a result of tube buckling, as eq. 3.8 makes clear, but the linearity of the oscillation at large amplitude is not well characterized.

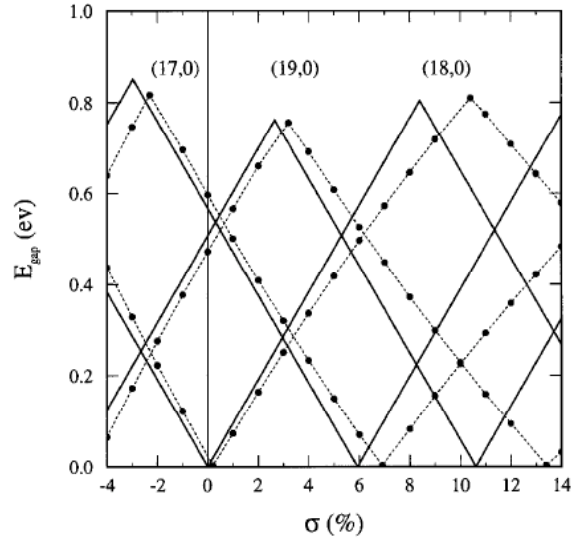


Figure 5.15 Theoretical relation of strain to band gap for three chiralities of SWNT, showing oscillatory behavior in the expected reaction[50].

The quality factor Q for the three symmetric and measurable peaks varied somewhat- 1150 for an applied amplitude of 0.6 V, 620 for 0.5 V and 430 for 0.3V. This may be a result of the aforementioned exponential relation between device amplitude and the source-drain transport that is used as a measurement technique. This will have the effect of stretching a peak in the y -axis, essentially increasing the effective Q artificially. While this feature may be useful in the application of the device, it could exaggerate the true mechanical Q of the oscillator.

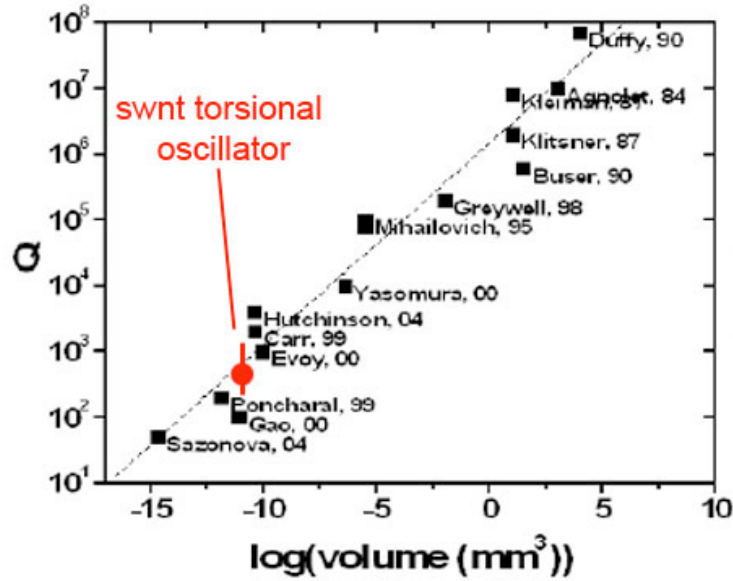


Figure 5.16 Relation of current SWNT torsional device quality (average and range) to various other oscillators, showing good agreement with the expected trend. Adapted from Ref. [61].

An average value of the three measurable peaks is considered representative of the true device characteristics. Here, $Q=740$, which fits well with the general trend of oscillators based on volume (Fig. 5.16). It is also clear from this value that the external dissipation mechanisms discussed earlier in this chapter are not the major sources for energetic loss in the system. By applying values specific to the SWNT torsional device to each dissipation calculation, it is found that the associated losses are not large enough to overdamp the oscillator (Table 5.1).

Mechanism	Q ⁻¹ Equation	Q
Air friction	$\frac{p(2l_{pad}w_{pad} + 2l_{pad}t_{pad} + 2w_{pad}t_{pad})}{m_{eff}\omega_o\sqrt{3k_B T/m_{air}}}$	3 x 10 ¹⁸
Clamping	$\left(\frac{t}{L}\right)^5$	10 ¹²
Ohmic	$\frac{(C'V)^2}{\pi\kappa C} \left(\frac{\omega_o\tau}{1 + (\omega_o\tau)^2} \right)$	10 ¹²
Thermoelastic effect	$\frac{\alpha^2 TE}{c} \left(\frac{\omega_o\tau}{1 + (\omega_o\tau)^2} \right)$	0 for pure torsion

Table 5.1 Calculated oscillator dissipation losses, adapted from [61] for the SWNT torsional device

5.5 Results and Discussion

In this chapter, it has been shown that the SWNT paddle device can be operated as a resonant torsional oscillator. Furthermore, this oscillatory behavior can be measured directly through the transduction properties that were detailed in Ch. 4, allowing for the assessment of resonant actuation with simple source-drain transport monitoring. Examination of observed resonance peaks yielded both further confirmation of the SWNT electromechanical response to strain and information about the device as an oscillator.

The fact that resonance can be monitored in this way at all is corroborating evidence of torsional piezoresistivity. The oscillatory behavior itself was confirmed by

observing a higher order harmonic of the resonance (Fig. 5.9) as well as by measuring the frequency response through a secondary method of direct imaging (Figs. 5.11 and 5.12). Furthermore, the actuation amplitude dependence (Fig. 5.14) showed qualitatively that the transport response to torsional strain (much higher strains than can be applied through DC actuation, such as in Ch. 4) has an exponential dependence. This is in agreement with past results[56-58].

As an oscillator, the SWNT-based device exhibits a Q nearing 1000 and falling in line with the trend of past devices (Fig. 5.16). Calculations indicate that there is relatively little loss in the system (Table 5.1).

Summary and Future Directions

The Future is here. It's just not widely distributed yet.

-William Gibson

6.1 Research Summary and Implications

This thesis has presented experimental measurements on a number of a SWNT torsional nanoelectromechanical device, which utilizes an individual SWNT to support a small paddle above a substrate and between two anchoring electrodes. The device allows the nanotube to be used as a torsional spring.

The mechanical reaction of such a device to applied electrostatic forces were deduced and through careful calculations to estimate the actual amount of torque acting on it, the first direct measurement of SWNT shear modulus was performed (Ch. 3). This line of experimentation demonstrated general agreement with theoretical calculations of the modulus and showed that the material acts as a linear torsional spring within the limits of strain applied through electrostatics. These results will be of importance to the incorporation of nanotubes into nanomechanical devices and may be expanded upon to have application in CNT-polymer composites. Furthermore, the measurement technique can be generalized to measure the torsional mechanical properties of a wide range of other nanometer-scale materials with applications in a wide range of areas.

Next, the device was used to examine the effect of applied strain on the transport properties of individual SWNT (Ch.4), as both theory[45-50] and experiment[54-58] have demonstrated. By monitoring source-drain resistance during the application of torque, a range of reactions was observed. This was in agreement with expectations and represented the first measurement of the torsional electromechanical response in a SWNT. The results of these experiments could have a wide range of application, from variable resistors in NEMS devices to characterization of the lattice structure of individual SWNT.

Finally, the torsional device was operated as an oscillator (Ch. 5). By incorporating the strain sensitivity of the source-drain transport, it was shown that the system can operate as a self-sensing nanoscale resonator with a Q in the hundreds. The behavior was confirmed through a secondary measurement of the resonance and the amplitude-dependent response was examined. These results could have a great deal of use as a highly sensitive resonator and to all the applications that that entails.

6.2 Future Directions and Aims

The CNT torsional device geometry has proven to be an intriguing one, as demonstrated by the number of investigations[14, 32, 40, 41, 59, 81] that have been performed since its inception. As the experiments detailed in this thesis imply, however, there is still a large amount of knowledge to be gained from future work involving them. In this final section, some of these aims will be discussed.

SWNT-based systems offer great promise in a variety of fields. First, improvements can be made to future generations of the devices (such as decreased

contact resistance to the tube and higher strain capabilities) that could allow for lower uncertainty in the measurements and better characterization of nanotube properties. Several analysis methods offer the ability to measure the fine structure of a particular SWNT either before or during application of torsional strain. These could include Raman spectroscopy[82], electron diffraction[83] or fluorescence microscopy[30]. Four-probe measurements could offer more confident elucidation of the changes in the inherent SWNT properties caused by torsional strain and recent advances[84] could allow for the fabrication and study of many devices built on tubes of a single chirality. Applications for well characterized devices of this kind could include electrical switching and varister components in NEMS.

As a resonant oscillator, the SWNT torsional device offers a number of possibilities, especially due to its self-sensing characteristics. Among the most exciting could be its utility in the field of biological and chemical sensing. The paddle itself can be functionalized through thiol chemistry to be reactive with a large range of entities, which could lead to direct mass sensing through frequency shifting in the resonance peak. While challenges exist (such as the sensitivity of the SWNT itself to adsorbed molecules), the possibilities are enticing.

The present body of work on the CNT torsional nanoelectromechanical system should be viewed as a beginning to a large set of investigations. This is a versatile platform for the study of CNT and nanomaterials in general.

APPENDIX 1: CHEMICAL VAPOR DEPOSITION TECHNIQUE

The following section includes step-by-step instructions for performing CVD growth of SWNT for device fabrication. All flow rates and growth times have shown to be highly dependent on the specific apparatus being used; different systems may require significant variation in the values presented here.

- 1) Cleave silicon into small pieces
 - Limited by the inner diameter of the tube furnace
- 2) Solvent clean and UV/Plasma clean substrates
- 3) Using Fe/Mo nanoparticle catalyst solution in hexane (dilute to 1/100k), deposit solution over entire surface and let evaporate
 - If using other catalyst or different initial concentration, may need to test several dilutions to find ideal amount
- 4) Place sample(s) into tube furnace
- 5) With no gas (air), anneal sample at 700 C for 10 min. (take into account ~5 min heating time)
- 6) Allow to cool to below 200 C
- 7) Hook up gas inlet and exhaust; turn on gas tanks at regulators
- 8) One at a time, set flow rate of Hydrogen (400 sccm), Methane (800 sccm), and Ethylene (5 sccm), and turn off each at switch
- 9) Turn on Hydrogen and purge for 15 minutes to remove air (dangerous)
- 10) Keep Hydrogen on and turn temp to 900 C (10 min)
- 11) Turn on both Methane and Ethylene (5 min) for growth

- Ensure flow rates at the beginning of the growth process
- 12) After growth, turn off Methane and Ethylene; leave Hydrogen on and let flow
- 13) Reduce temp and wait until < 200 C to shut off Hydrogen and remove samples

APPENDIX 2: CARBON NANOTUBE TORSIONAL DEVICE

FABRICATION DETAILS

Following is the complete fabrication method for CNT-based torsional devices from bare wafer to suspended structure. The instructions are very specifically written for the following equipment:

- Hitachi S-4700 FE Scanning Electron Microscope
- Kasper UV mask aligner
- Keithley 2400 sourcemeter
- Nano Pattern Generation System (NPGS) Software (J. C. Nability)
- DesignCAD
- Balzers Union CPD 020 critical point drying apparatus

The details will vary with different systems, but the general order of steps can be maintained to result in working devices.

****NOTE: if using CVD nanotube material, prepare nanotubes prior to all other processing by following Appendix 1****

I. Photolithography

1. Clean wafer

- rinse with solvents and Nitrogen dry

2. Clean room prep

- turn on gas (house or tank) and vac pump
- suit up, get 1813 resist from refrigerator, turn off light and enter yellow room (step on sticky mat on the way in)
- press POWER and then LAMP START on lamp power box (you'll hear squealing for a while) and power up mask aligner
- turn on individual Nitrogen flow
- set lamp to IDLE

WHILE LAMP HEATS UP:

3. Apply resist

- set spin coater to 4000 rpm and 60 seconds, set hotplate to 115 C and set a timer to 1 min
- place all samples onto hotplate for 5-10 min. covered with watch glass or beaker to drive off water vapor
- line inside of spin coater tray with aluminum foil for clean up
- remove one sample from heat and stick, unpolished side down, to spin coater chuck (with vacuum function or two sided tape) and fill 10 mL beaker with resist
- blow off sample with Nitrogen gun and pour on resist until entire surface is covered but not dripping off edges, start spinning and (once finished) move to hotplate and start the timer- remove after 1 min
- repeat for all samples

4. Exposure

GENERAL OPERATION:

- press MASK LOAD
- lift metal holder and load mask
- load sample
- ensuring mask doesn't fall before vacuum takes hold, lower metal holder
- press LOADED MANUAL (SEP light comes on)
- visually align sample
- press CONT
- set timer and press MANUAL EXPOSE

BEFORE WAFER EXPOSURE:

- prepare photometer (on bottom shelves under lamp power box)
- put meter probe on exposure platform and switch timer on lamp to arbitrarily high number
- load normally, except without a mask and expose
- use photometer output to calculate exposure time based on "high resolution process parameters" (below)

High Resolution Process Parameters (Refer to Figure 1)	
Substrate:	Polysilicon
Photoresist:	MICROPOSIT [®] S1813 [®] PHOTO RESIST
Coat:	12,300Å
Softbake:	115°C/60 sec. Hotplate
Exposure:	Nikon 1505 G6E, G-Line (0.54 NA), 150 mJ/cm ²
Develop:	MICROPOSIT [®] MF [®] -321 DEVELOPER 15 + 50 sec. Double Spray Puddle (DSP) @ 21°C

from Microposit user manual

- you can also check log for previous successful exposure times and use that

- you may want to test parameters on a spare sample before exposing all wafers

CHECK:

- mask chrome (darker) side down?
- if zif pattern, connective leads masked with tape?
- make sure pattern edges parallel with wafer edges?

- expose wafers

5. Develop

- prepare large beaker with 1813 developer and water (2:1)
- wave sample gently in developer for 1 min.
- rinse with water and GENTLY Nitrogen dry
- MIX FRESH DEVELOPER after every 2-3 samples (developer becomes diluted)

6. Metallize

- deposit ~10 nm Cr or Ti and ~30nm Au with thermal or e-beam evaporator
- thickness is important- photolith thickness should be LESS THAN that of future e-beam lith for superior contact to leads

7. DO NOT LIFTOFF

- by leaving the resist and metal on sample surface, the front of the sample remains protected from HF in next step

II. Backgating

1. Oxide removal

- Put some "Siloxide Etchant" or Hydrofluoric acid (HF) into a Teflon beaker
 - DO NOT use undiluted HF for this- the fumes alone can etch around to the sample side
- place wafers exposed side up onto Teflon block
- using plastic syringe (no needle), deposit etchant onto exposed side (do not create large bubble held onto surface by surface tension- small amount will suffice)
- wait for etching (check rate)
- once done, the etchant will dewet from silicon surface, balling up on oxidized areas
- once entire surface is uniform, dip in water bath or spray LIGHTLY with deionized (DI) water into HF waste
- Nitrogen dry

2. Metallization

- Thermally evaporate 100+ nm Al onto etched side (should be done immediately following removal of oxide)

3. Liftoff of photolith

- soak in acetone for at least 30 min.
- use syringe/sonicator to remove excess metal

- Nitrogen dry
- check with optical microscope

4. Diffusion/Alloying bake

- Use tube furnace with flowing Ar to bake all samples at 350 C for at least 30 min.

III. Anchors/Fiducials

NOTE: If NOT using CVD tubes, at this point (or preferably directly after fiducials) CNT should be deposited on sample surface

1. Cleave wafer into individual playgrounds

- place wafer, pattern up, on contact paper
- using a glass slide (separated from wafer by another sheet of contact paper) as a template, make one small (~0.25") scribe at one edge
- flip sample and place on padded mat, covered by new contact paper and roll small metal rod over it (so the rod is parallel with the scribe and motion is perpendicular), pressing until sample breaks
- spray with isopropanol (IPA), Nitrogen dry

2. WITH CVD MATERIAL INTENDED FOR ELECTRICAL

MEASUREMENTS ONLY: Tube Burning

- set Keithley for 10-20V and test the connection between each adjacent lead (1-2, 2-3....7-8,8-1)
- when there is current greater than a few tens of pA, use ramping software (eg. VIcurve.vi) to ramp voltage across leads from zero to 100 V
- USE NEEDLE CONNECTORS and once connection fails (current drops to pA again), REMOVE VOLTAGE IMMEDIATELY (even if cycle isn't complete)- otherwise could arc and destroy photolith pattern
- also check connection between all leads and backgate, to ensure no leakage current- if so, repeat for those connections (may have to go up to 200 V)
- rinse with IPA and Nitrogen dry

3. Initial Imaging

- image samples (capture):
 - 1 kV, 20uA
 - upper detector (column adjust)
 - Cond. Lens 1= 1
 - 1.3kX magnification
- transfer images to NPGS-equipped computer

4. OPTIONAL: Thermal treatment (removes soap layer and SEM contamination, further diffuses Al into silicon)

THIS CAN BE DONE WHILE MAKING THE CAD DRAWINGS

- place samples in ceramic boat and push into tube furnace
- ensure Ar flow through tube and begin cooling water flow
- close both ends and allow Ar flow for ~5 min (to ensure no air)
- set temperature to 350 C
- once temperature is reached, let sit for 45 minutes
- after time, set temperature to zero and allow to cool fully (lower than 100 C when removed)
- shut off Ar, remove sample
- rinse with IPA, Nitrogen dry

5. CAD (for each)

- choose File -> Image -> Load image file and select high resolution image
- open paddle farm file, zif_fids file and zif_coarsealign file

On high resolution image:

- zoom on scale bar, hit “u”, set crosshairs at ends and input length scale
- hit “v”, draw vectors to symmetrical areas of sample (fine alignment marks), zoom on intersection, go to Point->Origin and click on intersection point, and delete vector
- copy appropriate paddle anchors and place them appropriately
- make electrical leads (make no less than 2 μ m thick), starting from anchor and going to lead
- copy zif_fids onto image and align

- copy coarse align windows onto image and align
- delete SEM background image
- delete devices and fids and NPGS-> Save what remains as *_aln.DC2
- hit Edit -> Undo
- delete alignment windows and NPGS-> Save what remains as *_dev.DC2

6. Run file (for each)

- in NPGS menu, go to Project -> Create New Project, add folder name where files were stored
- in "run file editor", set entities to 2, change first to alignment and input *-aln.DC2, input *_dev.DC2 for second

FOR ALIGNMENT:

- magnification = 800
- measured beam current = 12
- ls=2000

FOR PATTERN:

- magnification = 800
- ls=300
- measured beam current = 12
- dose= 1.2

7. FOR ELECTRICALLY CONTACTING TUBES ONLY (others simply skip this step): Bilayer PMMA

- set spin coater to 5000 rpm and 40 seconds, set hotplate with internal readout to 180 C and set a timer to 2 min
- using dropper, deposit 4% PMMA (mwt = 350k) onto sample until entire surface is covered but not dripping off edges, start spinning and (once finished) move to hotplate
- remove after 2 min

8. PMMA coating (IF step 7 was skipped)

- set spin coater to 4000 rpm and 40 seconds, set tube furnace to 180 C
- stick sample, backgate down, to spin coater chuck with two sided tape or carbon tape
- using dropper, deposit 4% PMMA (mwt = 996k) onto sample until entire surface is covered but not dripping off edges, start spinning
- bake in tube furnace for 1.5-2 hrs.
- NOTE: when contact is less important, can substitute tube furnace for 2 min. on 180 C hotplate

9. Exposure

- put sample on Faraday cup stage and set SEM for 30 kV and 5 μ A and go to faraday cup
- set focus and stigma on edge of cup
- set current in high mag mode (above 20k x) to appropriate current (check run file "measured current")
- move to playground and refocus on debris or metal edge

- set magnification (check run file “magnification”), switch control over to NPGS and process run file

- switch control back to SEM; repeat for all samples

10. Develop

- Put small amount of PMMA developer (Methyl Isobutyl Ketone(MIBK):IPA, 1:3) in 10 mL beaker and set timer for 1:10 (make sure it’s enough to submerge the sample area)
- develop each sample, rinse with DI water and Nitrogen dry
- check with optical microscope

11. Metallize

- deposit ~10 nm Cr or Ti and ~80nm Au with thermal or e-beam evaporator
- THICKNESS SHOULD BE GREATER THAN THICKNESS OF PHOTOLITH

12. Liftoff

- soak in acetone for at least 15 min.
- use syringe/sonicator to remove off excess metal
- rinse with IPA, Nitrogen dry
- check with optical microscope

IV. Paddles

1. Image samples

- image samples (capture):
 - 1 kV, 20uA

- upper detector (column adjust)
- 1.3kX magnification
- transfer images to NPGS-equipped computer
- store samples in acetone for cleanliness (rinse with IPA and Nitrogen dry before further use)

2. CAD (for each)

- choose File -> Image -> Load image file and select high resolution image
- open zif_finealign file and paddle farm file

On high resolution image:

- zoom on scale bar, hit “u”, set crosshairs at ends and input length scale
- hit “v”, draw vectors to symmetrical areas of sample (fine alignment marks), zoom on intersection, go to Point->Origin and click on intersection point, and delete vector
- copy appropriate paddles (for SWNT, generally no longer than 600nm) and place them appropriately
- ONCE ALL PADDLES ARE ALIGNED: select all paddles and move up and to the right (~45 degrees) 150-200nm to account for drift
- copy fine align windows onto image and align
- delete SEM background image
- delete devices and NPGS-> Save what remains as *_aln.DC2

- hit Edit -> Undo

- delete alignment windows and NPGS-> Save what remains as

*_dev.DC2

3. Run file (for each)

- In NPGS menu, go to Project -> Create New Project, add folder name where files were stored

- in "run file editor", set entities to 2, change first to alignment and input *-aln.DC2, input *_dev.DC2 for second

FOR ALIGNMENT:

- magnification = 900
- measured beam current = 12
- layers 11 and 15 = Start New Set
- ls(7-10)=2000
- ls(11-14)=456
- ls(15-18)=192

FOR PATTERN:

- magnification = 900
- ls=300
- measured beam current = 12
- dose= 0.9 (for very small separation distances, values as low as 0.6 can be used)

4. FOR ELECTRICALLY CONTACTING TUBES ONLY (others simply skip this step): Bilayer PMMA

- set spin coater to 5000 rpm and 40 seconds, set hotplate with internal readout to 180 C and set a timer to 2 min
- using dropper, deposit 4% PMMA (mwt = 350k) onto sample until entire surface is covered but not dripping off edges, start spinning and (once finished) move to hotplate
- remove after 2 min

5. PMMA coating (IF step 4 was skipped)

- set spin coater to 4000 rpm and 40 seconds, set tube furnace to 180 C
- stick sample, backgate down, to spin coater chuck with two sided tape or carbon tape
- using dropper, deposit 4% PMMA (mwt = 996k) onto sample until entire surface is covered but not dripping off edges, start spinning
- bake in tube furnace for 1.5-2 hrs.
- NOTE: when contact is less important, can substitute tube furnace for 2 min. on 180 C hotplate

6. Exposure (for each)

- put sample on Faraday cup stage and set SEM for 30 kV and 5 μ A and go to faraday cup
- set focus and stigma on edge of cup
- set current in high mag mode (above 20k x) to appropriate current (check run file “measured current”)
- move to playground and refocus on debris or metal edge

- set magnification (check run file “magnification”), switch control over to NPGS and process run file
- IMPORTANT: for the three steps in alignment cycle- align once to first, once to second, twice to third and IMMEDIATELY tell program to expose sample. This will prevent excess drift and consequently missing the CNT
- switch control back to SEM; repeat for all samples

7. Develop

- Put small amount of PMMA developer (MIBK:IPA, 1:3) in 10 mL beaker and set timer for 1:10 (make sure it’s enough to submerge the sample area)
- develop each sample, rinse with DI water and NITROGEN dry
- check with optical microscope

8. Metallize

- deposit ~10 nm Cr and ~80 Au with thermal evaporator

9. Liftoff

- soak in acetone for at least 15 min.
- use syringe or sonicator to remove excess metal
- rinse with IPA, Nitrogen dry
- check with optical microscope

V. Etching

NOTE: Steps 1-6 are for making etch widows for a highly localized etch- if this is not needed, skip to step 7

1. Image samples

- image samples (capture):
 - 1 kV, 20uA
 - upper detector (column adjust)
 - 1.3kX magnification
- transfer images to NPGS-equipped computer
- store samples in acetone for cleanliness (rinse with IPA and Nitrogen dry before further use)

2. CAD (for each)

- choose File -> Image -> Load image file and select high resolution image
- open zif_finealign file and paddle farm file

On high resolution image:

- zoom on scale bar, hit “u”, set crosshairs at ends and input length scale
- hit “v”, draw vectors to symmetrical areas of sample (fine alignment marks), zoom on intersection, go to Point->Origin and click on intersection point, and delete vector
- Draw line DIRECTLY over paddle (line width = 0.2)
- ONCE ALL WINDOWS ARE ALIGNED: select all paddles and move up and to the right (~45 degrees) 150-200nm to account for drift

- copy fine align windows onto image and align
- delete SEM background image
- delete devices and NPGS-> Save what remains as *_aln.DC2
- hit Edit -> Undo
- delete alignment windows and NPGS-> Save what remains as *_dev.DC2

3. Run file (for each)

- in NPGS menu, go to Project -> Create New Project, add folder name where files were stored
- in “run file editor”, set entities to 2, change first to alignment and input *-aln.DC2, input *_dev.DC2 for second

FOR ALIGNMENT:

- magnification = 900
- measured beam current = 12
- layers 11 and 15 = Start New Set
- ls(7-10)=2000
- ls(11-14)=456
- ls(15-18)=192

FOR PATTERN:

- magnification = 900
- ls=300
- measured beam current = 12
- dose= 0.9

4. PMMA coating

- set spin coater to 4000 rpm and 40 seconds, set tube furnace to 180 C
- stick sample, backgate down, to spin coater chuck with two sided tape or carbon tape
- using dropper, deposit 4% PMMA (mwt = 996k) onto sample until entire surface is covered but not dripping off edges, start spinning
- bake in tube furnace for 1.5-2 hrs.
- NOTE: may be able to substitute tube furnace for 2 min. on 180 C hotplate

5. Exposure (for each)

- put sample on Faraday cup stage and set SEM for 30 kV and 5 μ A and go to faraday cup
- set focus and stigma on edge of cup
- set current in high mag mode (above 20k x) to appropriate current (check run file “measured current”)
- move to playground and refocus on debris or metal edge
- set magnification (check run file “magnification”), switch control over to NPGS and process run file
- IMPORTANT: for the three steps in alignment cycle- align once to first, once to second, twice to third and IMMEDIATELY tell program to expose sample. This will prevent excess drift and consequently missing the CNT

- switch control back to SEM; repeat for all samples
6. Develop
- Put small amount of PMMA developer (MIBK:IPA, 1:3) in 10 mL beaker and set timer for 1:10 (make sure it's enough to submerge the sample area)
 - develop each sample, rinse with DI water and Nitrogen dry
 - check with optical microscope (may not be able to see)
7. Test etch samples (when etch rate isn't established)
- scribe several (three or four) small pieces of silicon from *the same wafer that your sample came from* (preferably with photolith on them)
 - rinse with solvents
 - place small drop of Buffered HF (BHF) (or "siloxide etchant") on each wafer and stop etch (with water bath after varying times (no need to exceed 10 min, usually))
 - use AFM to measure etch depth as metal edges (compared to original wafer)
 - calculate time for your sample etching
8. Sample etching
- pour a small amount of BHF solution into a small Teflon beaker and prepare a timer
 - use plastic syringe, place drops of BHF onto your sample (DO NOT spill over edge- will eat away backgate)

9. Etch stop

- prepare large beaker of DI water and a storage jar of ethanol
- remove working sample at desired etch depth
 - keep in mind that etch rate may be varied by the presence of materials (cnt, etc) or by contamination from previous imaging- judge accordingly
- dip sample directly into DI water (do *not* let the liquid leave the surface of the sample; keep wet)
- *IF USING ETCH WINDOWS: soak in acetone for AT LEAST 15 min. to remove PMMA
- remove and place in jar of ethanol for storage until critical point drying

10. Critical point drying

- **make sure all three valves on critical point dryer are firmly closed**
- remove lid and pour ethanol in drying chamber until port hole is high enough to cover samples (judge by eye)
- place small glass ring (flow protector) into chamber (and off to right), and inside ring put one of the curved-bottom ceramic pieces (broken tube furnace boat)
- remove sample from jar and put directly into chamber ethanol (again, do not break surface tension on sample) and place FACE

DOWN in curved piece. If all samples don't fit, ceramic pieces are stackable; close lid

- open both tanks of CO₂, push "MAINS"

- push "TEMPERATURE" and set goal temperature to 15, let chamber cool

- once cooled, open GAS IN knob (on left of machine) **slightly** and let port hole fill entirely

 - if it is filled too quickly, the turbulence may damage your samples

- close GAS IN, open GAS OUT (right side front) several turns and then slowly open METERING VALVE (right side rear) to let liquid drain (do *not* let liquid level drop to the sample)

- close both METERING VALVE and GAS OUT and repeat filling process (from "open GAS IN", above) 4 or 5 times, until liquid is completely clear and all ethanol is replaced

- make sure all valves are closed and close CO₂ tanks

- set goal temperature to 45; transition will occur as pressure and temperature rise- watch port hole for it

- after transition, open METERING VALVE several turns and open GAS OUT *very* slightly (should only have started to hear the gas coming out)

- let pressure reduce; DO NOT let condensation occur (caused by letting out gas too fast)

- once pressure is atmospheric, close all valves, unscrew lid, remove sample, replace lid and log useage

Citation List

1. Iijima, S., *Helical microtubules of graphitic carbon*. Nature, 1991. **354**: p. 56-58.
2. Lu, J.P., *Elastic Properties of Carbon Nanotubes and Nanoropes*. Phys. Rev. Lett, 1997.
3. Huntington, J.B., in *Solid State Physics*, S. F. and T. D., Editors. 1958, Academic: New York.
4. Babic, B., et al., *Intrinsic thermal vibrations of suspended doubly clamped single-wall carbon nanotubes*. Nano Letters, 2003. **3**(11): p. 1577-1580.
5. Gao, R.P., et al., *Nanomechanics of individual carbon nanotubes from pyrolytically grown arrays*. Physical Review Letters, 2000. **85**(3): p. 622-625.
6. Krishnan, A., et al., *Young's modulus of single-walled nanotubes*. Physical Review B, 1998. **58**(20): p. 14013-14019.
7. Poncharal, P., et al., *Electrostatic deflections and electromechanical resonances of carbon nanotubes*. Science, 1999. **283**(5407): p. 1513-1516.
8. Treacy, M.M.J., T.W. Ebbesen, and J.M. Gibson, *Exceptionally high Young's modulus observed for individual carbon nanotubes*. Nature, 1996. **381**(6584): p. 678-680.
9. Wong, E.W., P.E. Sheehan, and C.M. Lieber, *Nanobeam mechanics: Elasticity, strength, and toughness of nanorods and nanotubes*. Science, 1997. **277**(5334): p. 1971-1975.
10. Falvo, M.R., et al., *Bending and buckling of carbon nanotubes under large strain*. Nature, 1997. **389**(6651): p. 582-584.
11. Hall, A., et al., *Simple and efficient method for carbon nanotube attachment to scanning probes and other substrates*. Applied Physics Letters, 2003. **82**(15): p. 2506-2508.
12. Shaffer, M.S.P. and A.H. Windle, *Fabrication and characterization of carbon nanotube/poly(vinyl alcohol) composites*. Advanced Materials, 1999. **11**(11): p. 937-+.
13. Curran, S.A., et al., *A composite from poly(m-phenylenevinylene-co-2,5-dioctoxy-p-phenylenevinylene) and carbon nanotubes: A novel material for molecular optoelectronics*. Advanced Materials, 1998. **10**(14): p. 1091.

14. Williams, P.A., et al., *Torsional response and stiffening of individual multiwalled carbon nanotubes*. Physical Review Letters, 2002. **89**(25): p. 255502.
15. Williams, P.A., et al., *Fabrication of nanometer-scale mechanical devices incorporating individual multiwalled carbon nanotubes as torsional springs*. Applied Physics Letters, 2003. **82**(5): p. 805-807.
16. Dresselhaus, M.S., G. Dresselhaus, and P.C. Eklund, *Science of Fullerenes and Carbon Nanotubes*. 1996, San Diego: Academic Press.
17. Tans, S.J., A.R.M. Verschueren, and C. Dekker, *Room-temperature transistor based on a single carbon nanotube*. Nature, 1998. **393**(6680): p. 49-52.
18. Odom, T.W., et al., *Structure and electronic properties of carbon nanotubes*. Journal Of Physical Chemistry B, 2000. **104**(13): p. 2794-2809.
19. Kwon, Y.K. and D. Tomanek, *Electronic and structural properties of multiwall carbon nanotubes*. Physical Review B, 1998. **58**(24): p. R16001-R16004.
20. Sze, S.M., *Physics of Semiconductor Devices*. 2nd ed. 1981, New York: John Wiley & Sons.
21. Javey, A., et al., *Ballistic carbon nanotube field-effect transistors*. Nature, 2003. **424**(6949): p. 654-657.
22. Nosh, Y., et al., *Relation between conduction property and work function of contact metal in carbon nanotube field-effect transistors*. Nanotechnology, 2006. **17**(14): p. 3412-3415.
23. Johnston, D.E., et al., *Electronic devices based on purified carbon nanotubes grown by high-pressure decomposition of carbon monoxide*. Nature Materials, 2005. **4**(8): p. 589-592.
24. Martel, R., et al., *Single- and multi-wall carbon nanotube field-effect transistors*. Applied Physics Letters, 1998. **73**(17): p. 2447-2449.
25. Sazonova, V., et al., *A tunable carbon nanotube electromechanical oscillator*. Nature, 2004. **431**(7006): p. 284-287.
26. Streetman, B.G., *Solid State Electronic Devices*. 3rd ed. 1990, Englewood Cliffs, NJ: Prentice-Hall.
27. Griffiths, D.J., *Introduction to Electrodynamics*. 3rd ed. 1999, Upper Saddle, NJ: Prentice Hall.

28. Thess, A., et al., *Crystalline ropes of metallic carbon nanotubes*. Science, 1996. **273**(5274): p. 483-487.
29. Kong, J., A.M. Cassell, and H.J. Dai, *Chemical vapor deposition of methane for single-walled carbon nanotubes*. Chemical Physics Letters, 1998. **292**(4-6): p. 567-574.
30. O'Connell, M.J., et al., *Band gap fluorescence from individual single-walled carbon nanotubes*. Science, 2002. **297**(5581): p. 593-596.
31. Li, Y., et al., *Preparation of monodispersed Fe-Mo nanoparticles as the catalyst for CVD synthesis of carbon nanotubes*. Chemistry Of Materials, 2001. **13**(3): p. 1008-1014.
32. Hall, A.R., et al., *Experimental measurement of single-wall carbon nanotube torsional properties*. Physical Review Letters, 2006. **96**(25): p. 256102.
33. Appenzeller, J., et al., *Optimized contact configuration for the study of transport phenomena in ropes of single-wall carbon nanotubes*. Applied Physics Letters, 2001. **78**(21): p. 3313-3315.
34. Chopra, N., *PhD Thesis*. 1996, University of California at Berkeley.
35. Salvetat, J.P., et al., *Elastic and shear moduli of single-walled carbon nanotube ropes*. Physical Review Letters, 1999. **82**(5): p. 944-947.
36. Walters, D.A., et al., *Elastic strain of freely suspended single-wall carbon nanotube ropes*. Applied Physics Letters, 1999. **74**(25): p. 3803-3805.
37. Minot, E.D., *PhD Thesis*. 2004, Cornell University.
38. Williams, P.A., *PhD Thesis*. 2002, University of North Carolina at Chapel Hill.
39. DiCarlo, A., et al., *How (and why) twisting cycles make individual MWCNTs stiffer*. unpublished, 2004.
40. Papadakis, S.J., et al., *Resonant oscillators with carbon-nanotube torsion springs*. Physical Review Letters, 2004. **93**(14): p. 146101.
41. Meyer, J.C., M. Paillet, and S. Roth, *Single-molecule torsional pendulum*. Science, 2005. **309**(5740): p. 1539-1541.
42. Evoy, S., et al., *Nanofabrication and electrostatic operation of single-crystal silicon paddle oscillators*. Journal Of Applied Physics, 1999. **86**(11): p. 6072-6077.

43. Young, W.C., *Roark's Formulas for Stress and Strain*. 6th ed. 1989, New York: McGraw-Hill.
44. Yakobson, B.I., C.J. Brabec, and J. Bernholc, *Nanomechanics of carbon tubes: Instabilities beyond linear response*. Physical Review Letters, 1996. **76**(14): p. 2511-2514.
45. Ding, J.W., et al., *Curvature and strain effects on electronic properties of single-wall carbon nanotubes*. Journal Of Physics-Condensed Matter, 2003. **15**(27): p. L439-L445.
46. Kane, C.L. and E.J. Mele, *Size, shape, and low energy electronic structure of carbon nanotubes*. Physical Review Letters, 1997. **78**(10): p. 1932-1935.
47. Maiti, A., A. Svizhenko, and M.P. Anantram, *Electronic transport through carbon nanotubes: Effects of structural deformation and tube chirality*. Physical Review Letters, 2002. **88**(12): p. 126805.
48. Rochefort, A., et al., *Electrical and mechanical properties of distorted carbon nanotubes*. Physical Review B, 1999. **60**(19): p. 13824-13830.
49. Yang, L., et al., *Band-gap change of carbon nanotubes: Effect of small uniaxial and torsional strain*. Physical Review B, 1999. **60**(19): p. 13874-13878.
50. Yang, L. and J. Han, *Electronic structure of deformed carbon nanotubes*. Physical Review Letters, 2000. **85**(1): p. 154-157.
51. Mintmire, J.W. and C.T. White, *Universal density of states for carbon nanotubes*. Physical Review Letters, 1998. **81**(12): p. 2506-2509.
52. White, C.T. and J.W. Mintmire, *Density of states reflects diameter in nanotubes*. Nature, 1998. **394**(6688): p. 29-30.
53. Clauss, W., D.J. Bergeron, and A.T. Johnson, *Atomic resolution STM imaging of a twisted single-wall carbon nanotube*. Physical Review B, 1998. **58**(8): p. R4266-R4269.
54. Paulson, S., et al., *In situ resistance measurements of strained carbon nanotubes*. Applied Physics Letters, 1999. **75**(19): p. 2936-2938.
55. Tomblor, T.W., et al., *Reversible electromechanical characteristics of carbon nanotubes under local-probe manipulation*. Nature, 2000. **405**(6788): p. 769-772.
56. Minot, E.D., et al., *Tuning carbon nanotube band gaps with strain*. Physical Review Letters, 2003. **90**(15): p. 156401.

57. Cao, J., Q. Wang, and H.J. Dai, *Electromechanical properties of metallic, quasimetallic, and semiconducting carbon nanotubes under stretching*. Physical Review Letters, 2003. **90**(15): p. 157601.
58. Stampfer, C., et al., *Nano-electromechanical displacement sensing based on single-walled carbon nanotubes*. Nano Letters, 2006. **6**(7): p. 1449-1453.
59. Cohen-Karni, T., et al., *Torsional electromechanical quantum oscillations in carbon nanotubes*. Nature Nanotechnology, 2006. **1**(1): p. 36-41.
60. Yuzvinsky, T.D., et al., *Precision cutting of nanotubes with a low-energy electron beam*. Applied Physics Letters, 2005. **86**(5).
61. Sazonova, V., *PhD Thesis*. 2006, Cornell University.
62. Collins, P.G., et al., *Extreme oxygen sensitivity of electronic properties of carbon nanotubes*. Science, 2000. **287**(5459): p. 1801-1804.
63. Marion, J. and S. Thornton, *Classical Dynamics of Particles and Systems*. 4th ed. 2002: Harcourt Brace College.
64. Houston, B.H., et al., *Thermoelastic loss in microscale oscillators*. Applied Physics Letters, 2002. **80**(7): p. 1300-1302.
65. Yasumura, K.Y., et al., *Quality factors in micron- and submicron-thick cantilevers*. Journal Of Microelectromechanical Systems, 2000. **9**(1): p. 117-125.
66. Bhiladvala, R.B. and Z.J. Wang, *Effect of fluids on the Q factor and resonance frequency of oscillating micrometer and nanometer scale beams*. Physical Review E, 2004. **69**(3).
67. Mihailovich, R.E. and N.C. MacDonald, *Dissipation measurements of vacuum-operated single-crystal silicon microresonators*. Sensors And Actuators A-Physical, 1995. **50**(3): p. 199-207.
68. Mohanty, P., et al., *Intrinsic dissipation in high-frequency micromechanical resonators*. Physical Review B, 2002. **66**: p. 085416.
69. Photiadis, D.M. and J.A. Judge, *Attachment losses of high Q oscillators*. Applied Physics Letters, 2004. **85**(3): p. 482-484.
70. Cross, M.C. and R. Lifshitz, *Elastic wave transmission at an abrupt junction in a thin plate with application to heat transport and vibrations in mesoscopic systems*. Physical Review B, 2001. **6408**(8): p. art. no.-085324.

71. Ekinci, K.L. and M.L. Roukes, *Nanoelectromechanical systems*. Review Of Scientific Instruments, 2005. **76**(6).
72. Nguyen, H.D., et al., *Angular vertical comb-driven tunable capacitor with high-tuning capabilities*. Journal Of Microelectromechanical Systems, 2004. **13**(3): p. 406-413.
73. Truitt, P.A., et al., *Efficient and sensitive capacitive readout of nanomechanical resonator arrays*. Nano Letters, 2007. **7**(1): p. 120-126.
74. LaHaye, M.D., et al., *Approaching the quantum limit of a nanomechanical resonator*. Science, 2004. **304**(5667): p. 74-77.
75. Cleland, A.N. and M.L. Roukes, *Fabrication of high frequency nanometer scale mechanical resonators from bulk Si crystals*. Applied Physics Letters, 1996. **69**(18): p. 2653-2655.
76. Purcell, S.T., et al., *Tuning of nanotube mechanical resonances by electric field pulling*. Physical Review Letters, 2002. **89**(27).
77. Gomer, R., *Field Emission and Field Ionization*. 1993, New York: American Institute of Physics.
78. Piazza, G., et al., *Voltage-tunable piezoelectrically-transduced single-crystal silicon micromechanical resonators*. Sensors And Actuators A-Physical, 2004. **111**(1): p. 71-78.
79. Piekarski, B., et al., *Surface micromachined piezoelectric resonant beam filters*. Sensors And Actuators A-Physical, 2001. **91**(3): p. 313-320.
80. Bargatin, I., et al., *Sensitive detection of nanomechanical motion using piezoresistive signal downmixing*. Applied Physics Letters, 2005. **86**(13).
81. Fennimore, A.M., et al., *Rotational actuators based on carbon nanotubes*. Nature, 2003. **424**(6947): p. 408-410.
82. Jorio, A., et al., *Structural (n, m) determination of isolated single-wall carbon nanotubes by resonant Raman scattering*. Physical Review Letters, 2001. **86**(6): p. 1118-1121.
83. Qin, L.C., *Determination of the chiral indices (n,m) of carbon nanotubes by electron diffraction*. Physical Chemistry Chemical Physics, 2007. **9**(1): p. 31-48.
84. Arnold, M.S., et al., *Sorting carbon nanotubes by electronic structure using density differentiation*. Nature Nanotechnology, 2006. **1**(1): p. 60-65.